



SAPIENZA
UNIVERSITÀ DI ROMA

Sapienza Università di Roma

Dipartimento di Fisica

Scuola di dottorato in Fisica degli Acceleratori

XXIX Ciclo

**6D Phase Space Optimisation for High
Brightness Electron Beams in RF Linacs as
Drivers for High Brilliance Inverse Compton
Scattering X and γ Ray Sources**

S. S. D. FIS/01

Relatore:

Prof. Luigi Palumbo

Correlatore:

Dr.ssa Cristina Vaccarezza

Direttore della Scuola di

Dottorato:

Prof. Riccardo Faccini

Autore:

Anna Giribono

A. A. 2016-2017



SAPIENZA
UNIVERSITÀ DI ROMA

Sapienza Università di Roma

Department of Physics

PhD School on Accelerator Physics

Cycle XXIX

6D Phase Space Optimisation for High Brightness Electron Beams in RF Linacs as Drivers for High Brilliance Inverse Compton Scattering X and γ Ray Sources

Anna Giribono

Supervisors:

Prof. Luigi Palumbo

Dr. Cristina Vaccarezza

Referees:

Prof. Hugues Monard

Prof. Vittoria Petrillo

Doctoral School director:

Prof. Riccardo Faccini

Examination Board:

Prof. Antonio Capone

Prof. Danilo Giulietti

Prof. Renato Fedele

A. A. 2016-2017



Contents

Introduction	i
Motivation	i
Dissertation Overview	iii
1 Optimising RF Linacs as Drivers for Bright Inverse Compton Radiation	
Sources	1
1.1 Introduction	1
1.2 High Brightness Electron Beam Generation in RF Photoinjectors	6
Emittance Compensation Method and Invariant Envelope Theory	7
Velocity Bunching Technique	10
Simulation Tools	11
2 Inverse Compton Scattering of a Relativistic Electron Beam and a Laser	
Pulse	13
2.1 Kinematics of the Interaction	13
2.2 Beam-beam Scattering	17
2.3 Scaling Laws	20
3 ELI-NP GBS Linac	23
3.1 An advanced high brilliance γ source	23
3.2 Accelerator Design Criteria	28
3.3 The RF Linac Layout	30

The Photo-injector	31
The C-band Booster Linac	34
Diagnostic Tools	35
3.4 RF Linac Start to End Simulations	36
The Photo-Injector	36
The C-band Booster Linac	40
Wakefield Effects in Single and Multi-bunch Operation	43
Quasi-constant Gradient C-band cavities	51
3.5 Machine Sensitivity Studies	54
3.6 Dark Current Evaluation	61
3.7 Final Considerations	66
4 SPARC LAB RF linac and TS Beamline	69
4.1 The SPARC LAB Test Facility	69
4.2 TS Experimental Setup	73
Electron Beam Dynamics	75
FLAME Laser System	78
Synchronization	79
Interaction Region	81
X-ray beam diagnostics	83
4.3 Commissioning Results	83
First commissioning phase	84
Second commissioning phase	89
4.4 Final Considerations	95
5 Conclusions	97
Appendix A Transverse Wakefield Effects	99
A.1 Effect of Injection Offset	99
A.2 Effect of Cavity Misalignments	101
Appendix B Transverse Beam Dynamics in RF Accelerating Structures	103
Bibliography	107
List of Figures	121

<i>CONTENTS</i>	3
List of Tables	129
Ringraziamenti	131



Introduction

Motivation

X and γ ray Inverse Compton sources are among the most performing devices in producing radiation with short wavelength, high power, ultrashort time duration, large transverse coherence and tunability. The expertise coming from the R&D activity on high brightness linear accelerators and high quality high power ps laser system enables today a transition phase towards the era of effective user facilities in X-ray imaging and γ -ray Nuclear Physics and Photonics. Those sources require strong constrains for the electron beam: the minimization of both the transverse normalized emittance and the energy spread allows to maximize the spectral density and to guarantee the monochromaticity of the emitted radiation.

In this Ph.D. thesis a detailed study is presented on the 6D phase space optimisation for high brightness electron beams in RF linacs as drivers for advanced and high brilliance Inverse Compton sources. In particular this work focuses on the beam dynamics studies for the ELI-NP Gamma Beam System (GBS) RF linac, currently in its delivering phase in Magurele (Romania), and on the commissioning phase of the SPARC.LAB Thomson Source electron beamline at INFN-LNF in Frascati.

In March 2014 the EuroGammas Consortium, which is led by Italy's Institute of Nuclear Physics (INFN), awarded and signed the contract to build and deliver the ELI-NP Gamma Beam System (GBS) in Romania, therefore the executive phase of the RF linac project started since then. Nearly at the same time the commissioning phase of the X-Ray Thomson source started at SPARC.LAB LNF facility.

The common aspects of the design of these two linac-based Compton sources have played an important role in the understanding of electron beam optimisation processes: beam dynamics studies together with the experience acquired in the commissioning phase ongoing at the SPARC_LAB Thomson source led the guide-lines for the 6D phase space optimisation for electron beams in the ELI-NP GBS RF linac.

The ELI-NP Gamma Beam System is an advanced gamma ray source with unprecedented specifications of brilliance ($>10^{21}$), monochromaticity (0.5%) and energy tunability (0.2 - 19.5 MeV). Here the challenging source performances are provided by the head on collision of a recirculated high power laser pulse and a train of 32 high brightness high quality electron beams with tunable energy (75 - 740 MeV) at 100 Hz repetition rate for the RF power system. My Ph.D. work has been focused on the beam physics studies and optimisation of the electron beam dynamics in the ELI-NP RF linac. Starting from the TDR of the machine, I focused on the aspects that are mostly involved in the robustness, operational reliability and active and passive element constraint specifications of such a demanding machine and on the challenge introduced by the multi-bunch operation. More in details I performed the start to end simulations for the RF linac to optimise the 6D phase space of the electron beam at the interaction point for a wide set of working points, each one as required by the user community. Beam dynamics studies have been also performed for the C-band linac to evaluate the effect on the beam quality of the short and long-range wakefields, both in the single and multi-bunch operation. The transverse motion in the C-band linac has been investigated considering the quasi-constant accelerating field profile of the cavities and has been shown that a new linac matching can help to preserve the electron beam quality. Machine sensitivity studies are also described aiming to check the robustness of the source in terms of jitter and misalignments in the linac. Finally the evaluation of the dark current is addressed to drive the design specifications for the shielding and the radiation safety system of the linac tunnel.

In the meantime at the SPARC_LAB X-ray Thomson Source (TS) the playground opportunity has been taken to couple the SPARC high brightness photoinjector with the high power FLAME laser system in order to provide a quasi coherent, moderate monochromatic (10%) X-ray source with the photon energy tunable in the range of 20 to 250 keV. Here a head on collision is foreseen at the Interaction Point between a 30 to 150 MeV electron beam and the 250 TW FLAME laser pulse which provides ~ 2 J on target. For the first experiment a high brightness 30 MeV electron beam was meant to be delivered at the interaction point for the generation of a X-ray beam for

the X-ray imaging of mammographic phantoms with the phase contrast technique. In this framework the dissertation aims to show both the beam dynamics simulations in the TS beamline and the strategies adopted in the commissioning phase to optimise the 50 and 30 MeV electron beam at the interaction point in the first and second experimental campaign.

Dissertation Overview

In this Ph.D. thesis are presented the studies on the 6D phase space optimisation for high brightness electron beams in RF linacs as drivers for advanced high brilliance Inverse Compton sources. Here the aim is to show how the expertise coming from the R&D activity on high brightness linear accelerators, coupled with high quality high power ps laser system, impacts on the X and γ radiation source performances and permits to achieve short wavelength, high power, ultrashort time duration, large transverse coherence and tunability. In particular the work in this thesis focus on beam dynamics studies in the ELI-NP GBS RF linac and on the commissioning phase of the SPARC.LAB Thomson Source, where high brightness electron beams (as those required by these sources) are currently handled by the SPARC.LAB photo-injector.

In Chapter 1 the review of Inverse Compton Scattering X and γ -ray sources is reported. The interest in the Compton radiation sources comes from the possibility to produce high energy photons as result of the scattering between a relativistic electron beam and a low energy photon beam: in this case the emitted photon energy depends quadratically on the electron beam energy and is strongly correlated with the emission angle, allowing narrow bandwidth by means of collimation systems. The recent technological development in the field of high brightness linear accelerators and high energy/high quality lasers enables today designing high brilliance Compton-X and Gamma-photon sources that are considered to be the new roadmap to open the era of effective user facilities in X-ray imaging and γ -ray Nuclear Physics and Photonics. In Chapter 1 are also reported few considerations on the handling of high brightness electron beam in RF linac; then it follows theoretical studies on two of most common techniques that permits the generation of high brightness electron beams in RF photoinjectors: the emittance compensation method, together with the invariant envelope theory, and the velocity bunching technique. Finally the simulation tools adopted for the beam dynamics studies, each optimised for the specific regime explored by the electron beam along the RF linac (i.e. the space-charge dominated regime and the emittance-dominated regime)

are here described.

In Chapter 2 the theory of Inverse Compton Scattering of relativistic electron beams and low energy photons is described starting from the kinematics of the electron-photon collision in the Compton model assumption; then the beam-beam interaction is treated in detail, showing also very useful *scaling laws* to evaluate analytically the characteristics of the photon beam produced by the Compton backscattering of the two colliding beams. The features of the emitted photon beam are illustrated, in particular with regards to the electron beam parameters showing that is possible to tune the energy and the bandwidth of the source acting on the electron beam 6D phase space orientation.

Chapter 3 starts with a general description of the ELI-NP GBS project and of the design criteria that lead to the final RF linac layout. Then are reported the beam dynamics studies that have been addressed during the executive phase of the project: start to end simulations of the linac are shown for several working points, each required as by the user community; studies on wakefield effects in both single and multi-bunch operation, in particular with regards to the longitudinal beam dynamics in the multi-bunch operation including long-range longitudinal wakefields; investigation of the transverse motion in quasi-constant accelerating field profile in the C-band RF linac. Machine sensitivity studies are also described in order to provide the basis for the alignment procedure and jitter tolerances. Finally the dark current transport has been simulated from the photo-cathode up to the dumps to evaluate in more detail beam losses in the dumpers and to provide the basis for shielding and safety system specifications.

In Chapter 4 the SPARC_LAB Thomson source is presented and the commissioning strategies and results are detailed illustrated. Firstly the SPARC_LAB project is described together with the research activity results here achieved and the current status of the machine. Then are reported the numerical simulations of the electron beam dynamics in the SPARC_LAB Thomson Source beamline needed to optimise the beam 6D phase space at the IP in view of the source commissioning phase. Simulated and experimental results are reported together with the upgrade of the electron beam transfer line and interaction region that can permit to achieve better source performances.

At last we draw the final conclusions.

Optimising RF Linacs as Drivers for Bright Inverse Compton Radiation Sources

Contents

1.1	Introduction	1
1.2	High Brightness Electron Beam Generation in RF Photoinjectors	6
	Emittance Compensation Method and Invariant Envelope Theory	7
	Velocity Bunching Technique	10
	Simulation Tools	11

1.1 Introduction

The interest in the Compton radiation sources started nearly 100 years ago with the A.H Compton Nobel-Prize winning work, where the arise of an up-shifted frequency photon as result of the Compton scattering of an electron and a laser beam was shown [1]. Nevertheless the idea of producing high energy photons in accelerators through Compton Scattering was proposed by H. Motz[2] and K. Landecker [3] in 1951-52 and it was developed by R. Milburn [4] in 1963 and independently by F. Arutyunian and V. Tumanian [5] later on. Indeed the scattering between a relativistic electron beam and a low energy photon beam results in a radiation source whose energy depends quadratically on the electron beam energy and is strongly correlated with the emission angle, allowing narrow bandwidth by means of collimation systems (see 2). Even if such Compton sources were considered very effective “*photon accelerators*”, the laser and

accelerator techniques at those times did not allow to consider Arutyunian and V. Tumanian's proposal from a practical point of view; the reason lied in the low cross section value of this sources (the maximum value is given by the Thomson cross section $\sigma_{tot}^{TH} = 0.67$ barn) coupled with the unavailable high power laser needed for high performances in terms of particle-photon collider luminosity, the figure of merit that measures the ability of a particle collider to produce the required number of interactions [6].

In 1978 the LADON test facility at INFN-LNF in Frascati, the very first Compton radiation source, worked in the head-on configuration for hadronic physics experiments and produced polarised and tagged gamma-ray beams with energies up to 80 MeV with a beam intensity of $\sim 10^4 - 10^5$ photons/s [7, 8]. Successful experiments at LADON were followed by the construction of other facilities, as the Graal at European Synchrotron Radiation Facility (ESRF) at Grenoble [9], and in this first phase several Compton scattering experiments took place in existing electron storage rings that offered GeV-scale electron energies needed to produce very hard γ -ray photons.

After a decade of R&D activity and machine test and development, the X/ γ -ray Compton sources are in the ongoing transition phase towards the era of effective user facilities in X-ray imaging and γ -ray Nuclear Physics and Photonics. The development of X and γ -ray sources with large spectral flux and high tunability opens the way to applications at the frontier of science [10, 11], allowing us to deepen the fundamental knowledge and understanding of the properties of materials and living systems by probing the matter on microscopic-to-nuclear scales in space and time [11]. Thomson [12, 13, 14, 15, 16, 17, 18, 19] and Compton sources [20, 21] are among the most performing devices in producing radiation with short wavelength, high power, ultrashort time duration, large transverse coherence and tunability. In the existing Compton devices, with emitted photon energies below $E_p = 100$ keV, the emission is generally provided by the collision between a high energy laser and a high brightness electron beam generated by linacs or storage rings [15], while more sophisticated schemes and interaction mechanisms are rapidly becoming a reality [22, 23, 24, 25, 26]. The most usual configuration is the head-on scattering, so called *Inverse Compton Scattering (ICS) source*, with the collision angle between the interaction beams $\theta_i = \pi$, but also geometries with different angles have been tested [16]. The mean photon energy actually measured in the various sources ranges between 7 and 70 keV, each device presenting a wide tunability. Experiments on the source characterization [27, 28, 29, 30], on the transmission, dark field and phase contrast imaging, computed microtomography, K-edge techniques on phantom [31], biological [15, 32], animal [33, 34] and human [16] samples have been

then successfully performed.

Advanced Inverse Compton γ -ray sources based on the scattering between high brightness electron bunches and high intensity high quality laser pulses are considered to be the new road-map to open the field of nuclear photonics; high brightness electron beam allows to improve both flux and brightness of the source, while increasing power of the laser available systems from TW to PW leads to an improvement in terms of number of emitted photons of three orders of magnitude with given pulse duration and the beam size. Within the next few years, laser performances are expected to increase by about an order of magnitude, and up to three orders of magnitude may be gained at the planned Extreme Light Infrastructure (ELI) facility (detailed described in 3.1) and High Power laser Energy Research (HiPER) facility [35]. Several laboratories world-wide are pursuing projects to develop such advanced Compton sources (Mega-ray project, AIST), with the main aim to step up from the present state of the art parameters, represented by the user facility for nuclear physics research HIGS, where the electron beam collides with an intracavity FEL beam resulting in total gamma-ray intensities (energy between 2 and 100 MeV with linear and circular polarizations) higher than 10^9 photons/second with few percent energy resolution.

The unique combination of high brightness electron beam and high quality-high intensity laser system, also enabled possibilities of producing hard electromagnetic radiation in a device that is relatively small bringing the quality and tunability of a synchrotron beamline to an X-ray scientist's local laboratory and so compatible with locations inside University Campus, large Hospitals, Museums or mid-size research infrastructures. New compact sources are rapidly being built all over the world, as the linac-based Southern Europe Thomson source for Applied Research (STAR), a 12 m long overall research infrastructure for a regional facility, or the storage-ring based ThomX which fits in $10 \times 10 \text{ m}^2$ [36]. The existence of such new compact high-flux X-ray machines based on Compton scattering has stimulated the commercial activity: the Lyncean Compact Light source is in operation right now and provides a continuously tunable energy spectrum and high spatial coherence - combined with some unique attributes such as intrinsically narrow bandwidth (few %) and a moderate (few mrad) diverging cone beam [37]. The Munich Compact Light Source (MuCLS) [38], installed at the Technische Universität in Munich (Germany), is the first commercially sold compact Compton source ($10 \times 10 \text{ m}^2$) developed and manufactured by Lyncean Technologies Inc. and is in operation since early 2015.

Figure 1.1 lists the existing and planned compact Compton sources updated at 2010

	Type	Energy [KeV]	Flux (@ 10% bandwidth)	Source size (μm)
*PLEIADES (LLNL) [11,12]	Linac	10-100	10^7 (10 Hz)	18
*Vanderbilt [13,14]	Linac	15-50	10^8 (few Hz)	30
*SLAC [15]	Linac	20-85		
*Waseda University [16,17]	Linac	0.25-0.5	$2.5 \cdot 10^4$ (5 Hz)	
*AIST, Japan [18]	Linac	10-40	10^6	30
*Tsinghua University [19]	Linac	4.6	$1.7 \cdot 10^4$	
*LUCX (KEK) [20]	Linac	33	$5 \cdot 10^4$ (12.5 Hz)	80
+ UTNL, Japan [21,22]	Linac	10-40	10^9	
MIT project [23]	Linac	3-30	$3 \cdot 10^{12}$ (100 MHz)	2
MXI systems [24]	Linac	8-100	10^9 (10Hz)	
SPARC –PLASMONX [25]	Linac	20-380	$2 \cdot 10^8$ - $2 \cdot 10^{10}$	0.5-13
Quantum Beam (KEK) [26,27]	Linac		10^{13}	3
*TERAS (AIST) [28]	Storage ring	1-40	$5 \cdot 10^4$	2
*Lyncean Tech [29,30,31]	Storage ring	7-35	$\sim 10^{12}$	30
Kharkov (SNC KIPT) [32]	Storage ring	10-500	$2.6 \cdot 10^{13}$ (25 MHz)	35
TTX (THU China) [33,34]	Storage ring	20-80	$2 \cdot 10^{12}$	35
ThomX France [35]	Storage ring	50	10^{13} (25 MHz)	70

Table 3: Compact Compton X ray sources. Symbols * and + refers respectively to machines in operation and to machines in construction.

Figure 1.1: List of the existing and planned Compact compton sources updated at 2010 [39].

[39].

Many X and γ Inverse Compton radiation sources are based upon the novel RF linac technology: the expertise coming from high brightness linear accelerators and high quality high power ps laser system enables the production of high spectral density, monochromatic and tunable energy photon sources. At this purpose it is interesting to notice that both flux and brightness of the source can benefit from a linac-based configuration where the emittance dilution, that arises in storage-ring due to the recirculation for millions of turns, can be avoided, while the possibility of a multi-bunch operation at high repetition rate (\sim kHz) can allow to achieve flux comparable to that projected for storage ring based Compton sources. These considerations, together with the wide electron energy range covered by a linac-based Compton source, and so the fast tuning of the emitted photon beam frequency, make them very attractive to the user community. The Extreme Light Infrastructure - Nuclear Physics Gamma Beam System (ELI-NP GBS) γ -source and the X-ray Thomson Source at Sources for Plasma Accelerators and Radiation Compton with Lasers and Beams (SPARC.LAB) are only two of the RF linac based Inverse Compton sources for users around the world.

These two sources are very similar since both foresee the head on collision between

an intense high power laser beam and a high brightness high quality relativistic electron beam; nevertheless the available electron energy and the required source bandwidth lead the SPARC.LAB Thomson source and the ELI-NP GBS γ -source to explore different regimes (see 2.3), well described by the *classical Thomson model* and by the *quantum Compton model* respectively. The ELI-NP GBS is a ~ 90 m long advanced high spectral density gamma ray source based on the Inverse Compton Scattering phenomenon with unprecedented specifications of brilliance ($>10^{21}$), monochromaticity (0.5%) and tunable energy (0.2 - 19.5 MeV), presently under construction in Magurele, Bucharest (RO); differently the SPARC.LAB Thomson Source, is a compact quasi monochromatic ($\sim 10\%$) X ray source with a tunable energy (20 - 250 keV) and high flux (10^9 ph. per pulse in *bw*) based on the Thomson backscattering process presently under its second commissioning phase at INFN-LNF in Frascati, Rome (Italy).

As mentioned the most innovative high brightness RF linacs, that allow to control both the electron beam transverse normalized emittance and energy spread, permits to achieve the challenging requirements of Inverse Compton Sources in terms of emitted radiation features in the desired source energy range.

In the last two decades the crucial role played by the high brightness electron beams in the frontier fields of radiation generation and advanced acceleration schemes has been largely established. The production of high quality phase space electron beams has shown to be essential for the coherent X-rays generation in the FELs as well to provide the matching conditions for the novel acceleration schemes based on high gradient wakefields and for the realization of bright Gamma-ray Compton sources. The characteristic brightness parameter B can be expressed as:

$$B = \frac{2I}{\varepsilon_n^2} \quad (1.1)$$

where I is the beam current in [A] and ε_n is the normalized emittance in the transverse phase space, hence high brightness means high current and a small footprint in the transverse phase space. The expertise coming from high brightness electron linacs driving X-ray FEL's can guide the design of RF Linacs to fulfil the requirements of high spectral density Inverse Compton Sources, even if here the quest is for maximum phase space density (instead of peak brightness). Noticeably, these rms beam quality factors have to be evaluated on projected (integrated) values over the electron bunch, unlike in FEL's machines where the so called "slice" values are mostly relevant for the high gain FEL process.

Finally a big effort has been devoted in these years to develop fruitful techniques of

phase space control and manipulation of intense electron sources based on RF guns, equipped with laser driven photocathodes, followed by one or two accelerating sections (photoinjectors).

1.2 High Brightness Electron Beam Generation in RF Photoinjectors

High quality electron beams can be achieved in RF photoinjectors by means of RF guns, equipped with laser driven photocathodes, followed by one or two accelerating sections. A simple emittance compensation scheme [40] based on a focusing solenoid at the exit of the RF gun, can be used in photoinjectors to control emittance growth due to the space charge effects while, from the invariant envelope theory [41], a proper matching of the transverse space of the electron beam injected in the downstream accelerating sections (booster) after the gun exit, can help to control the transverse emittance oscillations during the acceleration. Under the conditions of invariant envelope and proper phasing of space charge oscillations [42] the final emittance is almost compensated down to the thermal emittance value given by cathode emission with an expected emittance scaling like $\epsilon_n \propto \sigma_{cath} \propto \sqrt{Q}$, where σ_{cath} is the hitting laser spot size on the photocathode, and Q the extracted electron charge. A compression stage can occur to shorten the beam length so to achieve the required high peak current; the so-called velocity bunching method[43], has opened up a new possibility of compressing the beam inside an RF structure and if integrated in the emittance compensation process [44] can provide the desired bunch current values with the advantage of compactness of the machine and absence of Coherent Synchrotron Radiation (CSR) effects present in a magnetic compressor [45]. It is interesting to notice that a shortened beam length also permits to reduce the energy spread dilution due to RF curvature degradation, in fact the energy spread depends on the bunch length and the accelerating frequency as

$$\frac{\Delta\gamma}{\gamma} \approx 2 \left(\frac{\pi f_{RF} \sigma_z}{c} \right)^2. \quad (1.2)$$

The RF linac hybrid scheme foreseen at ELI-NP GBS γ source is based on these considerations.

The emittance compensation method, together with the invariant envelope theory, and the velocity bunching technique are described in detail in following sections.

Emittance Compensation Method and Invariant Envelope Theory

The electrons emitted from the cathode propagating through the gun region are subject to the space charge forces that lead to the emittance degradation. Even if this effect can be mitigated by means of high gradient accelerating field provided by RF gun, the phase dependent focusing forces that the electrons experience in this high gradient field still induce emittance growth[46]. Since the RF induced emittance grows with the beam dimensions (both longitudinal and transverse), a solution can be to keep them small and so leading to increased space charge forces once again. As mentioned above a focusing solenoid placed downstream the RF gun region, referred to as *emittance compensation solenoid* [40], can help reduce the space-charge induced emittance growth [46]. The solenoid applies a focusing kick to the beam that counteracts the defocusing effect due to the space charge that is strongest in the bunch middle and decreases towards the edge. Assuming the beam as divided in more slices; if any focusing kick is applied the space charge forces lead it to a fan-like distribution in the phase space; on the contrary if the solenoid kick is applied the beam propagates in the downstream drift space until the fan-like structure tends to close and a minimum phase space area is reached. If this minimum is reached in a regime where space charge effects are no more dominant, is possible to avoid the additional contribution to the emittance growth. At this purpose is useful to define the *laminarity parameter* ρ that is the ratio between the space charge force term and the emittance pressure term in the transverse plane

$$\rho = \frac{I\sigma_t^2}{2\gamma I_A \epsilon_t h^2} \quad (1.3)$$

where $I_A = 17$ kA is the Alven current [47] and $\gamma = 1 + T/mc^2$ is the normalized beam kinetic energy or “relativistic Lorentz factor”. This parameter permits to distinguish between the space-charge dominated regime, when $\rho \gg 1$, and the emittance dominated regime, when $\rho \ll 1$. It is clear that, given the other beam parameters, ρ decreases while γ increases; thus to avoid space charge induced emittance growth, the beam has to be properly matched to the downstream accelerating sections in order to keep under control the emittance oscillations and obtain the required emittance minimum at higher energy, i.e. at the injector exit.

A full theoretical description of the emittance compensation process [41] demonstrates that in the space charge-dominated regime, i.e. when the space charge collective force is largely dominant over the emittance pressure, mismatches between the space charge correlated forces and the external focusing gradient produce slice envelope os-

cillations that cause normalized emittance oscillations. It has been also shown in [48] that to damp these emittance oscillations secularly, the beam has to be propagated in the to the so-called “invariant envelope” regime, given by

$$\sigma_{INV} = \frac{1}{\gamma} \sqrt{\frac{2I}{I_A(1+4\Omega^2)\gamma}} \quad (1.4)$$

where E_{acc} is the accelerating field, $\gamma \sim 2E_{acc}$, I is the beam peak current in the bunch and Ω is the normalized focusing gradient defined as

$$\Omega^2 = \left(\frac{eB_{sol}}{mc\gamma'} \right) + \begin{cases} \sim \frac{1}{8} & \text{Standing Wave} \\ \sim 0 & \text{Traveling Wave} \end{cases}$$

The σ_{INV} is an exact solution of the rms beam envelope equation for a laminar beam, with

$$\sigma'' + \sigma' \frac{\gamma'}{\gamma} + \gamma \frac{\Omega^2 \gamma'^2}{\gamma^2} - \frac{I}{2I_A \sigma \gamma^3} = \frac{\epsilon_t h^2}{\sigma^3 \gamma^2} \sim 0 \quad (1.5)$$

According to this theory, i.e injecting the beam at a laminar waist, the working point was set for the LCLS FEL project [48]. By increasing the solenoid magnetic field, the emittance shows a double minimum behaviour along the horizontal axis as in Figure 1.2. If the accelerating structure is placed where the emittance exhibits its maximum then the emittance oscillation can be frozen and its minimum is translated at the exit of the accelerating section.

This solution corresponds to a generalized Brillouin flow condition that assures the control of emittance oscillations associated with the envelope oscillations such that the final emittance at the photoinjector exit is reduced to an absolute minimum. In order to fulfil this condition, it is necessary to match two types of flow along the photoinjector: the invariant envelope inside accelerating sections and Brillouin flow given by

$$\sigma_{BRI} = \frac{mc}{eB_{sol}} \sqrt{\frac{I}{2I_A \gamma}} \quad (1.6)$$

in intermediate drift spaces.

By substituting the (1.6) in laminarity parameter definition (1.3) one can see that the laminar regime extends up to an energy given by

$$\gamma_r = \sqrt{\frac{2}{3}} \frac{I}{I_A \epsilon_{th} \gamma'} \quad (1.7)$$

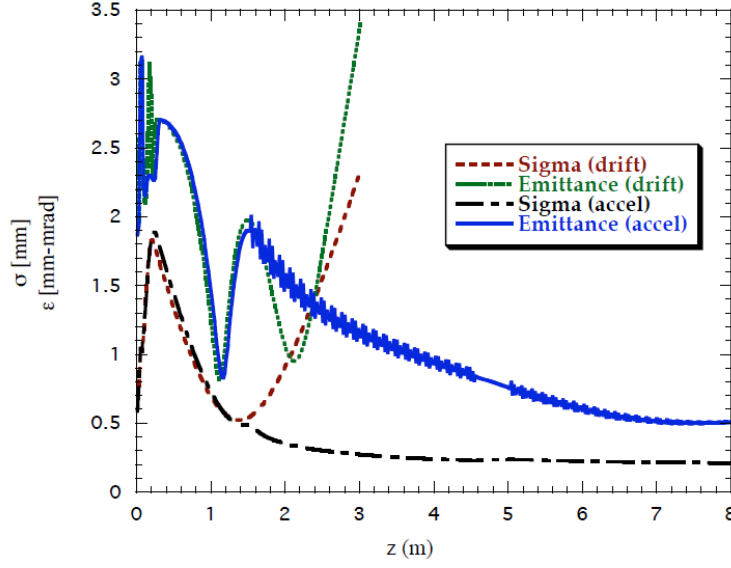


Figure 1.2: Emittance double minimum behavior, envelope evolution and emittance behaviour when accelerating structures are properly matched [48].

As a consequence of such a theory, the definition of the “injector” has to be extended up to an energy high enough to exit the laminar regime, termed *transition energy*. The beam enters then in the so called emittance-dominated regime, where trajectories cross over dominates over space charge oscillations and the total normalized emittance remains constant in an ideal accelerator.

Finally it is worth mentioning that, even if the emittance growth can be partially compensated, the beam emittance cannot be lower than its theoretical limit represented by the so called “thermal emittance”, that is an *intrinsic* feature of the beam; indeed the electrons extracted from the metal cathode belong to the tail of the Fermi-Dirac distribution and have the Maxwell velocity distribution given by

$$f(v_x, v_y, v_z) = f_0 \exp\left(-\frac{m(v_x^2 + v_y^2 + v_z^2)}{2k_B T}\right) \quad (1.8)$$

where k_B is Boltzmann constant and T the cathode temperature. The result is that the particles emerging from the cathode have an intrinsic velocity spread and so an intrinsic emittance. The thermal emittance of a non relativistic beam emerging from the cathode at the waist is

$$\epsilon_n^{th} = \frac{r_s}{2} \sqrt{\frac{k_B T}{mc^2}} \quad (1.9)$$

where r_s is the radius of the emitting surface with the hypothesis of uniform current density.

Velocity Bunching Technique

The velocity bunch technique is a compression process that consists in a rotation of the longitudinal electron phase space based on a time-velocity correlation (chirp) for which the electrons in the bunch tail are faster than those in the bunch head. This happens in the longitudinal potential of a travelling wave accelerating structure that accelerates the beam and at the same time applies an off crest energy chirp when the injected beam is slightly slower than the phase velocity of the rf wave, in such a way that when injected at the zero crossing field phase it slips back to accelerating phases. The electron beam is then compressed and accelerated at the same time in the first accelerating section after the rf gun and, under the above described conditions of invariant envelope and proper phasing of space charge oscillations, it is possible to keep control of the emittance growth.

In order to preserve the beam transverse emittance we have to integrate the longitudinal dynamics of the RF compressor into the process of emittance compensation by extending the invariant envelope theory [41] to the case of currents growing together with energy along the RF compressor. Let us assume that the current grows in the compressor at the same rate as the energy, i.e. $\frac{I_0\gamma}{\gamma_0}$ where I_0 and γ_0 are the initial values for the current and the energy, respectively, at the compressor injection. As stated in [48] this assumption is derived by observations performed in several simulations of the RF compressor, indicating that best results in terms of final beam brightness are achieved under this condition, which indeed gives rise to a new beam equilibrium. It should be noted that this condition may be violated strongly near the end of the compression process, but as this occurs at high energy, the violation may not have serious consequences. The rms envelope equation becomes in this case

$$\sigma'' + \sigma' \frac{\gamma'}{\gamma} + \sigma \frac{\Omega^2 \gamma'^2}{\gamma^2} = 0 \quad (1.10)$$

whose new exact analytical solution is

$$\sigma_{RFC} = \frac{1}{\Omega \gamma'} \sqrt{\frac{I_0}{2I_A \gamma_0}} \quad (1.11)$$

i.e. a beam flow at constant envelope (instead of $1/\sqrt{\gamma}$ as for the invariant envelope). This is dictated by a new equilibrium between the space charge defocusing term (decreasing now as $1/\gamma^2$) and the focusing and acceleration terms (imparting restoring forces to the beam): while for the invariant envelope equilibrium is achieved even in absence of external focusing (at $\Omega = 0$), in this case we need to provide external focusing.

In reference [49] the first experimental results obtained at SPARC are reported of velocity bunching compression with applied optimised compensation resulting in a significant mitigation of the emittance growth due to the compression process.

Simulation Tools

Different simulation codes have been adopted for the beam dynamics studies here presented, each optimised for the specific regime explored by the electron beam along the RF linac, i.e. the space-charge dominated regime and the emittance-dominated regime. In particular the beam dynamics in the injector has been simulated with the multi-particles codes Tstep [50] and Astra [51]. The ELI-NP GBS C-band linac has been simulated with the Elegant code [52], assuming the beam in the emittance dominated regime; the Trace 3D code [53] has been instead used to simulate the beam dynamics in the SPARC.LAB Thomson Source beamline, where the maximum beam energy chosen for the commissioning phase is below the transition energy (200 pC charge and maximum energy of 50 MeV). Additionally the code MAD [54] (version 8.51) has been employed to speed up the process of the transfer line matching.

The simulation codes with a short description of their capabilities are listed below:

- **Tstep** is an upgraded version of PARMELA [55]. It is a wide spread reliable multi-particle code that transforms the beam, represented by a collection of particles, through a user-specified linac and/or transport system, where field maps of magnets and accelerator cavities are derived from codes as POISSON, SUPERFISH and HFSS. It consists in calculating the self-fields by solving the Poisson equation for the electrostatic field in the reference frame where the beam may be considered at rest and then transforming the fields back to the laboratory frame where kicks to the particles are applied. It includes a 2-D and 3-D space-charge and thermal emittance calculation.
- **Astra** tracks particles through user defined external fields taking into account the space charge field of the particle cloud. The tracking is based on a non-adaptive

Runge-Kutta integration of 4th order. The beam line elements are set up w.r.t. a global coordinate system in Astra. All calculations in Astra are done with double precision, while output and input may be in single precision. It includes a 2-D and 3-D space-charge and thermal emittance calculation.

- **Elegant** is a beam dynamics code that computes Twiss parameters, transport matrices, non linear transport to 3rd order, closed orbits, beam transport floor coordinates, error amplification factors, dynamic apertures, and more. It performs 6-D tracking with matrices and/or canonical integrators, and supports a variety of time-dependent elements. It computes coherent and incoherent synchrotron radiation effects using a 1D model, and also performs optimisation algorithms (e.g., matching), including optimization of tracking results. It includes also wake fields and RF transverse field in the RF accelerating sections.
- **MAD** is a tool for charged-particles optics in alternating gradient accelerators and beam lines. Includes linear lattice parameter calculation, linear lattice matching, transfer matrix matching, and particle tracking.
- **TRACE 3D** is an interactive beam-dynamics program that calculates the envelopes of a bunched beam, including linear space-charge forces, through a user-defined transport system. TRACE 3-D provides an immediate graphics display of the beam envelopes and phase-space ellipses, and accommodates fourteen different types of fitting or beam-matching options.

Inverse Compton Scattering of a Relativistic Electron Beam and a Laser Pulse

Contents

2.1 Kinematics of the Interaction	13
2.2 Beam-beam Scattering	17
2.3 Scaling Laws	20

2.1 Kinematics of the Interaction

Let us consider the scattering of a relativistic electron and a photon in the laboratory frame coordinate system (x_e, y_e, z_e) . Without loss of generality we can assume the incident electron momentum \underline{p}_i along the \underline{z}_e direction and the incoming photon momentum $\hbar\underline{k}_i$ (\hbar is the Planck constant) along the direction given by the polar angle θ_i and the azimuthal angle ϕ_i , as illustrated in Figure 2.1. The collision occurs at the origin of the coordinate system. After the collision, the photon with a momentum $\hbar\underline{k}_f$ is scattered into the direction given by the polar angle θ_f and the azimuthal angle ϕ_f , see Figure 2.1. The momentum and energy conservation laws in case of an elastic scattering (as it is in our case) lead to

$$p_i + k_i = p_f + k_f \tag{2.1}$$

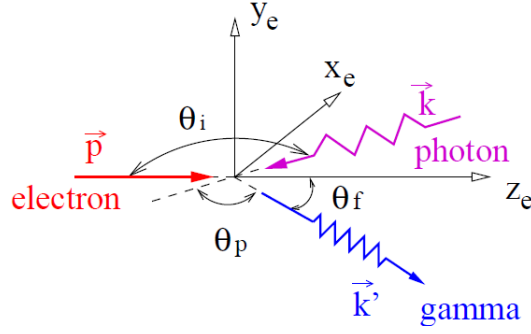


Figure 2.1: Geometry of Compton scattering of an electron and a photon in a laboratory frame coordinate system (x_e, y_e, z_e) in which the electron is incident along the z_e direction. The incident photon is propagating along the direction given by the polar angle θ_i and azimuthal angle ϕ_i . The collision occurs at the origin of the coordinate system. After the scattering, the scattered photon propagates in the direction given by the polar angle θ_f and azimuthal angle ϕ_f . θ_f is the angle between the momenta of incident and scattered photons, \underline{k}_i and \underline{k}_f . The electron after scattering is not shown in the figure.

where $p_i = (E_e/c, \underline{p}_i)$ and $k_i = (E_L/c, \hbar \underline{k}_i)$ are the 4-momenta of the electron and photon before the scattering respectively, $p_f = (E_f/c, \underline{p}_f)$ and $k_f = (E_p/c, \hbar \underline{k}_f)$ are their 4-momenta after the scattering, E_e and E_L are the energies of the electron and photon before the scattering, E_f and E_p are their energies after the scattering and c is the speed of the light. From (2.1) it follows that the electron after the interaction presents a diminished Lorentz factor given by:

$$\gamma_f = \gamma_i - \frac{h}{mc^2} (\nu_p - \nu_L) \quad (2.2)$$

where ν_p is the emitted photon frequency and can be obtained by squaring both sides of (2.1) and after some manipulations

$$\nu_p = \nu_L \frac{1 - \underline{e}_k \cdot \underline{\beta}_i}{1 - \underline{n} \cdot \underline{\beta}_i + \frac{h\nu_0}{\gamma_i mc^2} (1 - \underline{e}_k \cdot \underline{n})} \quad (2.3)$$

where $\underline{p}_j = \gamma_j \underline{\beta}_j mc$ ($j = i, f$), $\underline{k}_i = \frac{2\pi\nu_L}{c} \underline{e}_k$ and $\underline{k}_f = \frac{2\pi\nu_p}{c} \underline{n}$; the angle-energy correlation of the emitted photon is well described if the (2.4) is expressed in terms of angles and energies

$$E_p = E_L \frac{1 - \beta_i \cos \theta_i}{(1 - \beta_i \cos \theta_f) + (1 - \cos \theta_p) \frac{E_L}{E_e}} \quad (2.4)$$

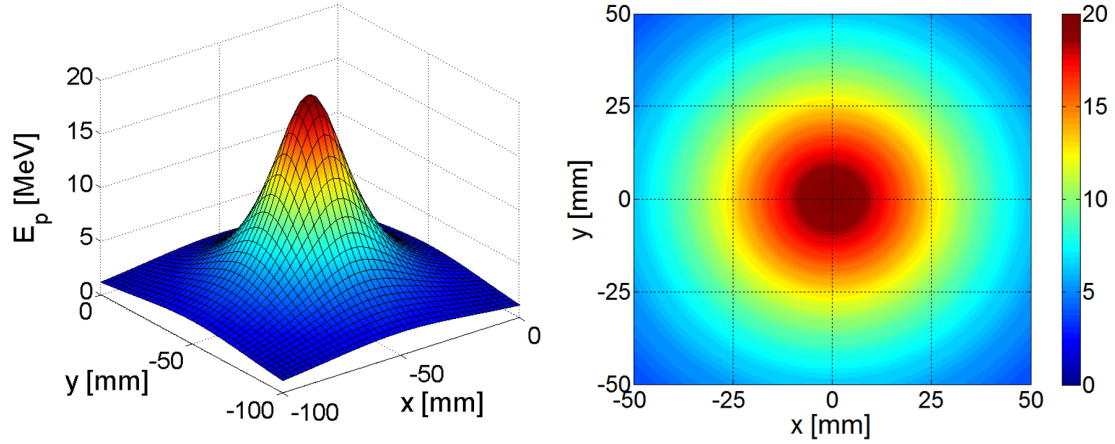


Figure 2.2: Energy distribution - 3-dimensional on the left side plot and 2-dimensional on a screen perpendicular to the electron propagation axis on the right side plot - of the emitted photon at $L = 50$ m downstream the interaction point; the photon is emitted in the head-on collision of a 740 MeV electron, the highest ELI-NP GBS source energy working point, and a 515 nm wavelength photon. The scattered photon energy E_p only depends on the scattering angle θ_f , i.e the energy decreases in circles around z being it independent of the azimuth angle Φ_f .

The highest energy (corresponding to the so called *Compton edge*) of the emitted photon is observed at $\theta_f = 0$ and it decreases with the θ_f increasing ($\theta_f=[0:\pi]$); more detail in it is possible, in principle, to select a desired photon energy with a simple geometrical collimation system and by properly choosing its acceptance angle Ψ . If we assume an head-on collision, $\theta_i = \pi$ and $\theta_p = \pi - \theta_f$ the equation (2.4) becomes

$$E_p = E_L \frac{1 + \beta_i}{(1 - \beta_i \cos \theta_f) + (1 + \cos \theta_f) \frac{E_L}{E_e}} \quad (2.5)$$

which is independent from the azimuthal angle Φ_f . This means that, given the energies of the incident electron and photon, E_e and E_p , the scattered photon energy E_p only depends on the scattering angle θ_f , i.e the energy decreases in circles around z being it independent of the azimuth angle Φ_f . The relation between the scattered photon energy E_p and scattering angle θ_f is demonstrated in Figure 2.2 that shows the energy distribution - 3-dimensional on the left side plot and 2-dimensional on a screen perpendicular to the electron propagation axis on the right side plot - of the emitted photon at $L = 50$ m downstream the interaction point; the photon is emitted in the head-on collision of a 740 MeV electron, the highest ELI-NP GBS source energy working point, and a 515 nm wavelength photon. In this figure, the scattered photon energies E_p are associated to the

colours in the sidebar (in MeV) and the scattering angles θ_f are represented by the radii R of the circles, i.e, $\theta_f = R/L$. We can see that the scattered photons with higher energies are concentrated around the centre ($\theta_f = 0$), while lower energy photons are distributed away from the centre and that the maximum energy corresponds to $\theta_f = 0$, i.e when the photon is scattered into the backward direction of the incident photon (sometimes called backscattering).

For a small scattering angle ($\theta_f \ll 1$) and an ultra-relativistic electron ($\gamma \gg 1$), the (2.5) can be simplified to

$$E_p \approx \frac{4\gamma_i^2 E_L}{1 + \gamma_i^2 \theta_f^2 + 4\gamma_i^2 \frac{E_L}{E_e}} \quad (2.6)$$

Neglecting the recoil effect (2.6) can be reduced to the result given by the *relativistic Thomson scattering* theory [56] $E_p \simeq 4\gamma_i^2 E_L$; so in the Thomson approximation on axis the incoming photon is boosted by a factor $\sim 4\gamma_i^2$ by the relativistic electron and the emitted photon energy reaches its maximum value; therefore the Compton scattering can be used to produce high energy photons in the X/γ range.

The (2.6) is plotted in Figure 2.2 in the Thomson approximation for several electron energies, each corresponding to the ELI-NP GBS source energy working point; the figure shows not only that the emitted photon energy depends on the electron energy (γ_i), but also that, since it decreases as $\gamma_i^2 \theta_f^2$, the photon energy distribution narrows at higher electron energies.

The (2.3) can be also expressed in terms of wavelength and angles:

$$\lambda_p = \lambda_L \left(\frac{1 - \beta_i \cos \theta_f}{1 - \beta_i \cos \theta_i} \right) + \frac{h}{\gamma_i m c} \left(\frac{1 - \cos \theta_p}{1 - \beta_i \cos \theta_i} \right) \quad (2.7)$$

Looking at (2.7) it is worth mentioning that the emitted wavelength is the sum of two contributions: the first term on the right side of (2.7) represents the classical Thomson effect λ_T , while the second part is related to the red-shift due to the inelastic electron recoil λ_R and referred as ‘‘Compton recoil’’. The latter gains importance as the electron energy goes into the GeV range, when the desired bandwidth is very thin or when the laser energy is extremely high, and is given by (see [57])

$$\Delta = 2 \frac{\lambda_p - \lambda_T}{\lambda_p + \lambda_T} \quad (2.8)$$

or

$$\Delta = \frac{4\gamma E_L}{E_0 + 2\gamma E_L} \quad (2.9)$$

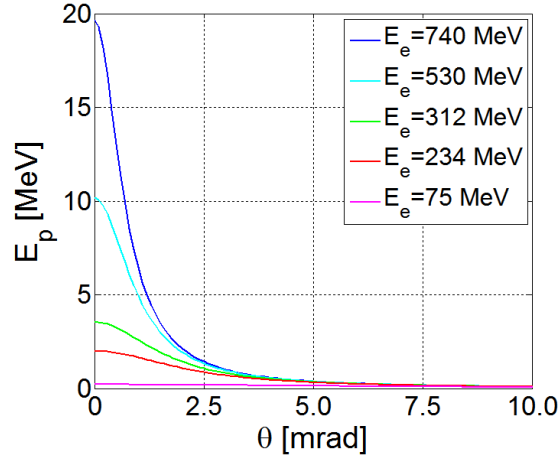


Figure 2.3: Photon energy as function of the scattering angle θ_f result of the scattering of an electron and a 515 nm wavelength photon. The (2.6) is plotted in the Thomson approximation for several electron energies, each corresponding to the ELI-NP GBS source energy working point; the emitted photon energy depends on the electron energy (γ_i) and, since it decreases as $\gamma_i^2 \theta_f^2$, the photon energy distribution narrows at higher electron energies.

with E_0 the electron rest mass. Thus the emitted photon energy can be expressed as (see [58, Intro.])

$$E_{ICS} = E_{TH}(1 - \Delta) \quad (2.10)$$

where E_{ICS} is the source energy in the Compton model and E_{TH} is the source energy in the classical Thomson model. For example, the behaviour of the source energy and of the Compton recoil Δ as function of the electron beam energy has been calculated in 3.2 for the ELI-NP GBS source and establishes the required electron beam energy to range between 75 - 740 MeV. In our range of interest (up to 1 GeV) the Thomson effect is definitely the dominant effect, even if to neglect the recoil effect causes some percent shift in the wavelength value, which is not a small shift compared to the relative bandwidth of 0.5% or even less desired for the ELI-NP experiment.

2.2 Beam-beam Scattering

The features of a photon beam emitted in the Compton scattering of a laser beam and an electron beam, i.e in a beam-beam scattering, can be derived from the above considerations on the electron-photon collision, being it equivalent to the scattering between

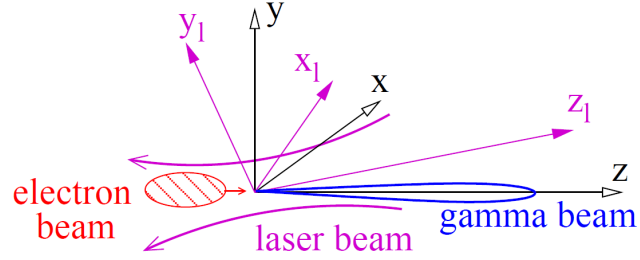


Figure 2.4: Geometry of Compton scattering of an electron and a photon in a laboratory frame coordinate system (x, y, z) in which the electron is incident along the \underline{z} direction. The incident photon beam is propagating along the negative z_l -axis direction in its coordinate system (x_l, y_l, z_l) . The coordinate systems (x, y, z) and (x_l, y_l, z_l) share the same origin.

a mono-energetic electron beam and a mono-energetic laser beam with zero transverse sizes.

The Figure 2.2 shows Compton scattering of an electron beam and a laser pulse in the laboratory frame. Geometry of Compton scattering of an electron beam and a photon beam in the laboratory frame coordinate system (x, y, z) in which the electron is incident along the \underline{z} direction. The incident photon beam is propagating along the negative z_l -axis direction in its coordinate system (x_l, y_l, z_l) . The coordinate systems (x, y, z) and (x_l, y_l, z_l) share the same origin. The time $t = 0$ is chosen for the instant when the centre of the electron beam and laser pulse arrive at the origin. The definition of these two coordinate systems allows the study of the Compton scattering process with an arbitrary collision angle, i.e, the angle between z -axis and negative z_l -axis. For a head-on collision, the collision angle equals π . In this case, the electron and laser coordinate systems coincide. In these coordinate systems, the electron and laser beams can be described by their respective distribution functions $f_e(\underline{r}, \underline{p}, t)$ and $f_L(\underline{r}, \underline{k}, t)$. The number of the emitted photons per unit time dt and phase space volume $d\underline{p} d\underline{k} dV$ generated in the interaction is defined as

$$dN(\underline{r}, \underline{p}, \underline{k}) = \sigma_{tot}(\underline{p}, \underline{k})c(1 - \underline{\beta}_i \cdot \underline{e}_k)N_e f_e(\underline{r}, \underline{p}, t)N_L f_L(\underline{r}, \underline{k}, t)d\underline{p} d\underline{k} dVdt \quad (2.11)$$

where σ_{tot} is the Compton cross section and depends only on the momenta of the incoming electron and photon, N_e and N_L are the total number electrons and photons and

$c(1 - \underline{\beta}_i \cdot \underline{e}_k)$ is the relative velocity of the two beams. The total number of scattered photons can be obtained integrating the (2.11) on time, volume and momenta.

The Compton cross section in the Lorentz invariant form has been calculated in [59, 60, 61] by using Quantum Electrodynamics (QED) theory; after some manipulations the total cross section can be obtained for unpolarized electrons scattering with polarised photons as follows [62]

$$\sigma_{tot} = 2\pi r_e^2 \frac{1}{X} \left\{ \left(1 - \frac{4}{X} - \frac{8}{X^2} \right) \log(1+X) + \frac{1}{2} + \frac{8}{X} - \frac{1}{2(1+X)^2} \right\} \quad (2.12)$$

where r_e is the *classical electron radius* and X is one of the Lorentz invariant variables defined as follows

$$X = \frac{s-(mc)^2}{(mc)^2} \quad Y = \frac{(mc)^2-u}{(mc)^2}$$

where m is the electron mass at rest, $s = (p_i+k_i)^2$, $u = (p_i-k_f)^2$ and X and Y satisfy the inequalities $\frac{X}{X+1} \leq Y \leq X$ [59].

Neglecting the recoil effect the (2.13) can be reduced to the *classical Thomson cross section*:

$$\sigma_{tot}^{TH} = \frac{8\pi r_e^2}{3} (1-X) \approx \frac{8\pi r_e^2}{3} = 0.67 \text{ barn} \quad (2.13)$$

In the case of an head-on collision occurring at the waists of both beams the total number of photons per shot can be approximated by

$$N = L_s \sigma_{tot} \simeq \frac{N_e N_L}{2\pi \Sigma_i} \sigma_{tot} \quad (2.14)$$

where L_s is the single collision luminosity and Σ_i is

$$\Sigma_i = \sqrt{\sigma_x^2 + \frac{w_0^2}{4}} \sqrt{\sigma_y^2 + \frac{w_0^2}{4}} \quad (2.15)$$

with σ_i the transverse rms electron beam size ($i=x,y$) and w_0 is the laser focal spot size at collision. The (2.14) is valid whenever we can neglect the diffraction of both the electron beam and the laser beam across the interaction (focal) plane. It means that, given the beta function $\beta = \frac{\gamma \sigma_i^2}{\varepsilon_n}$ and the length σ_z of the electron beam, it has to be verified $\sigma_z \leq \beta$ being ε_n and σ_i the transverse normalise emittance and spot size at the interaction point; similarly, given the Rayleigh range $Z = \frac{\pi w_0^2}{\lambda_L}$ and the length σ_{zL} of the laser pulse, it has to be verified $\sigma_{zL} \leq Z$ (to avoid luminosity degradation due to the well-known hour-glass effect, that is detailed described in [6]). The (2.14) can be also

expressed as follows in terms of laser pulse energy E_L , electron beam charge Q , laser photon energy $h\nu_L$

$$N = 4.12 \cdot 10^8 \frac{E_L[J]Q[pC]}{h\nu_L[eV]\Sigma_i[\mu m^2]} \quad (2.16)$$

with $\sigma_{tot} = \sigma_{tot}^{TH}$.

2.3 Scaling Laws

The simple model introduced above permits to deduce very useful *scaling laws* [63] to evaluate analytically the characteristics of the photon beam produced by the Compton backscattering of the two colliding beams.

A very useful scaling law for the total number of photons emitted in a cone of rms emi-angle θ_{rms} can be derived from (2.17), that represents the total number of scattered photons per second over the entire solid angle and the entire energy spectrum. Assuming, in fact, an electron beam with circular transverse section of radius σ_t ; the photon number for a single shot scales as:

$$N_\gamma^{bw} = 0.35 \cdot 10^9 \frac{E_L[J]Q[pC]}{h\nu_L[eV]\Sigma_i[\mu m^2]} \Psi^2 \quad (2.17)$$

where σ_{tot} has been assumed equal to σ_{tot}^{TH} and $\Psi = \gamma_i \theta_{rms}$ is the acceptance angle of the collimation system; thus for example the number of photons emitted in the cone of rms emi-angle θ_{rms} scales nearly like the square of Ψ or like the inverse square of the Σ_i , and so on and so forth.

Any Compton source is a polychromatic source of back-scattered photons and, as mentioned in 2.1, in order to produce a monochromatic photon beam one needs to select a narrow cone around the electron beam propagation axis by means of special collimators. So what really matters for experiments and applications of the collimated photon beams, is the number of photons N_γ^{bw} carried by the back-scattered radiation pulse within a small angle, and the rms bandwidth associated with it ν_p - that is the concept of spectral luminosity and spectral density, which are the real figure of merit for Nuclear Physics and Photonics applications. The Spectral Density in the bandwidth in a single shot is typically expressed in units of photons/s · eV and is defined as

$$SPD_r = \frac{N_\gamma^{bw}}{\sqrt{2\pi}h[\frac{\Delta\nu}{\nu}]_r} \quad (2.18)$$

From (2.3) is possible to deduce the source bandwidth $\frac{\Delta v}{v}$, that scales with the quadratic sum of contributes due respectively to the acceptance Ψ , to the electron normalised emittance ε_n and energy spread $\Delta\gamma/\gamma$ and to the laser natural bandwidth $\Delta v_0/v_0$, diffraction d and temporal profile σ_{zL} :

$$\begin{aligned} \left[\frac{\Delta v_p}{v_p} \right]_{\Psi} &\approx \frac{\Psi^2}{\sqrt{12}} \\ \left[\frac{\Delta v_p}{v_p} \right]_{\varepsilon_n} &\approx \left[\frac{\varepsilon_n}{\sigma_x} \right]^2 \\ \left[\frac{\Delta v_p}{v_p} \right]_{\gamma} &\approx \left[\frac{2\Delta\gamma}{\gamma} \right] \\ \left[\frac{\Delta v_p}{v_p} \right]_d &\approx \left[\frac{M^2 \lambda_L}{2\pi w_L} \right]^2 \\ \left[\frac{\Delta v_p}{v_p} \right]_{v_L} &\approx \left[\frac{\Delta v_L}{v_L} \right] \\ \left[\frac{\Delta v_p}{v_p} \right]_{\sigma_{zL}} &\approx \left[\frac{a_0^3/3}{1+a_0^2/2} \right] \end{aligned}$$

where $a_0 = 4.3 \frac{\lambda_L}{w_0} \text{sqrt} \left(\frac{U[J]}{\sigma_{zL}[\text{ps}]} \right)$ and in $\left[\frac{\Delta v_p}{v_p} \right]_{\gamma}$ have been neglected the terms due to the presence of the quantum frequency recoil. The term $\left[\frac{\Delta v_p}{v_p} \right]_{\sigma_{zL}}$ represents the non-linear effects due to the laser intensity responsible for multi-photon absorption/scattering phenomena; these non-linear effects, strongly dependent on the interacting laser energy, must be minimised in narrow bandwidth Inverse Compton Sources, as those for Nuclear Physics and Photonics, by using laser pulses with $a_0 \ll 1$.

Finally the relative bandwidth can be expressed as in the following formula

$$\frac{\Delta v_p}{v_p} = \sqrt{\left[\frac{\Psi^2}{\sqrt{12}} \right]^2 + \left[\frac{\varepsilon_n}{\sigma_x} \right]^4 + \left[\frac{\Delta v_p}{v_p} \right]_{\gamma}^2 + \left[\frac{\Delta v_p}{v_p} \right]_L^2} \quad (2.19)$$

whit $\left[\frac{\Delta v_p}{v_p} \right]_L$ including all the collision laser contribution to the source bandwidth. Once the bandwidth has been fixed at the required value $\left[\frac{\Delta v_p}{v_p} \right]_r$ one can calculate the corresponding acceptance as follows

$$\Psi_r^2 \approx \sqrt{\left[\frac{\Delta v_p}{v_p}\right]_r^2 - \left[\frac{\varepsilon_n}{\sigma_x}\right]^4 - \left[\frac{\Delta v_p}{v_p}\right]_\gamma^2 - \left[\frac{\Delta v_p}{v_p}\right]_L^2} \quad (2.20)$$

Looking at (2.20) it is worth mentioning that for beams characterized by high focusing, the term $\left[\frac{\Delta v_p}{v_p}\right]_{\varepsilon_n}$ dominates in the bandwidth, thus limiting the collection of the photons to a small acceptance angle. Lower focusing decreases the transverse momenta of the electrons in the interaction region and permits to increase the acceptance, nevertheless lower focusing means also a photon number in the shot decreasing, and so a compromise is needed in order to optimise the spectral density of the source. These formulas have been applied to the ELI-NP GBS case study and validated thanks to comparisons with the simulated results obtained by Monte-Carlo codes, as CAIN [58, Ch.1],[63].

ELI-NP GBS Linac

Contents

3.1	An advanced high brilliance γ source	23
3.2	Accelerator Design Criteria	28
3.3	The RF Linac Layout	30
	The Photo-injector	31
	The C-band Booster Linac	34
	Diagnostic Tools	35
3.4	RF Linac Start to End Simulations	36
	The Photo-Injector	36
	The C-band Booster Linac	40
	Wakefield Effects in Single and Multi-bunch Operation	43
	Quasi-constant Gradient C-band cavities	51
3.5	Machine Sensitivity Studies	54
3.6	Dark Current Evaluation	61
3.7	Final Considerations	66

3.1 An advanced high brilliance γ source

The ELI-NP Gamma Beam System (GBS) is a high spectral density and monochromatic γ photon source based on the Inverse Compton Scattering process, that will be

installed at the Magurele site (close to Bucharest in Romania) in 2017 and it is one of the ELI project pillars.

The Extreme Light Infrastructure (ELI) project is part of a European plan to build a new generation of large research facilities selected by the European Strategy Forum for Research Infrastructures (ESFRI). The main goal of ELI is to provide ultra-short laser pulses of a few femtoseconds (10-100 fs) duration and give performance up to 10 PW and it bring new techniques for medical image-display and diagnostics, radiotherapy, tools for new materials developing and testing, latest in X-ray optics. ELI will be implemented as a distributed research infrastructure based initially on 3 specialised and complementary facilities:

- **ELI attosecond** is located in Hungary where a new building is being built on an old Soviet military base in the northern part of Szeged next to the number 5 main road. The primary mission of the ELI-ALPS Szeged research facility is to make a wide range of ultrashort light sources accessible to the international scientific community user groups. Laser driven secondary sources emitting coherent extreme-ultraviolet (XUV) and X-ray radiation confined in attosecond pulses is a major research initiative of the infrastructure. The secondary purpose of the facility is to contribute to the necessary scientific and technological developments required for high peak intensity and high power lasers.
- **ELI Beamlines** is located in the Czech Republic in the Central Bohemia region, near Prague. Here it will be creates a new generation of secondary sources for interdisciplinary applications in physics, medicine, biology and material sciences. Thanks to the tunability of its laser system, the ELI Beamlines facility will be able to deliver high-quality sources of various kinds adapted to the needs of a large variety of users.
- **ELI-NP (Nuclear Physics)** is located in Romania where a new building is being built in Magurele, near Bucharest. It will focus on laser-based nuclear physics and will generate radiation and particle beams with much higher energies, brilliances suited to studies of nuclear and fundamental processes.

The EuroGammaS Consortium is in charge of providing the design, manufacturing, delivery, installation, testing and commissioning of the Gamma Beam System (GBS), for the benefit of the ELI-NP project, managed by the Horia Hulubei National Institute for Physics and Nuclear Engineering Bucharest - Magurele. The “EuroGammaS

”Association is composed by the Istituto Nazionale di Fisica Nucleare, the “Association leader”, the Università degli Studi di Roma “La Sapienza”, the Centre National de la Recherche Scientifique, ACP S.A.S., Alsym S.A.S., Comeb Srl, ScandiNova Systems AB.

At the Nuclear Physics pillar of ELI the scientific advanced potentials will be explored of a high intensity laser system (up to 10^{24} W/cm²) joined with a high brilliance Gamma ray Beam System, in the field of Nuclear Physics and Nuclear Photonics for users, not yet addressable nowadays. Such a γ photon beam is meant to provide a source with unprecedented quality, as already mentioned, in terms of small bandwidth (0.5 %), very high spectral density ($> 10^4$ photons/sec/eV) and peak brilliance ($> 10^{21}$) in the wide energy range 0.2 - 19.5 MeV. It opens the era of nuclear photonics and pursues advanced applications in the field of national security, material and life sciences, nuclear waste treatment, nuclear medicine, as well as fundamental studies in nuclear physics dealing with the nucleus structure and the role of giant dipole resonances, of great relevance also for astrophysics studies and answer questions concerning star nucleosynthesis.

At the ELI-NP GBS the γ beam is produced in the head-on collision of the high quality high brightness electron beam with maximum energy 740 MeV and a high quality high power ps laser beam; it represents a steep forward jump in the available technologies in comparison to the present state of the art, with an expected step-up of the various beam performances by at least two orders of magnitude, in particular the spectral density, figure of merit for Nuclear Physics and Photonics applications that has to be increased up to 10^4 photons/sec/eV for the ELI-NP source. Beside the ultra high quality of the electron beams the upgrade comes from the operation at 100 Hz repetition rate for the RF in the multi-bunch configuration and to recirculate the laser pulse as many times as possible at the IP. The use of a multi-bunch train colliding with a high intensity recirculated laser pulse allows to increase the number of collision per second, and so the gamma flux.

The Figure 3.1 shows the machine layout, while the expected performances and the source specifications are listed in Table 3.1. The completion of ELI-NP-GBS by EuroGammaS is foreseen by the end of 2018 and so an intense study campaign has been performed to optimise the RF linac to ensure the required performances (Table 3.1) and a reliable routine operation of the γ source.

In the first and second sections of this chapter the design criteria and the layout of the RF linac are illustrated; then in the following sections the optimisation is described

Table 3.1: Summary of γ ray beam specifications and expected performances for electron beam and collision laser pulse.

Electron Beam Parameters @IP		
all values are rms		
Bunch charge, Q	25 – 400	pC
Mean Energy, E_e	75 – 740	MeV
Relative Energy Spread, $\frac{\Delta\gamma}{\gamma}$	0.4 – 1.0	%
Bunch Length, σ_z	200 – 300	μm
Spot Size, σ_r	15 – 30	μm
Normalised Transverse Emittance, ϵ_n	0.4-0.6	mm mrad
# Bunches in the train,	≤ 32	
Repetition Rate	100	Hz
Bunch separation, T_b	16	ns
Energy variation in the train, ΔE	≤ 1	%
Emittance dilution due to beam break – up	≤ 10	%
Pointing jitter	1	μm

Yb:Yag Collision Laser Beam Parameters @IP		
Pulse Energy	0.2 – 0.4	J
Wavelength	515	nm
Photon Energy	2.4	eV
Pulse Length [r.m.s.]	1.5	ps
Spot Size w_0	> 28	μm
Bandwidth [r.m.s.]	< 0.1	%
M^2	< 1.2	
a_0	0.02 – 0.04	
Collision Angle α	172	deg
Repetition Rate	100	Hz
Recirculator Rate per Laser Pulse	32	

γ –ray Photon Beam Specifications		
Energy	0.2 – 19.5	MeV
Spectral Density	$0.8 – 4.0 \cdot 10^4$	ph/s·eV
Peak brilliance	$10^{20} – 10^{23}$	ph/s·mm ² ·mrad ² ·0.1%
Bandwidth [r.m.s.]	≤ 0.5	%
Source size [r.m.s.]	10 – 30	μm
Pulse length [r.m.s.]	0.7-1.5	ps
# photons/shot within FWHM bandwidth	$\leq 2.6 \cdot 10^5$	
# photons/second within FWHM bandwidth	$\leq 8.3 \cdot 10^8$	

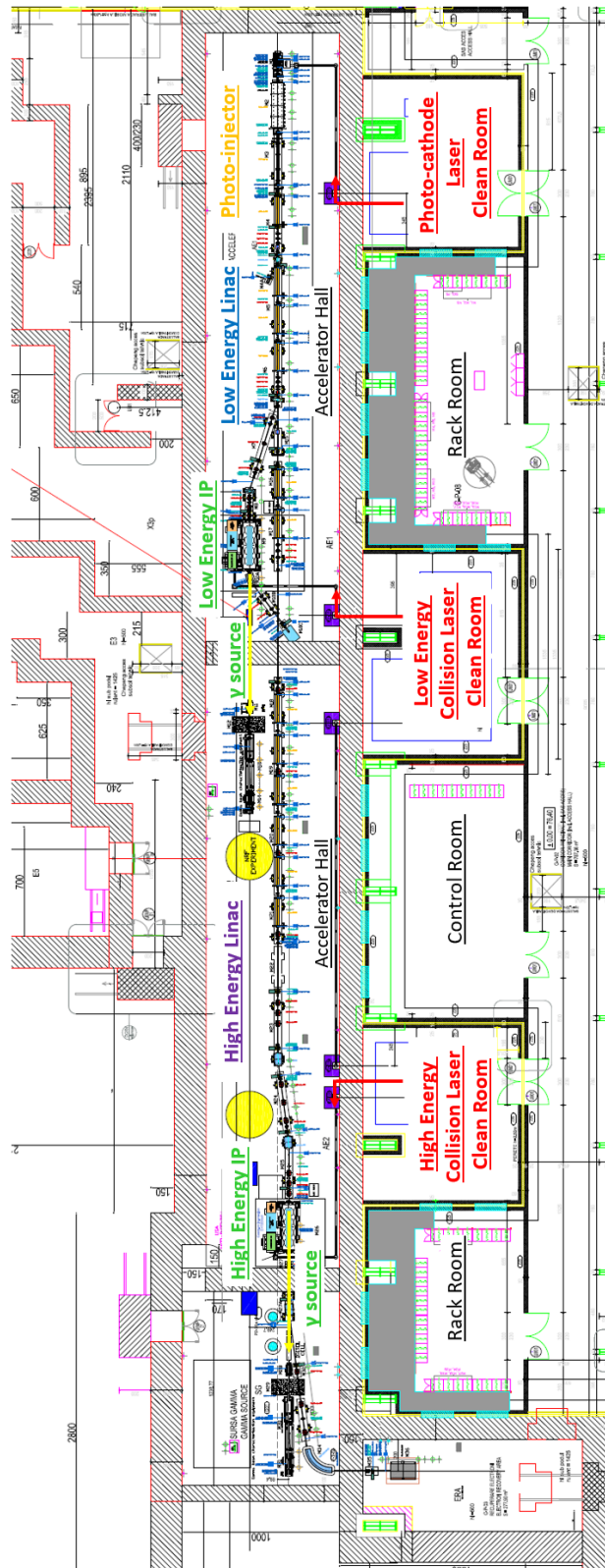


Figure 3.1: ELI-NP Gamma Beam System (GBS) layout: a SPARC-like S-band high brightness injector [49] followed by two C-band RF linacs (low and high energy) that through the relative transfer lines provide the electron beam to the Low and High Energy Interaction Points (LE IP and HE IP) respectively [58].

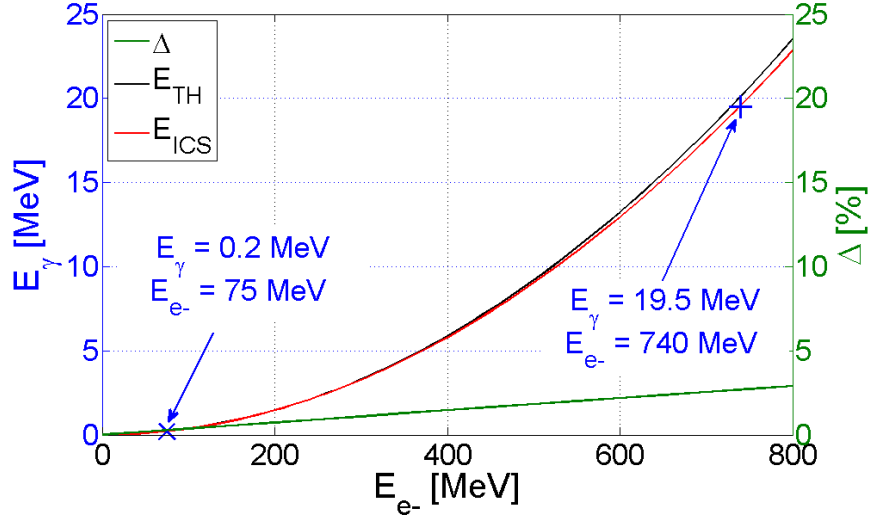


Figure 3.2: Behaviour of the source energy E_{ICS} and of the Compton recoil Δ as function of the electron beam energy E_{e^-} . The electron beam energy is established to range between 75 - 740 MeV

of the 250 pC electron beam dynamics to guarantee the desired values for the electron beam emittance and energy spread also including the wakefields effects, both in single and multi-bunch operation, and the quasi-constant gradient C-band cavities; then the analysis of the robustness of the linac design is addressed regarding machine element jitters and misalignments and on this basis alignment procedure and jitter tolerances have been provided; in the last section is described the analysis related to evaluation of the dark current along the RF linac.

3.2 Accelerator Design Criteria

The stringent requirements on the ELI-NP γ source spectral density - $0.8 - 4.0 \cdot 10^4$ ph/s·eV - and bandwidth - $<0.5 \%$ - in the desired energy range - 0.2 - 19.5 MeV - provide the basis for the accelerator design criteria.

As mentioned in 2 the frequency of the emitted radiation depends on the electron beam energy as in (2.10), here reported

$$E_{ICS} = E_{TH}(1 - \Delta) \quad (3.1)$$

A 740 MeV electron beam colliding with the laser pulse described in Table 3.1 generates a 19.5 MeV photon beam where $\Delta \approx 0.54$ MeV. The behaviour of the source energy

and of the Compton recoil Δ as function of the electron beam energy is reported in Figure 3.2. The ELI-NP GBS required electron beam energy ranges between 75 - 740 MeV.

The spectral density in the required r.m.s. bandwidth $[\frac{\Delta v}{v}]_r$ can be described as follows (3.1)

$$SPD_r = \frac{N_\gamma^{bw}}{\sqrt{2\pi}h[\frac{\Delta v}{v}]_r} \quad (3.2)$$

Being the number of number of photons in the bandwidth, N_γ^{bw} , and the r.m.s. value of the bandwidth itself, $\frac{\Delta v}{v}$, described as in 2.3, is possible to define from eq. 3.12 the following factor of merit $\hat{\eta}$ for the electron beam

$$\hat{\eta} = \frac{Q_b}{\sigma_t^2 [(\frac{\Delta \gamma}{\gamma})^2 + (\frac{\epsilon_n}{\sigma_t})^4]^{\frac{1}{2}}} \quad (3.3)$$

where ϵ_n is the transverse normalized emittance, σ_t is the transverse spot size, $\Delta\gamma/\gamma$ is the energy spread and Q_b is the charge of the electron beam at the interaction point (IP). In this form $\hat{\eta}$ scales like the spectral density of the emitted radiation [64, eq. 3-5], and points out the relevance of electron beam emittance and energy spread contribution to the radiation quality.

In a high brightness linac the longitudinal and transverse phase spaces are not strongly coupled, especially in the photo-injector where the energy is still low and low bunch compression is foreseen; so it can be assumed that the transverse emittance can be minimised, for a given charge, independently on the beam energy spread and a new qualifying parameter η can be identified

$$\eta = \frac{Q_b}{\epsilon_n^2} \quad (3.4)$$

In this form η represents the 4D electron phase space density to maximise.

Based on above considerations an intense study has been performed to optimise the final source design as reported in ELI-NP official Technical Design Report (TDR) [58]; here the chosen electron beam parameters are: ϵ_n in the range 0.2 – 0.6 mm mrad, $\Delta\gamma/\gamma \leq 0.1\%$ and tunable energy in the range 75 – 740 MeV. As reported in [58, Ch. 1] the behaviour of the source spectral density as function of the electron beam spot size indicates $15 \mu m \leq \sigma_t \leq 30 \mu m$ as the optimal range for the electron beam spot size at the interaction point with the best result for $\sigma_t \approx 20 \mu m$.

The linac optimisation (exhaustive description for the ELI-NP case is reported in [65]) has been divided in two parts:

1. minimisation of ε_n to maximise η ;
2. minimisation of the energy spread to preserve the source bandwidth.

The ε_n minimisation requires a bunch long enough in the RF gun to reduce the emittance growth due to the space charge contribution, it is ensured with a SPARC-like S-band photo injector [49]. Here the gun emittance compensation solenoid, together with the gradients on following TW S-band cavities set to satisfy the invariant envelope conditions, providing a “frozen” ε_n at the photo-injector exit (see ??).

The energy spread minimisation is obtained with a slightly off-crest operation in the C-band RF linac, following the S-band photo injector, and it guarantees electron beam energy in the range 75 - 740 MeV, taking advantage of the high accelerating gradients provided by the C-band cavities to compact its length. The final energy spread induced by to the RF curvature $\frac{\Delta\gamma}{\gamma}$ can be described in terms of bunch length and accelerating frequency and is shown in (3.3)

$$\frac{\Delta\gamma}{\gamma} \approx 2 \left(\frac{\pi f_{RF} \sigma_z}{c} \right)^2 \quad (3.5)$$

where an on crest operation, in full relativistic conditions has been considered.

To avoid the energy spread dilution due to RF curvature degradation effects keeping $\Delta\gamma/\gamma \leq 0.1\%$, a $\sigma_z \leq 280\mu m$ must be injected in the C-band linac, see Figure 3.3. A velocity bunching scheme is applied in the first S-band accelerating section, resulting in a gentle compression factor $f \leq 3$; the emittance degradation due to a shortened bunch its kept under control by means of a solenoid around the first S-band section, as routinely and successfully applied at SPARC_LAB.

3.3 The RF Linac Layout

The application of the above mentioned accelerator design criteria results in a hybrid scheme consisting in a SPARC-like S-band high brightness photoinjector [49] followed by a C-band RF linac as shown in Figure 3.4. The 100 Hz repetition rate and the multibunch configuration provide the demanding requirement of high spectral density, enabling in this way to accelerate up to 40 bunches in the same 450 ns long RF pulse with a 15-20 ns spacing to raise the effective repetition rate up to a ~ 4 kHz value. The

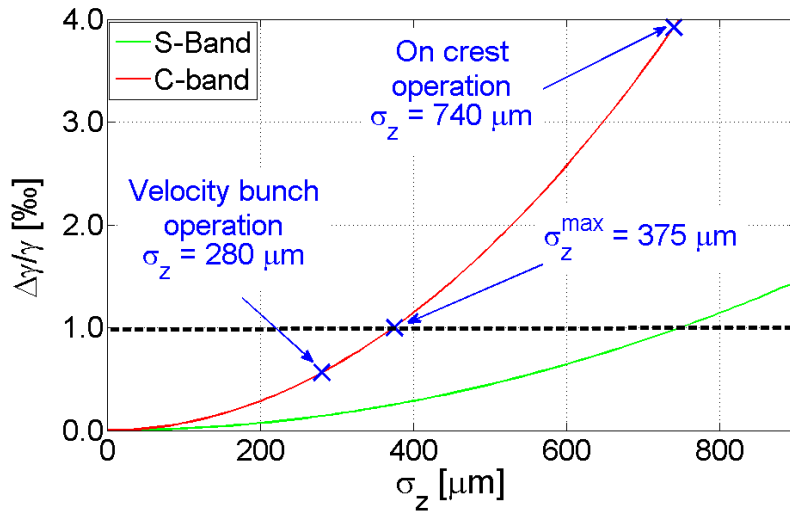


Figure 3.3: Behaviour of the energy spread dilution due to RF curvature degradation effects as function of the bunch length and of the accelerating frequency in the on crest operation and full relativistic conditions. At ELI-NP GBS the choice has been to inject a $\sigma_z \leq 280 \mu\text{m}$ in the C-band linac to avoid $\Delta\gamma/\gamma > 0.1\%$. This is obtained by means of the adopted velocity bunching scheme, resulting in a gentle longitudinal compression factor < 3 at the photo injector exit, as routinely and successfully applied at SPARC-LAB.

routinely multi-bunch operation at the ELI-NP GBS foresees the collision of a train of 32 electron bunches, separated by almost 16 ns and each one carrying 250 pC of charge, with a high intensity recirculated laser pulse.

The Photo-injector

The SPARC-like S-band injector, operating at 2.856 GHz, is composed of a 1.6 cell S-band RF gun equipped with a copper photo cathode and an emittance compensation solenoid, followed by two TW SLAC type S-band sections [66]; a second compensation solenoid surrounds the first S-band cavity for the operation in the velocity bunching scheme. The whole system have been already mounted and aligned at INFN-LNF laboratories in 2016 as illustrated in Figure 3.5, and is hosted on three independent modules 4 m long each: the RF gun and the gun solenoid are on the first module (M1), while the S-band structures on the following ones (M2 and M3).

The RF gun will operate at the accelerating peak field gradient $E_{acc} \approx 120 \text{ MV/m}$, while the two S-band structures will operate at a maximum of 23.5 MV/m allowing to reach a maximum electron beam energy at the injector exit of 146 MeV on crest.

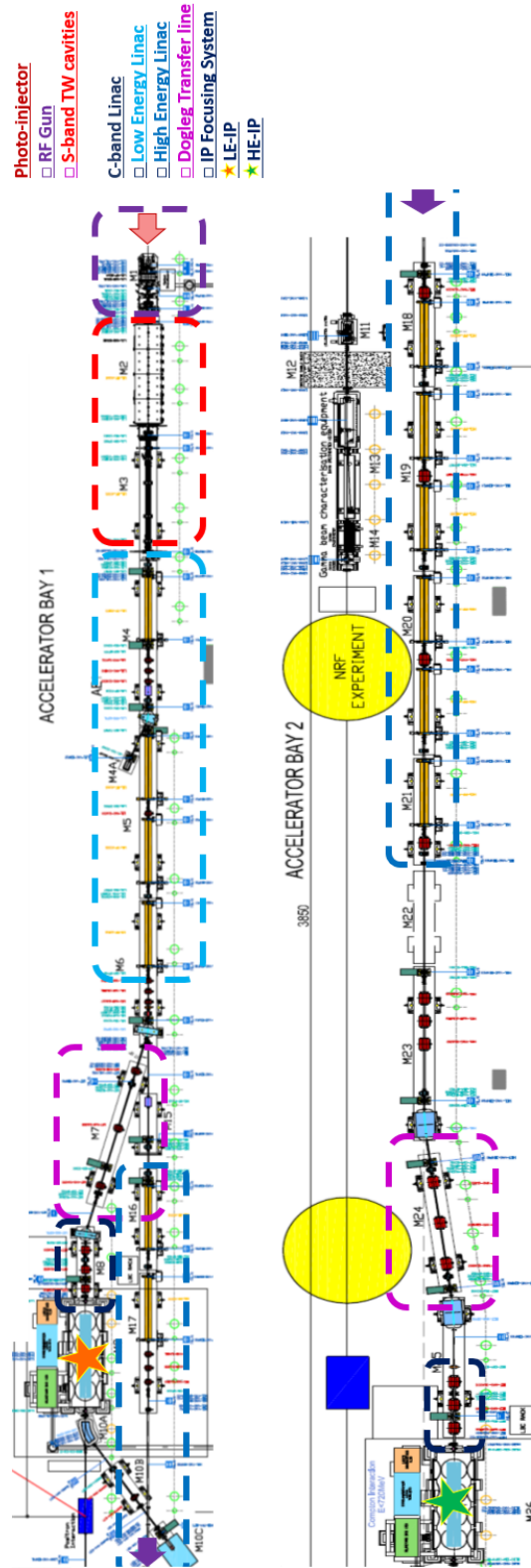


Figure 3.4: ELI-NP Gamma Beam System (GBS) layout: a SPARC-like S-band high brightness injector [49] followed by two C-band RF linacs (low and high energy) that through the relative transfer lines provide the electron beam to the Low and High Energy Interaction Points (LE IP and HE IP) respectively [58].

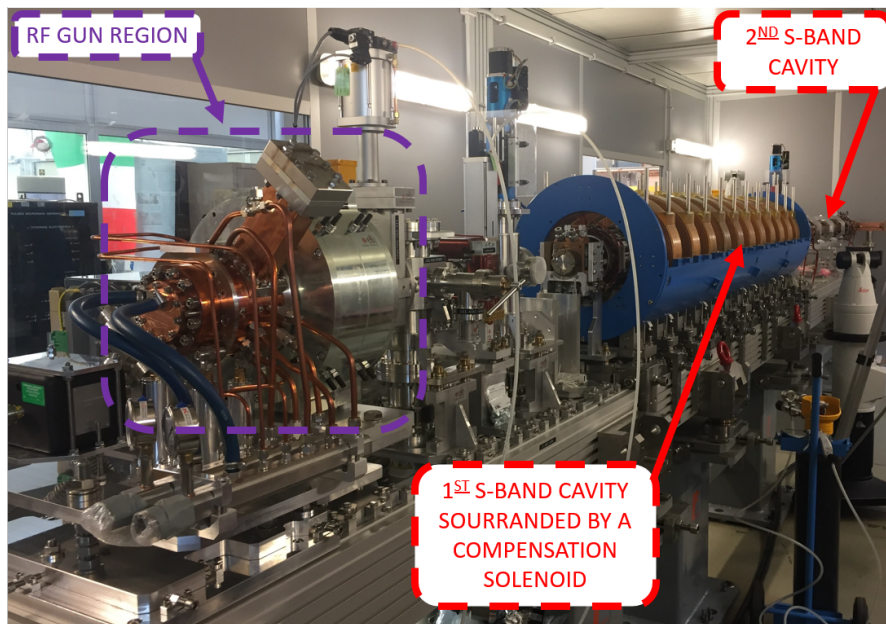


Figure 3.5: The whole system have been already mounted and aligned at INFN-LNF laboratories and is hosted on three independent modules: the RF gun and the gun solenoid are on the first module (M1), while the S-band structures on the following ones (M2 and M3).

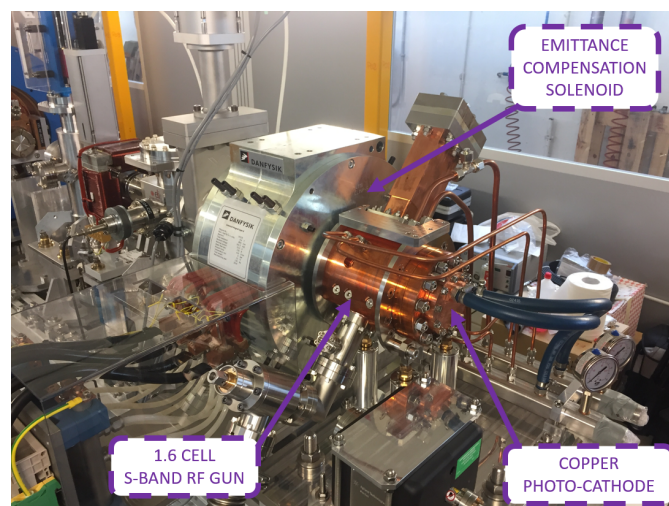


Figure 3.6: The RF gun region is composed of a 1.6 cell S-band RF gun, operating at 2.856 GHz, equipped with a copper photo cathode and an emittance compensation solenoid.

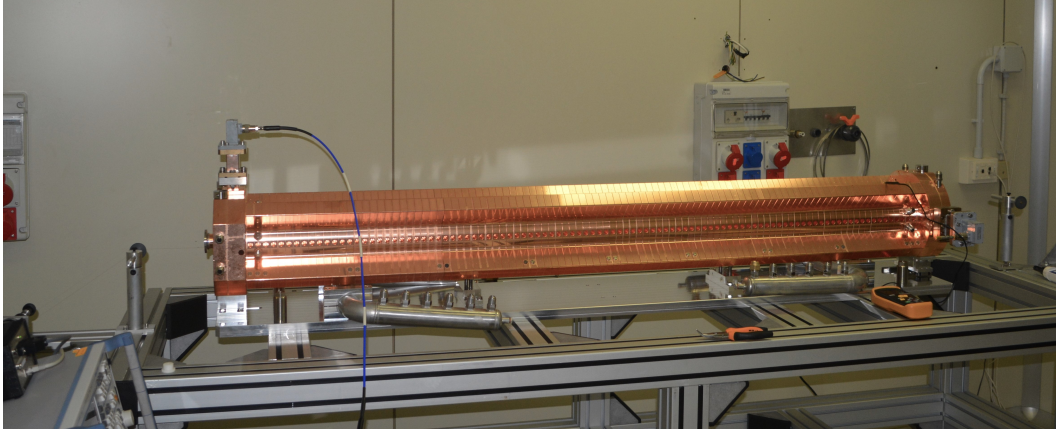


Figure 3.7: The C-band accelerating structures are 1.8 m long and consist of 102 cells with a $2\pi/3$ phase advance per cell. The cavities will be hosted at INFN-LNF laboratories until the commissioning phase; here the vacuum tests for some of them have already started.

The gun region is one of the most critical part of the accelerator where the emittance compensation process takes place; the design of this part has been carefully studied and foresees the possibility to slightly tune the drift space between the injector elements in order to satisfy the invariant envelop condition and optimise the beam parameters at the first TW section entrance. The gun solenoid consists in two coils that can be powered independently with alternate signs providing the compensation for eventual alignment errors and residual multipolar components. A steerer, placed downstream the emittance compensation solenoid, allows to control the electron beam trajectory before the injection in the first travelling accelerating section. The Figure 3.6 shows the RF gun region mounted and aligned at INFN-LNF laboratories in 2016.

The C-band Booster Linac

The C-band RF linac operates at 5.712 Ghz, with the accelerating structures designed and developed at LNF, [67] (modules M4-M35). Here the accelerating gradient can be set up to a maximum of 33 MV/m, allowing enough margin for the off crest operation that minimise the final beam energy spread in the whole 75 – 740 MeV energy range [64, 65]. The C-band accelerating structures are 1.8 m long and consist of 102 cells with a $2\pi/3$ phase advance per cell. The cavities will be hosted at INFN-LNF laboratories until the commissioning phase; here the vacuum tests for some of them have already started.

The linac is divided in two main sections as shown in Figure 3.4: the low energy extraction line and the downstream high energy line. The low energy linac is composed of four accelerating sections and can carry the electron beam up to the maximum energy $E \approx 320$ MeV; a dogleg transport line DL1 downstream its exit provides on right side an off axis deviation of ~ 90 cm and delivers the beam at the Low Energy Interaction Point (LE IP). The straight-on branch of the dogleg drives the beam along the downstream high energy linac. It is composed of eight accelerating sections and brings the electron beam up to the maximum energy $E = 740$ MeV; here a second dogleg DL2 delivers the electron beam at the High Energy Interaction Point (HE IP) with a off axis deviation of ~ 120 cm. In each of the two IP's regions a quadrupole triplet provides a flexible final focusing for matching the electron beam spot size vs the counter-propagating laser pulse.

Diagnostic Tools

The electron beam characterisation is essential to properly match the electron beam coming from the RF linac to provide the required phase space orientation at the IP. The beam envelope is captured in several positions along the machine and in particular at the gun exit, at the low and high linac entrance and exit and at the IPs. The imaging on the screen mounted at the gun exit is used for the beam energy measurement, provided by means of the beam deflection a steerer (horizontal or vertical) upstream the screen, and to centre the beam on the photo cathode. The longitudinal phase space characterisation is obtained using a S-band RF deflecting cavity [68] coupled with a dipole in two main locations: downstream the first C-band cavity of the low energy linac and upstream the first C-band cavity of the high energy linac. The 6D phase space characterisation is completed in these places with the emittance measurements by means of the quadrupole scan technique. The latter can be also done at each straight-on section of the linac to keep under control the eventual emittance dilution. Beam current monitors are placed at the gun exit and all along the machine in order to optimise the beam charge transport up to the IP. The current measurements at the gun exit together with a RF injection phase scan enables the identification of the proper injection phase needed to maximise the beam energy gain as indicated by the beam dynamics simulations. Finally the beam trajectory is measured with beam position monitors all along the machine and in particular at the interaction region entrance and exit, where the special cavity BPMs resolution is of the order of $2 - 3 \mu\text{m}$.

3.4 RF Linac Start to End Simulations

Intense beam dynamics studies have been performed to provide a reliable working point for the linac to drive in collision an electron beam able to guarantee the γ -ray source performances (see 3.2). The needed electron beam parameters, checked with CAIN simulations, are described in [69] for different Working Points (WPs), each corresponding to the main user required γ -photon beam energy. The electron beam parameters at the interaction point have been optimised for the 250 pC nominal electron beam with 30 k macro particles in the single bunch operation and are listed in Table 3.2. Looking at the Table 3.2 results it has to be mentioned that for the very low energy 0.20 MeV WP the energy spread turns out to be slightly out of specifications even if still acceptable by the user community.

The ELI-NP GBS nominal case foresees a 80 MeV electron beam coming from the photo-injector with the parameters listed in Table 3.3; the beam transition energy between the space charge and the emittance dominated regime occurs at ≈ 70 MeV. Regarding the beam dynamics simulations, the machine can then be split into two parts with the beam exploring two different regimes (for more details see 1.2): the laminar regime in the photoinjector, where the beam dynamics optimisation is mainly devoted to minimise the space-charge induced emittance; and the emittance-dominated regime (where the total normalised emittance remains constant in an ideal accelerator) in the C-band "booster" linac to gain energy and minimise the $\frac{\Delta\gamma}{\gamma}$. Each electron beam generated in the injector has been tracked along the C-band linac to provide the final beam parameters at the IP.

The Photo-Injector

The photo-injector optimisation aims to provide at the C-band entrance a 250 pC electron beam with $\varepsilon_n \simeq 0.4$ mm mrad, $\sigma_z \simeq 280$ μm and energy in the range 80 ± 10 MeV; the beam line matching foresees a proper set of the emittance compensation solenoids and the S-band cavity gradients in the velocity bunching scheme, according to the invariant envelope criteria (see 3.2 and 1.2).

The beam dynamics in the injector has been simulated with multi-particles codes Tstep [50] and Astra [51], which take into account the space charge effects, relevant at very low energies, and the thermal emittance, considered to be $\varepsilon_t \simeq 0.91 \pm 0.01$ [mm mrad]/[mm] $\cdot \sigma_r$ [mm rms], as the measured value for an S-band RF gun operating at

Table 3.2: Simulated parameters of the 250 pC electron beam at LE IP and at HE IP for several Working Points (WPs), each corresponding to the user required γ -photon beam energy. Following parameters result from electron beam dynamics studies devoted to optimise the γ -ray source.

γ -source WP [MeV]	E_{e^-} @IP [MeV]	E_{e^-} @Inj Exit [MeV]	$\frac{\Delta\gamma}{\gamma}$ @IP [%c]	σ_z @IP [μm]	ε_n @IP [μm]	β_t @IP [m]	σ_t @IP [μm]
<i>LOW ENERGY LINAC</i>							
0.20	75	70.5	1.15	275	0.51	0.16	23.5
1.00	165	80.5	0.86	274	0.44	0.43	20.0
2.00	234	80.5	0.82	273	0.44	0.43	19.6
2.85	280	80.5	0.78	275	0.45	0.50	19.5
3.50	312	90.5	0.80	278	0.41	0.55	19.3
<i>HIGH ENERGY LINAC</i>							
10.00	530	80.5	0.45	272	0.44	0.71	17.5
13.00	605	80.5	0.43	273	0.44	0.71	17.5
19.50	740	90.5	0.48	278	0.41	0.95	16.5

$E_{acc} = 120 \text{ MV/m}$ [70].

The bunch distribution at the cathode surface strongly impacts on the optimisation process of final parameters at the injector exit. Several computational studies and measurements developed at the SPARC.LAB photo-injector demonstrated that a laser pulse with a flat-top longitudinal distribution allows to minimise the projected emittance value at the injector exit [71]; even better results can be achieved by a tuning of the flat-top pulse FWHM duration and rise time [72]. The above considerations, together with an extensive simulation campaign reported in [58, Ch. 2], lead to consider a photo-cathode laser pulse with a flat-top longitudinal profile of 8.5 ps FWHM duration, 1.5 rise time and a transverse uniform distribution of rms spot size $\sigma_r = 250 \mu\text{m}$, radius $r = 0.5 \text{ mm}$. The Figure 3.8 shows the shaped charge distribution at cathode surface produced by such laser pulse as obtained with 2D Tstep simulations; the cylindrical symmetry of the beam allows us to adopt a 2D model which requires a reasonable number of particles and mesh points, and so computational time.

Three working points have been optimised, around the reference one, to exit from the photo injector with a beam energy in the range $80 \text{ MeV} \pm 10 \text{ MeV}$, to cover the required energy range for the electron beam while preserving its quality: looking at Table 3.2 each row colour corresponds to a beam energy at the injector exit.

The RF gun accelerating field is $E_{acc} \simeq 120 \text{ MV/m}$ and a slightly dephasing be-

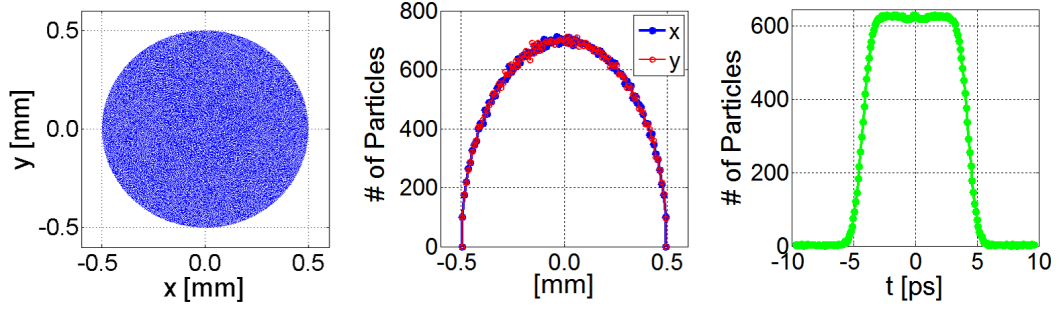


Figure 3.8: Charge distribution at cathode surface produced by the photo-cathode laser pulse as obtained with 2D Tstep simulations. The photo-cathode laser pulse shows a flat-top longitudinal profile of 8.5 ps FWHM duration, 1.5 rise time and a transverse uniform distribution of rms spot size $\sigma_r = 250 \mu m$, radius $r = 0.5$ mm.

Table 3.3: Simulated parameters of the 250 pC electron beam at photo-injector exit for several Working Points (WPs).

E_{e^-} [MeV]	E_{acc} [MV/m]	$\frac{\Delta\gamma}{\gamma}$ [%]	σ_z [μm]	ϵ_n [μm]	β_t [m]	σ_t [μm]
70.5	18.25	1.67	267	0.53	79.1	559
80.5	21.00	1.71	279	0.43	63.0	414
90.5	23.50	1.69	280	0.41	50.5	344
146.0	23.50	1.69	274	0.45	50.5	439

tween the field and the beam allows to maximise the energy gain in this part. Then, the following S-band structures operate in the range $E_{acc} = 17.5 - 23.5$ MV/m to provide the energy tuning in the range 80 ± 10 MeV. It has to be mentioned that for accelerating gradients lower than 20 MV/m, needed to provide a 70 MeV electron beam, the transition energy increases up to 90 MeV; nevertheless only a slightly difference can be observed extending the multi particle simulation to the first cavity of the downstream C-band linac.

The velocity bunching scheme in the first S-band cavity is adopted to shorten the beam length from 740 to 280 μm . Finally, the emittance minimisation is obtained setting the gun solenoid at $\simeq 3$ KG and the one surrounding the first S-band cavity at $\simeq 0.3$ KG. A slightly off-crest operation of the second S-band cavity further reduces the energy spread at the injector exit. In this configuration the design electron beam parameters at the injector exit are: $E = 80.5$ MeV, $\epsilon_n = 0.45$ mm mrad, $\sigma_t = 439 \mu m$, $\Delta\gamma/\gamma = 1.69 \%$, $\sigma_z = 274 \mu m$ (see Figure 3.10).

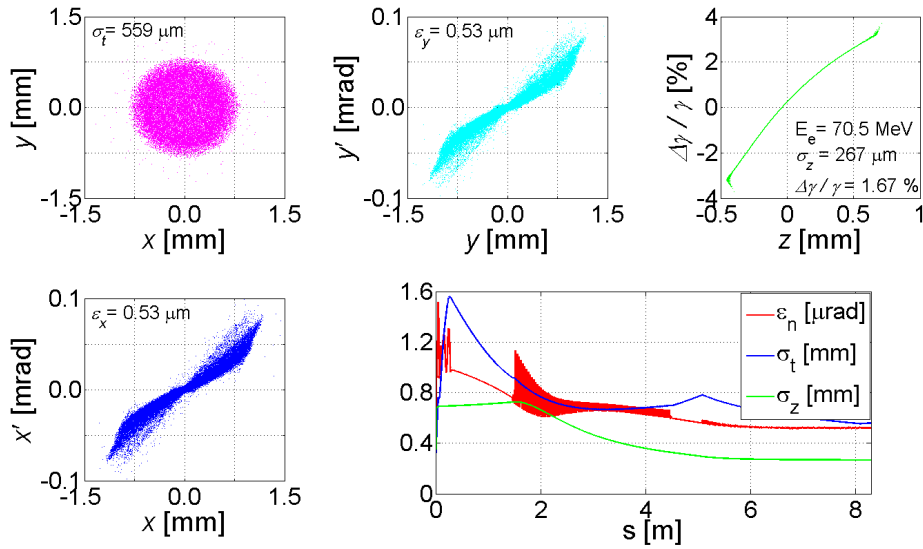


Figure 3.9: Longitudinal and transverse phase spaces at the injector exit and evolution of transverse normalised emittance (ε red line), spot size (σ_t blue line) and longitudinal bunch length (σ_z green line) from the cathode to the injector exit for a 250 pC electron beam with final energy of 70.5 MeV as obtained with the Tstep code.

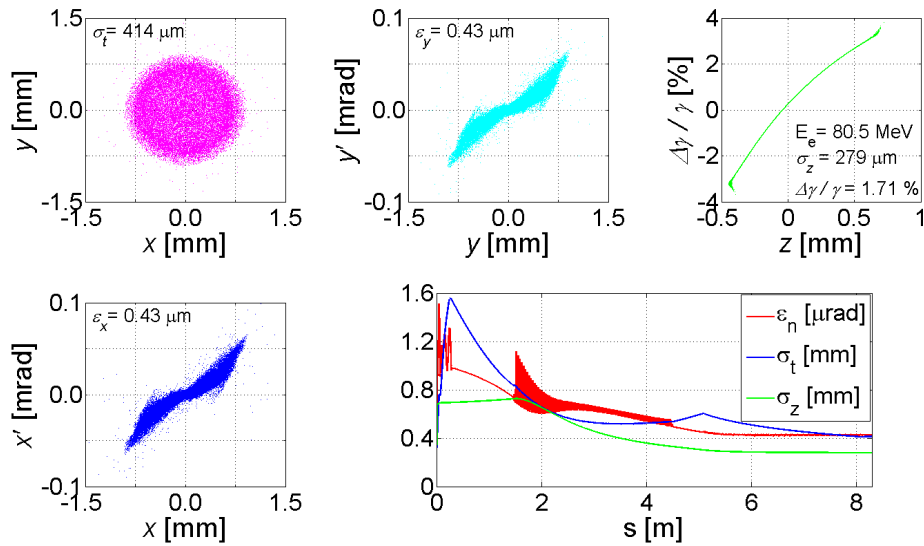


Figure 3.10: Longitudinal and transverse phase spaces at the injector exit and evolution of transverse normalised emittance (ε red line), spot size (σ_t blue line) and longitudinal bunch length (σ_z green line) from the cathode to the injector exit for a 250 pC electron beam with final energy of 80.5 MeV as obtained with the Tstep code.

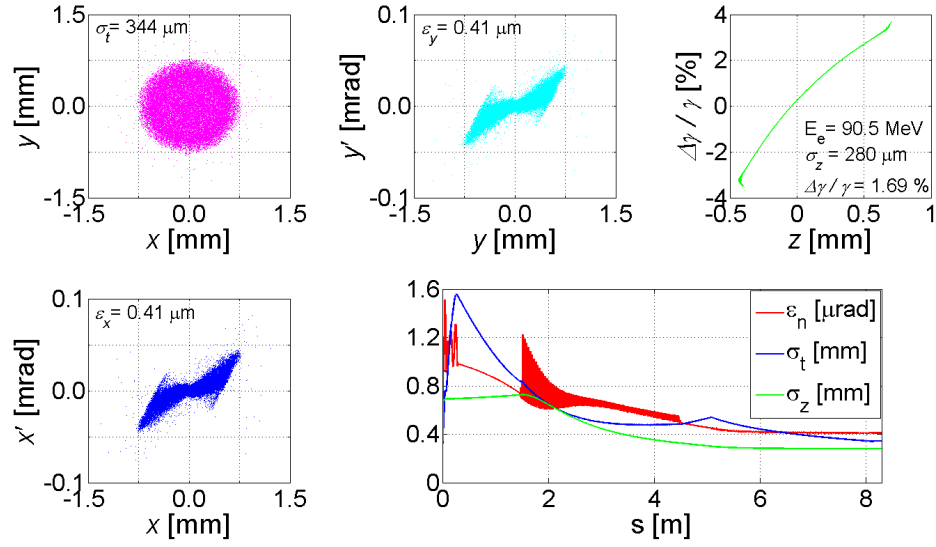


Figure 3.11: Longitudinal and transverse phase spaces at the injector exit and evolution of transverse normalised emittance (ε red line), spot size (σ_t blue line) and longitudinal bunch length (σ_z green line) from the cathode to the injector exit for a 250 pC electron beam with final energy of 90.5 MeV as obtained with the Tstep code.

The simulation results are shown in Figure 3.9 - Figure 3.11 for a 250 pC electron beam with final energy of 70.5, 80.5 and 90.5 MeV; the plots show the longitudinal and transverse phase spaces at the injector exit and evolution of the transverse normalised emittance (ε red line), spot size (σ_t blue dash-dot line) and longitudinal bunch length (σ_z green dashed line) from the cathode to the injector exit as obtained with the Tstep code.

The on-crest operation has been also explored resulting in a maximum 146 MeV electron beam at the injector exit. Here the gun solenoid is set at $\simeq 3.2$ KG while the one surrounding the first S-band cavity set at $\simeq 0.4$ KG.

The beam parameters obtained with the simulations are listed in Table 3.3 for all the examined working points.

The C-band Booster Linac

The C-band linac optimisation aims to provide the electron beam, coming from the injector, at IP with: $\varepsilon_n \simeq 0.45$ mm mrad, $\Delta\gamma/\gamma \leq 0.1\%$ and tunable energy in the range 75 – 740 MeV; more detail in the beam line matching foresees to properly set magnetic elements and accelerating cavities, including wake fields in the C-band sections and the

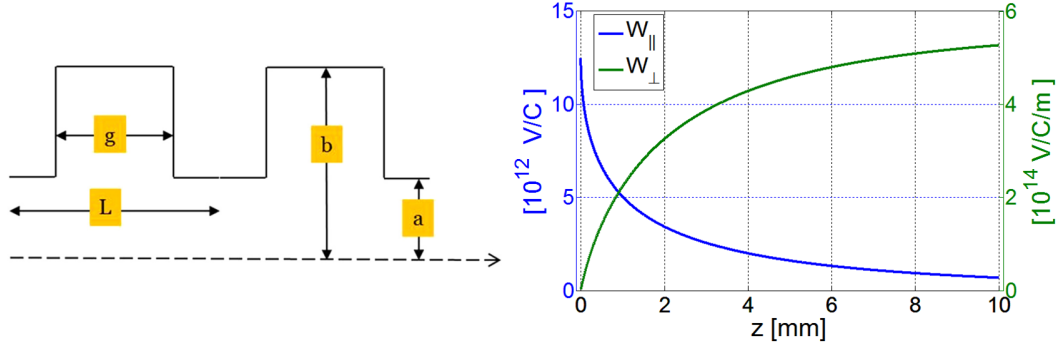


Figure 3.12: Right: Pill box cavity model considered for the wake fields calculations. Left: Longitudinal and transverse short-range wake function curves integrated over one cell for the C-band accelerating structure.

coherent and incoherent synchrotron radiation effects in the bending magnets.

Electron beam dynamics simulations in the C-band booster linac have been performed with the Elegant code [52] that includes the wakefields generated by the electron beam inside the accelerating structures together with the longitudinal space charge and the coherent and incoherent synchrotron radiation effects in the bending magnets. The code computes wake fields making the convolution of the specified time-dependent moment of the particle distribution with the Green wake function, defined as the time response of a system to a unit impulse. The longitudinal wake function is expressed in *Volt/Coulomb*, while the transverse wake function as *Volt/(Coulomb meter)* in order to be independent of the offset of the driving charge.

For the C-band structures the asymptotic values of the longitudinal and transverse wake fields have been calculated according to [73, 74]

$$W_{0\parallel}(s) \approx \frac{Z_0 c}{\pi a^2} \exp\left(-\sqrt{\frac{s}{s_1}}\right) \frac{V}{Cm} \quad \text{with} \quad s_1 = 0.41 \frac{a^{1.8} g^{1.6}}{L^{2.4}} \quad (3.6)$$

$$W_{0\perp}(s) \approx \frac{4Z_0 c s_2}{\pi a^4} \left[1 - \left(1 + \sqrt{\frac{s}{s_2}}\right) \exp\left(-\sqrt{\frac{s}{s_2}}\right)\right] \frac{V}{Cm^2} \quad \text{with} \quad s_2 = 0.17 \frac{a^{1.79} g^{0.38}}{L^{1.17}} \quad (3.7)$$

where Z_0 is the free space impedance, c is the light velocity and a , L , b and g are defined as in Figure 3.12. The calculated Green function wakes used in Elegant for the C-band accelerating structures are reported in Figure 3.12.

Several Working Points have been optimised to provide at LE-IP an electron beam energy in the range 75 - 312 MeV and at HE-IP a beam energy in the range 530 -740 MeV, and the resulting parameters are listed in Table 3.2. An additional working point, not reported in Table 3.2, has also been studied for the highest electron beam energy of 740 MeV at HE-IP, relaxing the performances of the RF machine power system; an uncompressed electron beam with 146 MeV energy is generated in the photo-injector and then tracked-up to the HE-IP with final $\Delta\gamma/\gamma$ of at least 2 ‰, out of specifications even if still acceptable by the user community.

The row colours in Table 3.2 are related to the electron beam energy at the photo-injector exit needed to guarantee the required beam quality at the IPs. Low and the high energy line have been matched to provide the design electron beam parameters as follows

@LE-IP: $\varepsilon_n \simeq 0.45$ mm mrad, $\sigma_t \simeq 19.5$ μm , $\Delta\gamma/\gamma = 0.80$ ‰, $\sigma_z \simeq 270$ μm .

@HE-IP: $\varepsilon_n \simeq 0.45$ mm mrad, $\sigma_t \simeq 17.0$ μm , $\Delta\gamma/\gamma = 0.45$ ‰, $\sigma_z \simeq 270$ μm .

Accelerating gradients set in the range of 10 – 33 MV/m, complying with the ELI-NP RF power distribution system, together with the proper off crest operation, i.e. dephasing of ± 15 degrees with respect to the maximum RF accelerating field, allow to reach energy spread values of 0.8 ‰ at LE IP and of 0.4 ‰ at HE IP. The beam transport line optics is matched to close the horizontal dispersion at each dogleg exit. Furthermore, the final focusing system provides a spot size tunable in the range 18 – 25 μm at the LE IP and in the range 10 – 25 μm at the HE IP.

Reference working points for the C-band linac are the 234 MeV electron beam at LE-IP and the 530 MeV electron beam at HE-IP, respectively the 2.0 MeV and 10.0 MeV γ source energy. The simulation results are shown in Fig.3.14 for the 234 MeV electron beam required at the LE IP for the 2 MeV γ photon beam production. The accelerating gradient is set at 23 MV/m with the following dephasing: $+15^\circ$ on the first two accelerating structures and -3° for the third and the fourth ones. The resulting electron beam parameters at the LE IP are: $E = 234$ MeV, $\varepsilon_n = 0.44$ mm mrad, $\sigma_t = 19.6$ μm , $\Delta E/E = 0.82$ ‰, $\sigma_z = 273$ μm . The simulation results are shown in Fig.3.16 for the 530 MeV electron beam required at the HE IP for the 10 MeV γ photon beam production. The accelerating gradient is set at 22 MV/m with the following dephasing: $+20^\circ$ on the first four accelerating structures and -3° for the following ones. The resulting electron beam parameters at the HE IP are: $E = 530$ MeV, $\varepsilon_n = 0.44$ mm mrad, $\sigma_t = 17.5$ μm , $\Delta E/E = 0.45$ ‰, $\sigma_z = 272$ μm .

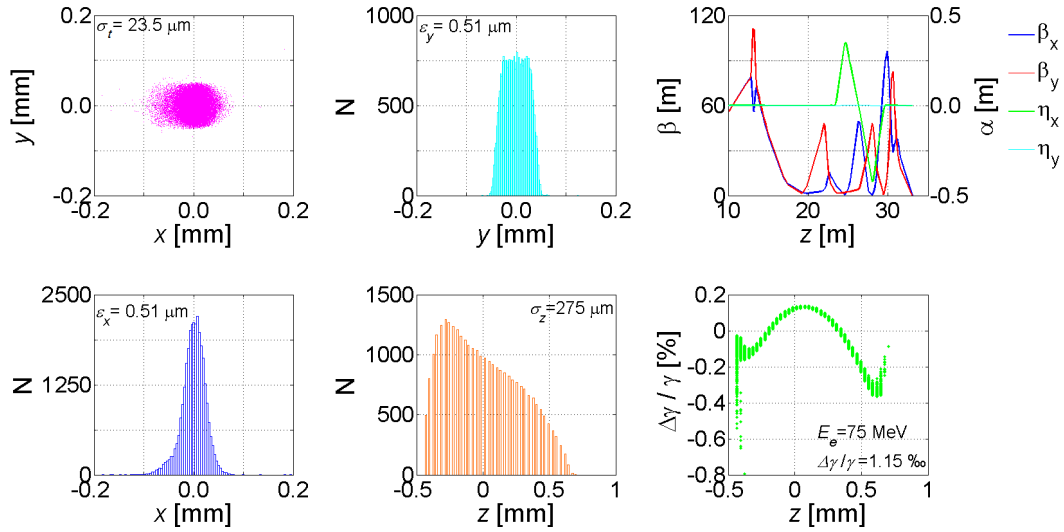


Figure 3.13: Transverse and longitudinal phase space at LE-IP for the 75 MeV electron beam as obtained by Elegant simulations and the Twiss parameters of the electron beam lines from the photo-injector exit down to the LE-IP.

The simulation results are shown in Figure 3.13 - Figure 3.15 for the lowest, nominal and higher energy working points of the low energy line and in Figure 3.16 - Figure 3.17 for the nominal - that is also the lowest - and higher energy working points of the high energy line; the plots show the longitudinal and transverse phase spaces at IPs and the Twiss parameters of the electron beam lines from the photo-injector exit down to the LE-IP and HE-IP respectively.

Wakefield Effects in Single and Multi-bunch Operation

When an intense electron beam passes through a wall discontinuity, as RF accelerating structures, it gives rise to electromagnetic fields which can affect its own beam dynamics. If the beam velocity is almost that of light, from the causality principle, fields can only stay behind the leading charge and only trailing charge dynamics, in both longitudinal and transverse plane, will be perturbed in the sense of changing in momentum. Longitudinal wake fields, where the forces are parallel to the beam axis, affect the energy profile of the beam; transverse wake fields, where the forces are perpendicular to the beam axis, can deflect the beam further away from the axis in case of off-axis beam trajectories. Results can be the bunch emittance growth and large transverse trajectory errors [75].

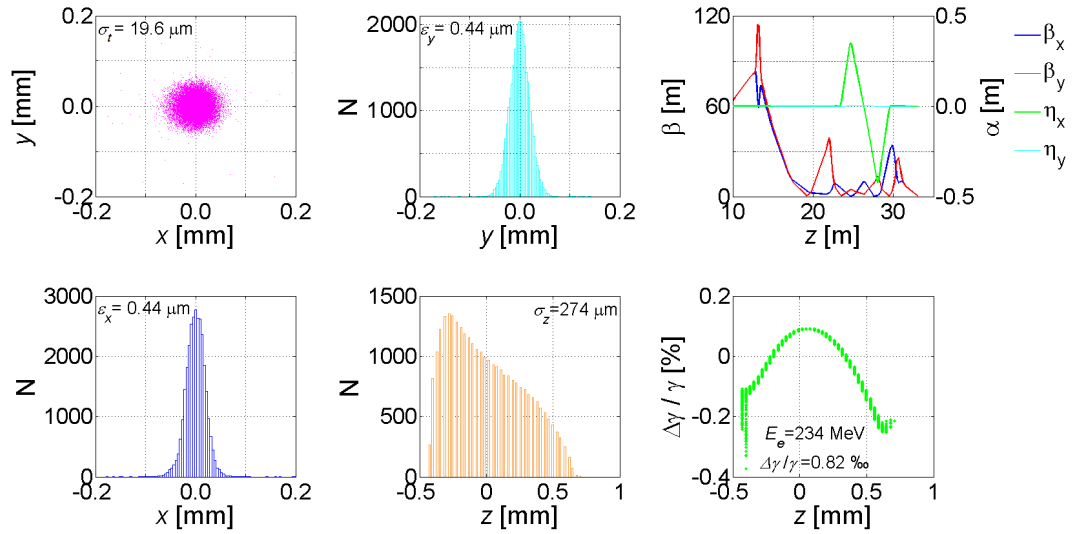


Figure 3.14: Transverse and longitudinal phase space at LE-IP for the 234 MeV electron beam as obtained by Elegant simulations and the Twiss parameters of the electron beam lines from the photo-injector exit down to the LE-IP.

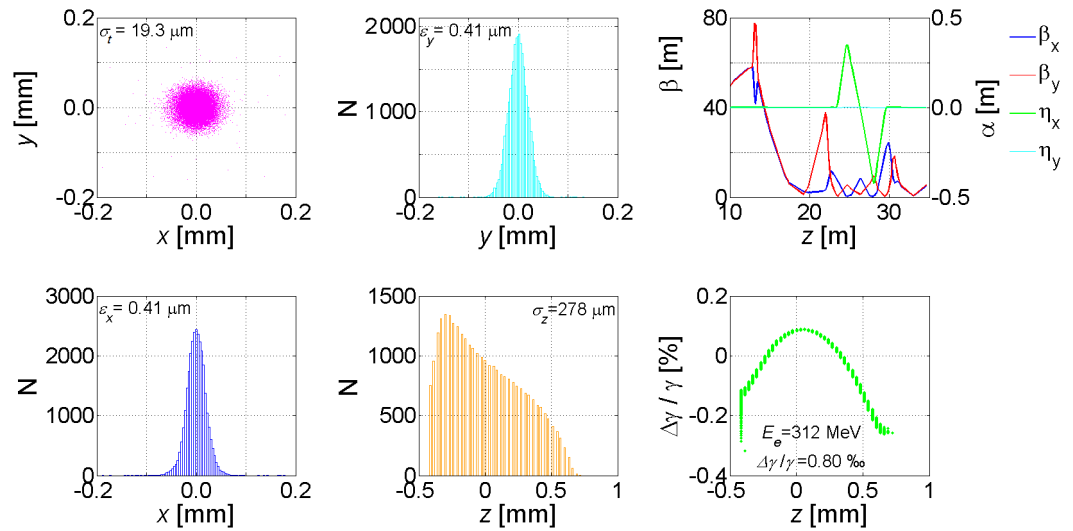


Figure 3.15: Transverse and longitudinal phase space at LE-IP for the 312 MeV electron beam as obtained by Elegant simulations and the Twiss parameters of the electron beam lines from the photo-injector exit down to the LE-IP.

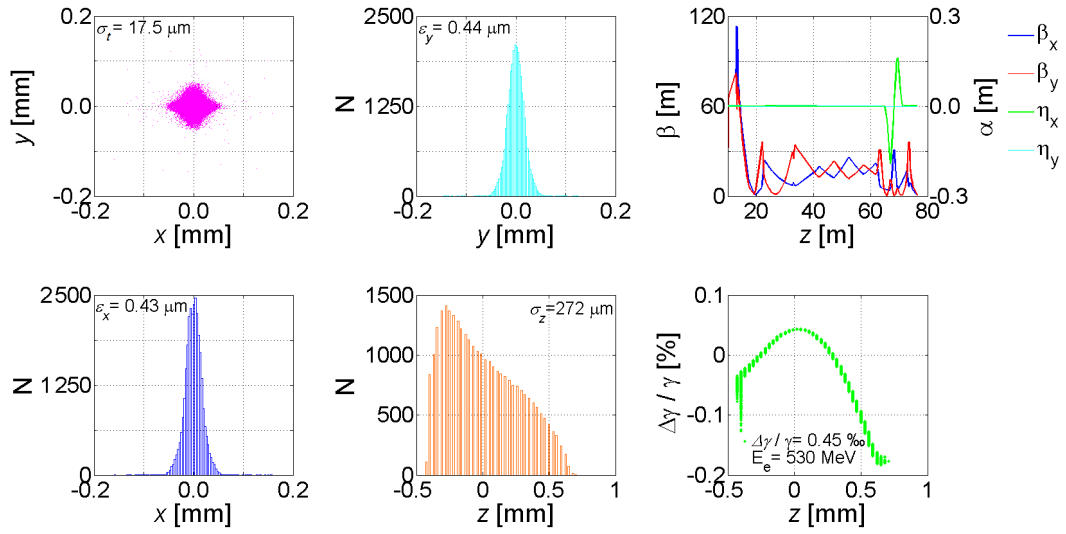


Figure 3.16: Transverse and longitudinal phase space at HE-IP for the 530 MeV electron beam as obtained by Elegant simulations and the Twiss parameters of the electron beam lines from the photo-injector exit down to the HE-IP.

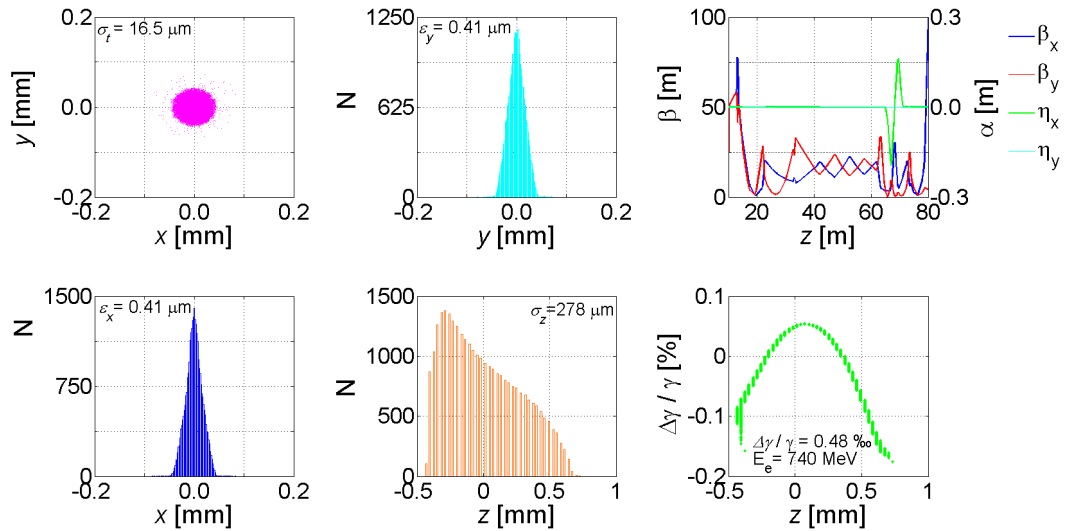


Figure 3.17: Transverse and longitudinal phase space at HE-IP for the 740 MeV electron beam as obtained by Elegant simulations and the Twiss parameters of the electron beam lines from the photo-injector exit down to the HE-IP.

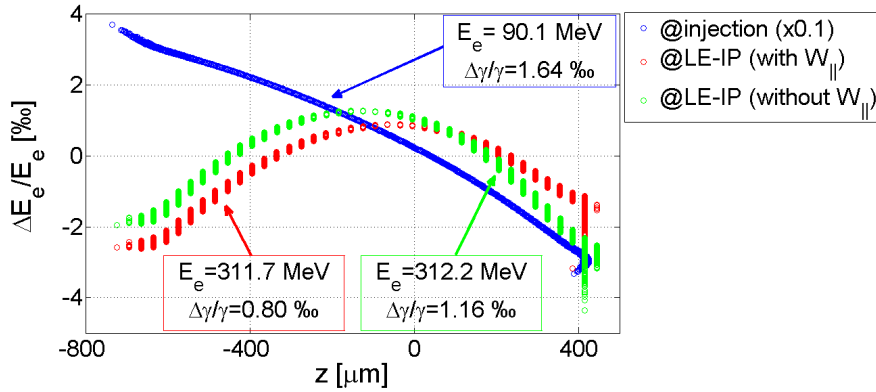


Figure 3.18: Beam energy profile at the C-band linac injection (blue curve) and at LE-IP as obtained by including (red curve) and not including (green curve) the longitudinal wakefields: the beam loses $\sim 0.2\%$ of its energy due to the longitudinal wakefields.

Those fields are called short-range wakefields where they vanish in few bunch lengths [76], otherwise they are called long-range wakefields and can lead to instabilities in case of multi-bunch operation. In the following beam dynamics studies regarding the beam quality sensitivity to wakefields effects in the C-band linac are presented in both single and multi-bunch operation.

Single-bunch Operation

The 250 pC electron beam, represented by 50k macro-particles generated with the Astra code, comes up to the C-band linac entrance with the following parameters: $E = 80.5$ MeV, $\varepsilon_n = 0.44$ mm mrad, $\sigma_t = 401$ μm , $\Delta\gamma/\gamma = 1.69$ ‰, $\sigma_z = 274$ μm . Then the beam is tracked through the C-band low energy linac with the Elegant code and short-range longitudinal and transverse wakefields effects have been considered separately.

Longitudinal wakefields effects The study is in terms of the energy profile variation in case of on-axis trajectory, so that the effect of transverse wake fields can be neglected; longitudinal wakefields inside the C-band cavities have been calculated as described in 3.4. The Figure 3.18 shows the beam energy profile at the C-band linac injection (blue curve) and at LE-IP as obtained by including (red curve) and not (green curve) the longitudinal wakefields: the beam loses $\sim 0.2\%$ of its energy due to the longitudinal wakefields.

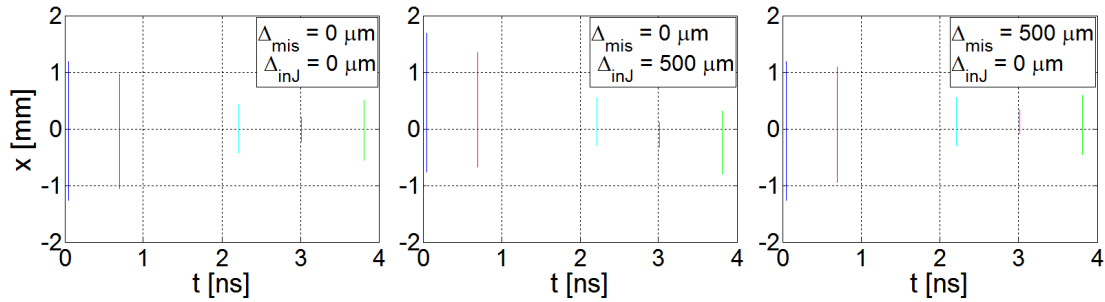


Figure 3.19: Evolution of the electron beam horizontal distribution along the C-band linac in ideal conditions (left) and in case of $\Delta_{inj} = 500 \mu m$ (centre) or $\Delta_{mis} = 500 \mu m$ (right).

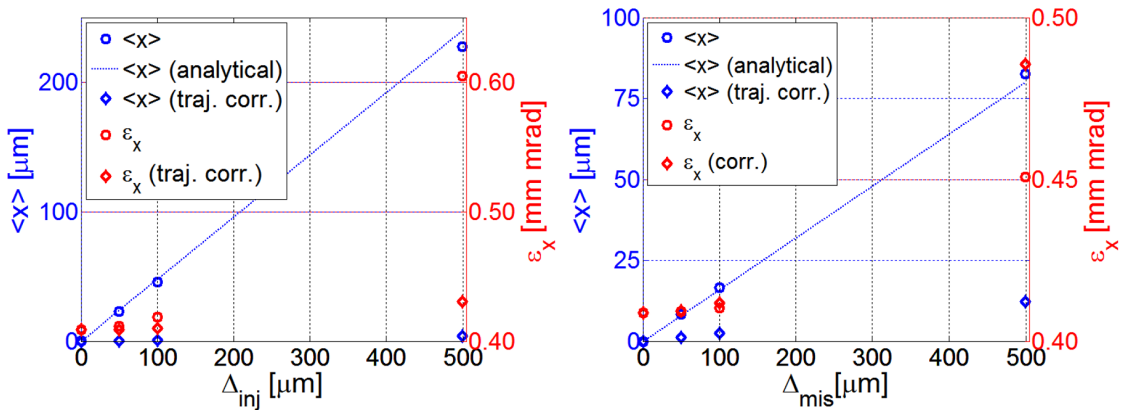


Figure 3.20: Behaviour of the simulated horizontal centroid (blue markers) - $\langle x \rangle$ - and normalised emittance (red markers) - ϵ_x - as function of Δ_{inj} (left) and Δ_{mis} (right) with (diamonds) and without trajectory correction (rounds). The behaviour of $\langle x \rangle$ (blue rounded markers) as function of Δ_{inj} (left) and Δ_{mis} (right), confirms the expected linear dependence on Δ_i (blue dashed lines) analytically calculated as described in [75, Ch. 2] (with $i=[inj,mis]$).

Transversal wakefields effects The study is in terms of beam quality and trajectory errors in case of injection offsets at the linac entrance (Δ_{inj}) or cavity misalignments (Δ_{mis}), that both cause the arising of transverse wakefields inside the C-band cavities; the latter have been calculated as described in 3.4. In both cases the head of the bunch excites transverse wakefields that affect the tail motion. The mechanism is similar, but not the same: if injection offsets occur, then the leading particle travels unperturbed along the linac undergoing free betatron oscillations of amplitude Δ_{inj} ; differently, if cavity misalignments occur, then the leading particle travels straight on, without undergoing betatron oscillations. The Figure 3.19 shows the evolution of the beam horizontal distribution along the C-band linac in nominal conditions (left) and in case of $\Delta_{inj} = 500 \mu m$ (centre) or $\Delta_{mis} = 500 \mu m$ (right).

The single bunch transverse motion in case of injection offsets at the linac entrance or cavity misalignments is detailed described in [77] that also reports very useful analytical formulas to evaluate the expected centroid displacement and emittance growth (more details in Appendix A).

For $\Delta_{inj} \neq 0$ the centroid displacement has been analytically calculated from the equation of motion of the head and tail particles (in the assumption that the beam consists of two macroparticles, each of charge $Q/2$ separated by $\Delta z = 2\sigma_z$). The horizontal motion equation of the head particle is

$$x_1(s) = \Delta_{inj} \cos(ks) \quad (3.8)$$

where s is the longitudinal position along the accelerator and k is the betatron wave number for the head particle ($k = 1/\beta$). Assuming that both particles have the same betatron number k , the horizontal motion equation of the tail particle is

$$x_2 = x_1 + \frac{QW_{0\perp}(2\sigma_z)}{4kE(s)} \Delta_{inj} s \sin(ks) \quad (3.9)$$

where $W_{0\perp}(2\sigma_z)$ is the transverse wakefield at the the distance $\Delta z = 2\sigma_z$ and $E(s)$ the electron beam energy at s .

For $\Delta_{mis} \neq 0$ the equation of motion of the beam centroid is [77]

$$x(s) = -\frac{QW_{0\perp}(2\sigma_z)}{2E_0} \sqrt{\frac{\beta(s)}{\gamma(s)}} \left(\sum_{j=1}^{N_s} \sqrt{\frac{\beta_j}{\gamma_j}} \sin(\Psi(s) - \Psi_j) \right) \Delta_{mis} L \quad (3.10)$$

where $\beta(s)$ and $\gamma(s)$ are the beta function and the Lorentz factor of the electron beam at s , L is the length of the accelerating cavity j and $(\Psi(s) - \Psi_j)$ is the phase advance from the centre of the structure j to the position s .

The beam centroid motion has been computed in the C-band linac structures in case of $\Delta_{inj} \neq 0$ or $\Delta_{mis} \neq 0$ following (3.8) - (3.10); beam dynamics simulations in the C-band linac in case of on-axis motion give nominal values of β and γ along the machine. In Figure 3.20 are reported the beam centroids at the exit of the 4th C-band accelerating cavity as obtained by analytical calculation and simulations.

As illustrated in Figure 3.20, the behaviour of the simulated horizontal centroid (blue rounded markers) - $\langle x \rangle$ - as function of Δ_{inj} (left) and Δ_{mis} (right), confirms the expected linear dependence on Δ_i (blue dashed lines) analytically calculated as described in [75, Ch. 2] (with $i=[inj,mis]$) and here reported in (3.8) - (3.10).

The trajectory correction can help to prevent emittance growth and centroid displacements due to transverse wakefields [78, 79]; the Figure 3.20 also shows the behaviour of $\langle x \rangle$ (blue markers) and ϵ_x (red markers) as function of Δ_i with (diamonds) and without (rounds) the trajectory correction. Simulation results highlight that the trajectory correction is much more effective in case of $\Delta_{inj} \neq 0 \mu m$ than in case of $\Delta_{mis} \neq 0 \mu m$ and so, as it will be explained in details in 3.5, $\Delta_{mis} < 100 \mu m$, and even less, are strongly suggested.

Multi-bunch Operation

The multi-bunch operation at the ELI-NP GBS foresees the collision of a train of 32 electron bunches, separated by almost 16 ns, with a high intensity recirculated laser pulse and allows to increase the gamma flux. In such multi-bunch configuration long-range wake fields, excited when the beams pass through the C-band linac cavities, can strongly affect the beam dynamics of the bunches trailing the first one. Longitudinal wake fields, related to the excitation of the fundamental accelerating mode and referred to as beam loading effects, can produce a cumulative energy deviation from the first to the last bunch, while transverse wake fields can drive to the multi-bunch beam break up in case off-axis trajectories occur. The analysis, detailed reported in [80], has been done in terms of variation of the bunch energy along the train in the case of on-axis electron beam motion so that the effects of transverse long-range wake fields can be neglected. In detail, as reported in the Introduction of [58], the electron beam energy variation along the train is required to be lower than 1.0 ‰ with a relative energy spread lower than 1.0 ‰. The electron beam dynamics of each bunch of the train has been simulated with the Elegant code superimposing the long-range wakefields to the short-range wakefields in each cell of the C-band linac accelerating structures. The longitudinal wakefields propa-

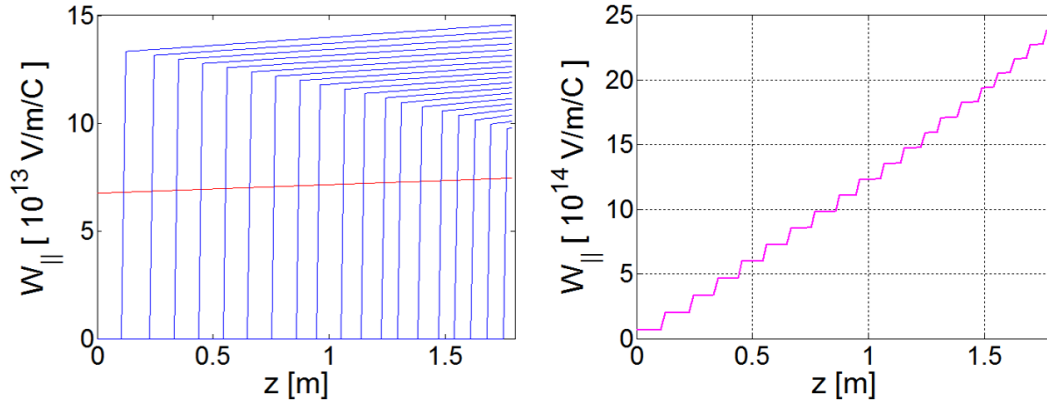


Figure 3.21: Left: Wake potential inside a C-band cavity observed at different instances t_n corresponding to the n^{th} bunch arrive ($n=0,1, \dots, 20$). Right: Total longitudinal wake potential in full beam loading condition, i.e. in the steady state.

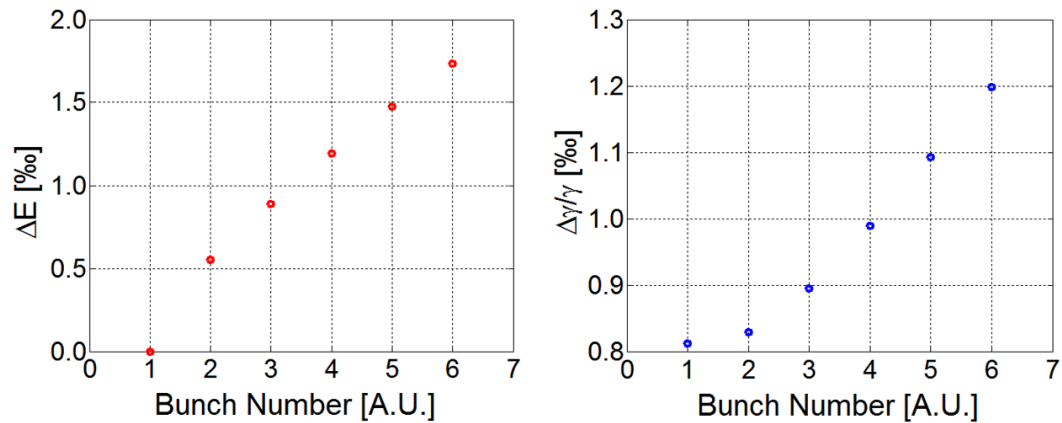


Figure 3.22: Left: Cumulative energy deviation in the multi-bunch operation from the first to the last bunch due to longitudinal long-range wake fields. Right: Relative energy spread in the multi-bunch operation from the first to the last bunch due to longitudinal long-range wake fields.

gation inside the C-band accelerating cavities has been accurately calculated at different instances corresponding to the n^{th} bunch arrive ($n=0,1, \dots, 20$) (see Figure 3.21); this calculation and the proposed full beam loading compensation technique, consisting in a modulation of the input power to maintain the required energy variation and energy spread along the train, are described for our case in [81]. Since after the passage of 20 bunches the wake field reaches a steady state, the study regarded the calculation of the beam loading in case of maximum 20 bunches, not expecting observable deviation from the bunch 20^{th} to the last of the train. In Figure 3.22 is plotted the simulated cumulative energy deviation in the multi-bunch operation from the first to the bunch 6^{th} due to the beam loading effect: the energy decreases from the first to the 6^{th} bunch of the train, resulting in a deviation from the first bunch energy of almost 2.0 ‰, reaching values higher than the 1.0 ‰ required in [58]. Also a variation in the relative energy spread along the train is expected due to the beam loading effect; in Figure 3.22 is also plotted the relative energy spread in the multi-bunch operation from the first to the bunch 6^{th} due to the beam loading effect: the relative energy spread increases from the first to the 6^{th} bunch, reaching energy spread values higher than 1.0 ‰ required in [58].

Above considerations enhance the importance of the full beam loading compensation proposed in [81] to avoid the energy modulation along the train so reducing the longitudinal phase space degradation at the collision with the laser pulse. In the next future the study will be extended to the electron beam dynamics in the RF gun and in the two S-band SLAC type TW cavities. Further the transverse long-range wake fields will be treated in order to estimate the multi bunch beam break up effect on the transverse phase space.

Quasi-constant Gradient C-band cavities

The electron beam dynamics in the C-band linac, illustrated for the ELI-NP GBS case in 3.4, has been investigated assuming a constant accelerating field in the twelve TW disk loaded cavities. Actually, as reported in [67], the cavities are fed by a single klystron with a constant RF input pulse and the cavity iris apertures have been shaped to have a quasi-constant accelerating field with $E_{avg} = 33$ MV/m and a 15 ‰ slope; the reason lies in avoiding very small irises at the end of the structure, needed for a perfect constant gradient profile, that lead to the increase of the dipole mode effectiveness, reduction of the pumping speed and beam clearance. Further to achieve an average accelerating field of 33 MV/m in a constant impedance structure the accelerating field

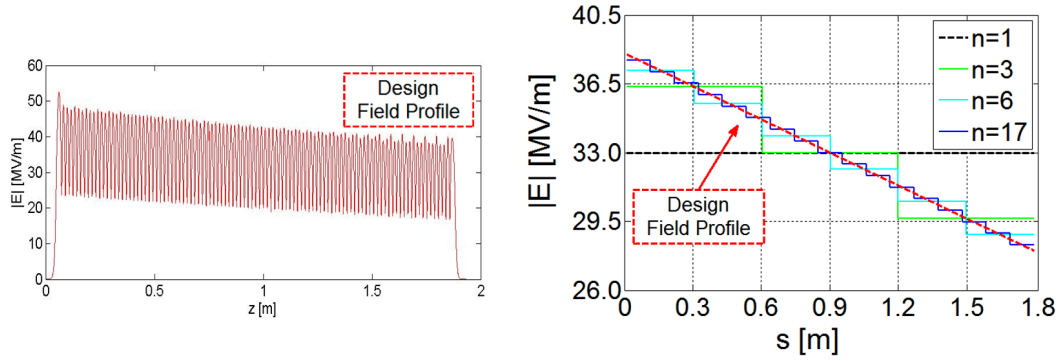


Figure 3.23: Left: accelerating field as obtained by simulations and reported in [67]. Right: Accelerating field as obtained by Elegant simulations (right): the cavity, 1.8 m long and with $2\pi/3$ field phase advance per cell, has been split in n constant profile TW structures (with $n = 1, 3, 6, 17$) to provide a good enough approximation to the design field profile (red dashed line).

in the first cell has to be increased up to more than 43 MV/m, giving potential problems from the breakdown rate point of view. The design field profile, simulated and reported in [67], is illustrated on the left in Figure 3.23: the non-constant field profile leads to a change of the transverse motion in the input and output couplers of the cavities (see Appendix B), that are due to RF focusing, adiabatic damping and RF kick and depend on the accelerating gradient and on the electron energy [130, 26]; so the booster matching robustness should be investigated and eventually newly computed.

The electron beam dynamics in the C-band linac is illustrated considering the quasi-constant accelerating field of the C-band cavities by using the Elegant code, that includes the transverse RF field effects. The code combines pure π -mode standing wave with a travelling wave to accurately simulate the fringe field, at either beginning and end of the cavity, based on the Serafini-Rosensweig model described in [82]: the fringe field at beginning is simulated with a half standing wave cell leading the TW cavity; the fringe field at end is simulated with half standing wave cell trailing the TW cavity. Each cavity, 1.8 m long and with $2\pi/3$ field phase advance per cell, has been split in n constant profile TW structures (with $n = 1, 3, 6, 17$) to provide a good enough approximation to the design gradient profile. The Figure 3.23 shows the design accelerating field on axis [67] (left) and the ones simulated with Elegant for different n (right): higher is n and more precisely can be simulated the mentioned effect at entrance and exit of a cavity, indeed the model accuracy increases from 86.8 % by using $n = 1$ (constant TW structure) to 99.2 % by using $n = 17$.

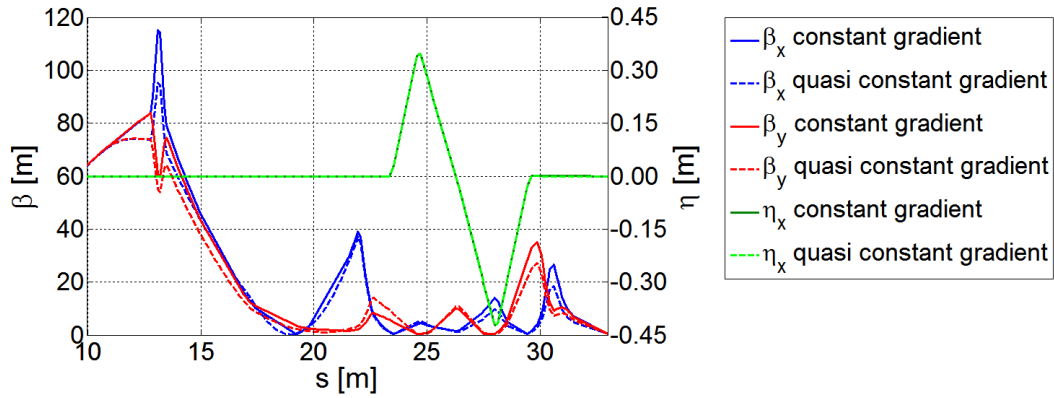


Figure 3.24: Twiss parameters along the linac for the 234 MeV electron beam at LE-IP in case of constant gradient (lines) and quasi constant gradient (dashed lines) C-band accelerating structures.

At the very beginning the beam dynamics is simulated in the first C-band cavity, set at the maximum 33 MV/m accelerating gradient, in order to estimate the effect on the transfer line matching of the quasi constant field profile. The nominal 250 pC electron beam, composed of 30 k macro particles, exits from the photo-injector with a final energy of 80.5 MeV, then is injected in the linac. The quasi constant field profile affects mainly the transverse beam dynamics resulting in a decrease of the spot size at the cavity exit from $\sigma_t = 334 \mu m$ for $n = 1$ to $\sigma_t = 318 \mu m$ for $n = 17$. This behaviour can be explained looking at the focusing strength associated to the transverse RF field in the couplers, that scales as

$$K_r = -\frac{1}{8} \left[\frac{\gamma'}{\gamma} \right]^2 \quad (3.11)$$

where γ' is the gradient in the particle energy over a period of the cavity (for details see Appendix B).

A proper matching of the quadrupoles along the linac can help to prevent this effect and to provide the nominal beam parameters at LE-IP.

On the above considerations a final beam dynamics study has been performed for the reference 2.0 MeV source working point. The 250 pC electron beam has been tracked up to the LE IP with a final energy of 234 MeV in case of quasi-constant gradient TW cavities for $n = 17$. The beam line has been newly matched by acting on the strength of the first four quadrupoles. The resulting beam parameters at LE-IP are listed in Table 3.4 and the Twiss parameters along the C-band linac are reported in Figure 3.24.

Table 3.4: Simulated parameters for the 234 MeV electron beam at LE-IP in case of constant gradient and quasi-constant gradient TW accelerating cavities.

234 MeV @LE-IP	Constant Gradient TW	Quasi Constant Gradient TW	
Energy	234.0	234.0	MeV
Energy Spread	0.82	0.82	%
Bunch Length	273.0	274	μm
ϵ_n	0.44	0.43	mm mrad
σ_t	19.6	20.5	μm

3.5 Machine Sensitivity Studies

The introduction of errors in the ELI-NP GBS electron beam lines affects the electron beam quality at the IP resulting in emittance and energy spread growth and large transverse trajectory errors [75]. Intense machine sensitivity studies have been performed in order to provide the basis for the alignment procedure and jitter tolerances [83]. In order to ensure a reliable routine operation of the γ -photon source, starting from the accelerator main systems specifications in [58] and taking advantage of the experience acquired at SPARC_LAB Thomson source [84, 85], the maximum reasonable error values have been considered to face the most realistic situation, see Table 3.5, trying not to count only on the best performance of the machine systems and to check the actual robustness of the source design.

The following results are related to the 250 pC electron beam, composed of 30 k macroparticles, tracked up to the LE IP with a final energy of 280 MeV. Injector sensitivity studies have been carried out using Giotto [86] and Astra codes to provide tolerances and specifications for cathode laser system, power supplies and solenoids. Each bunch generated in the injector, has been tracked up to the LE IP along the C-band RF linac, whose sensitivity studies have been carried out using the Elegant code to provide tolerances and specifications for power supplies, magnetic elements and BPMs resolution. At first, the beam transport line is matched to obtain the desired electron beam parameters at the LE IP: $\epsilon_n = 0.45$ mm mrad, $\sigma_t = 20$ μm , $\Delta\gamma/\gamma/E = 0.81$ %, $\sigma_z = 280$ μm , then misalignments and jitter are introduced both in the injector and in the booster to perform the tracking.

Machine sensitivity studies have been performed on samples of 100 machine runs each one obtained generating for each machine a tracking code input in which the ele-

Table 3.5: Maximum error values for power supplies, magnetic elements and beam position monitors resolution.

Photo-Injector		
GUN		
RF Voltage [ΔV]	± 0.2	%
RF Phase [$\Delta\Phi$]	± 0.2	deg
S-band Accelerating Sections		
RF Voltage [ΔV]	± 0.2	%
RF Phase [$\Delta\Phi$]	± 0.2	deg
Alignment on transverse plane [Δxy]	± 70	μm
Solenoids on GUN & TW cavities		
Alignment on transverse plane [Δxy]	± 70	μm
Cathode Laser System		
Arrival time [Δt]	± 200	fs
Pointing Instabilities [Δs]	± 20	μm
Energy Fluctuation	± 5	%
C-band RF linac		
Modules		
Alignment on transverse plane [Δxy]	± 300	μm
Tilt about incoming long. axis [$\Delta\theta$]	± 150	μrad
C-band Accelerating Sections		
RF Voltage [ΔV]	± 0.2	%
RF Phase [$\Delta\Phi$]	± 1	deg
Alignment on transverse plane [Δxy]	$\pm 70, \pm 100$	μm
Quadrupoles		
Geometric strength [Δk]	± 0.3	%
Alignment on transverse plane [Δxy]	$\pm 70, \pm 100$	μm
Tilt about incoming long. axis [$\Delta\theta$]	± 1	mrad
Dipoles		
Bend angle [ΔB]	± 0.1	%
Tilt about incoming long. axis [$\Delta\theta$]	± 1	mrad
Steerers		
Strength [Δk_s]	± 0.2	μrad
Beam position monitors		
Resolution [r]	± 10	μm
Cavity Beam position monitors		
Resolution [r]	± 5	μm

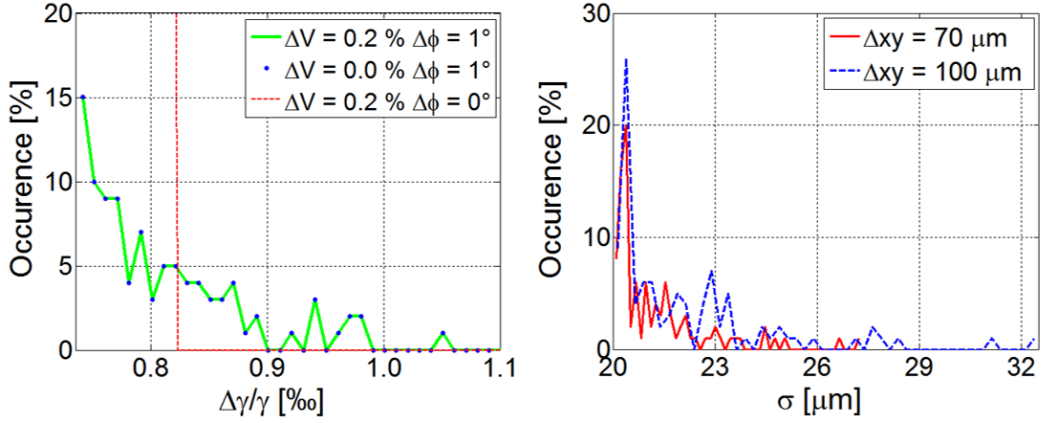


Figure 3.25: Right: Energy spread ($\Delta\gamma/\gamma$) occurrence over 100 machine runs at LE IP in case of: RF voltage jitter (red dashed line), RF phase jitter (blue dots), RF phase and voltage jitter (green line). The analysis suggests that the energy spread can grow up to 0.1% if RF phase jitter in the range $\pm 1^\circ$ arises. Left: Transverse spot size (σ_t) occurrence over 100 machine runs at LE IP for $\Delta xy = \pm 70 \mu\text{m}$ (red line) and $\Delta xy = \pm 100 \mu\text{m}$ (blue dashed line). The analysis suggests that the spot size can grow up to almost 33 μm for $\Delta xy = \pm 100 \mu\text{m}$.

ments errors are provided, in the chosen range, by means of the Matlab Latin Hypercube function that returns an n-by-p matrix, containing a latin hypercube sample of n values (machine run identifier) on each of p variables (element errors). For each column of matrix, the n values are randomly distributed with one from each interval $(0, 1/n)$, $(1/n, 2/n)$, ..., $(1-1/n, 1)$, and they are randomly permuted, furthermore a normal random distribution of minus and plus sign is also applied. In this way the error matrix randomly factorize from -100% to $+100\%$ the considered error values listed in Table 3.5 for each element. With the aim to determine most dangerous error contributions, charge fluctuations in the range 237.5 – 262.5 pC, brought on by cathode laser energy jitter of $\pm 5\%$, and errors in the C-band RF linac are considered one by one according to Table 3.5. The trajectory correction in the booster is not applied at first in order to enhance the emittance dilution and large transverse trajectory errors due to misaligned accelerating structures and quadrupoles and to injection offset [75]. Injector sensitivity studies in case of charge fluctuations result in a maximum deviation from the optimised parameters at injector exit of $\pm 0.05\%$ and do not cause significant linac optics mismatch in case of any other error. The electron beam affected by charge jitter has been injected in the RF linac. Tilt about the incoming longitudinal axis of $\pm 1^\circ$ such as jitter on dipole bending angle of $\Delta B = \pm 0.1\%$ and quadrupole strength of $\Delta k = \pm 0.3\%$ have negligible effects on the

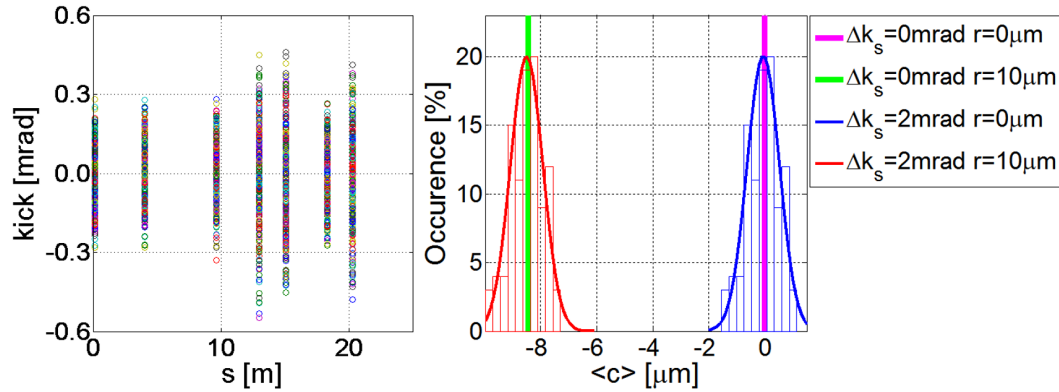


Figure 3.26: Steerer strength needed to centre the electron beam on the BPMs (right) and resulting trajectory errors at LE-IP (left): BPM resolution defines the mean value of trajectory errors $\langle c \rangle$, while steerer strength jitters introduce a standard deviation from the mean value of $\approx \pm 1 \mu\text{m}$.

beam parameters at LE IP and so, are proposed, together with the cathode laser energy jitter, as specifications for the ELI-NP GBS machine. The accelerating structure voltage and phase jitter contributions mainly affect the energy spread of the electron beam. The occurrence of resultant energy spread values over the 100 machine runs is plotted in Figure 3.25 in case of: RF voltage jitter (ΔV red dashed line), RF phase jitter ($\Delta \Phi$ blue dots), RF phase and voltage jitter (green line). The Figure 3.25 shows that the case of RF voltage jitter leads to almost all the machine runs producing an electron beam energy spread of $\approx 0.81 \%$; nevertheless the case of RF phase jitter results in few machine runs producing an electron beam energy spread growth up to $\approx 1.0 \%$. The analysis suggests that energy spread lower than 1.0% needs RF phase jitter lower than $\pm 1^\circ$ in order to ensure a successful routinely operation of the γ -photon source. Misalignments on transverse plane, Δxy , are considered on both accelerating structures and quadrupoles in the range $\pm 70 \mu\text{m}$ or $\pm 100 \mu\text{m}$. While the energy spread remains always lower than 0.88% , the normalized emittance and the spot size grow up to respectively 0.7 mm mrad and almost $33 \mu\text{m}$ for $\Delta xy = \pm 100 \mu\text{m}$. More relaxed is the scenario for $\Delta xy = \pm 70 \mu\text{m}$ where ϵ_n is lower than 0.6 mm mrad and σ_t is lower $27 \mu\text{m}$. The Figure 3.25 also shows the occurrence of resultant σ_t values over the 100 machine runs for $\Delta xy = \pm 70 \mu\text{m}$ (red line) and $\Delta xy = \pm 100 \mu\text{m}$ (blue dashed line). Even if the case of $\Delta xy = \pm 100 \mu\text{m}$ results in few machine runs producing a σ_t higher than $30 \mu\text{m}$, the proposed alignment precision is at least of $\pm 70 \mu\text{m}$.

According to previous study results and to Table 3.5, an enlarged sample of 352 ma-

chine runs is considered introducing also errors in the injector and on the C-band linac module alignment; the latter are treated in the code as beam injection offset, $\Delta xy = \pm 300 \mu m$, and divergence, $\Delta\theta = \pm 150 \mu rad$, at the entrance of each module, including the ones hosting the interaction regions. The 352 machine runs are generated with the same procedure used before, but now misalignments are established in the range $\pm 70 \mu m$. Once more, injector sensitivity studies show negligible effects on the beam parameters at the injector exit not affecting the C-band RF linac matching. At this point the trajectory correction is applied to control the large transverse trajectory errors due to misaligned accelerating structures and quadrupoles, including in the Elegant code the steerer strength jitter and BPM resolution as listed in Table 3.5. Steerers are switched on centering the beam on all BPMs, avoiding off-axis trajectories, and on the two cavity BPMs placed at the entrance and exit of the interaction regions, to maximize the source luminosity. (The alignment errors on steerer magnets and BPMs have not been introduced so far and it will be done next). Figure 3.26 shows the steerer strength needed to centre the electron beam on the BPMs (left side) and the resulting trajectory errors at LE-IP, $\langle c \rangle$ (right side). Looking at the plot on right side, steerer strength always $< 1 mrad$, the maximum value allowed by specifications described in [58], suffices to guarantee beam centroid offsets at IP lower than $10 \mu m$. The plot also shows that BPM resolutions define the mean value of trajectory errors, while steerer strength jitters introduce a standard deviation from the mean value of $\approx \pm 1 \mu m$; a feedback loop that works towards the source luminosity optimisation, not dependent on the BPM resolutions, drives to the best collision alignment through a proper setting of the two steerers before the IP and ensures a reliable routine operation with an electron beam pointing jitter $< 1 \mu m$, as required in [58]. The result of the trajectory correction, that allows to manage injection offset and the spot size growth due to emittance dilution, is an electron beam with $\epsilon_n = (0.45 \pm 0.03) \text{ mm mrad}$, $\sigma_t = (22.5 \pm 1.5) \mu m$ and $\Delta\gamma/\gamma/E = (0.81 \pm 0.05) \%$, confirming the robustness of the source to jitter and misalignments inside the tolerance range listed in Table 3.5.

Finally, beam dynamics studies in case of the random insertion of machine errors listed in Table 3.5 have been performed for the reference working points of the low and high energy line, the 2 MeV and the 10 MeV γ source respectively. A sample of 350 machine runs, generated with the same procedure used before, is considered. The 250 pC electron beam, composed of 30 k macroparticles, has been tracked up to the LE-IP with a final energy of 234 MeV and to the HE-IP with a final energy of 530 MeV, using the electron beamline matching described in 3.4. In Figure 3.27 - Figure 3.29 the

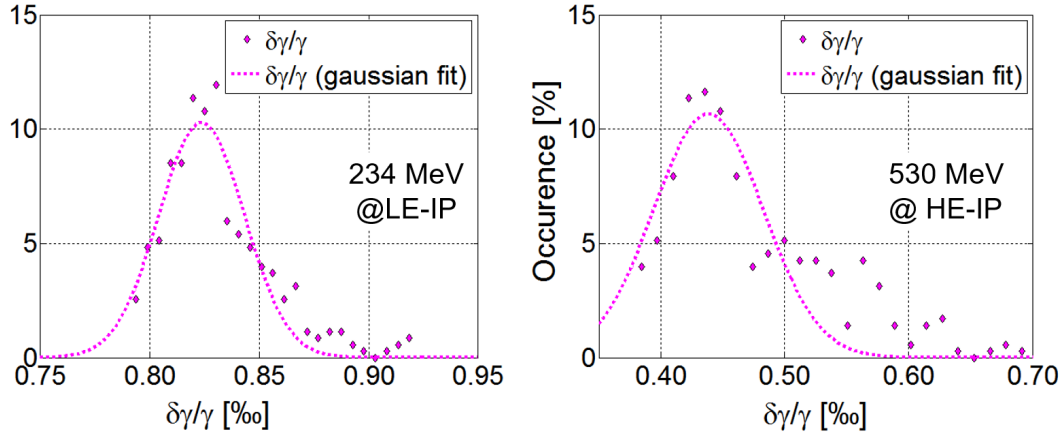


Figure 3.27: Energy spread occurrence over 350 machine runs for the 2.0 MeV (234 MeV electron beam LE-IP) and the 10.0 MeV (530 MeV electron beam HE-IP) γ source WPs in case of $70 \mu\text{m}$ misalignments and jitters on the machine as described in Table 3.5.

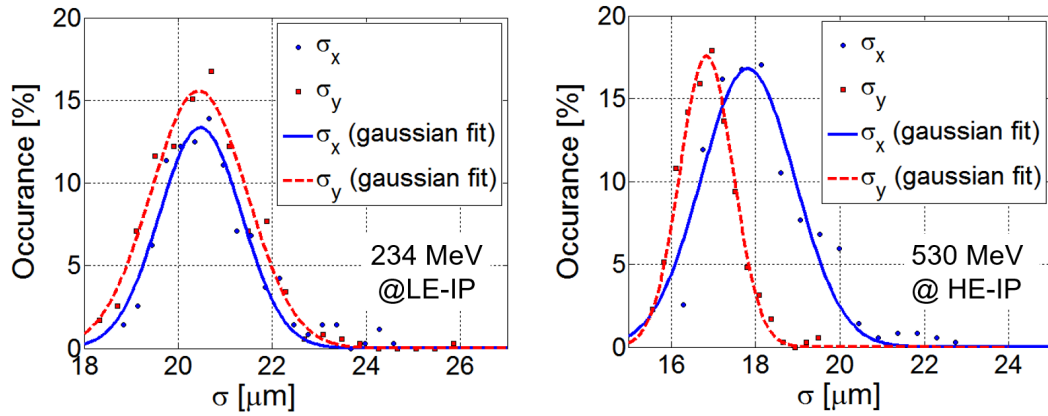


Figure 3.28: Focal spot size occurrence over 350 machine runs for the 2.0 MeV (234 MeV electron beam LE-IP) and the 10.0 MeV (530 MeV electron beam HE-IP) γ source WPs in case of $70 \mu\text{m}$ misalignments and jitters on the machine as described in Table 3.5.

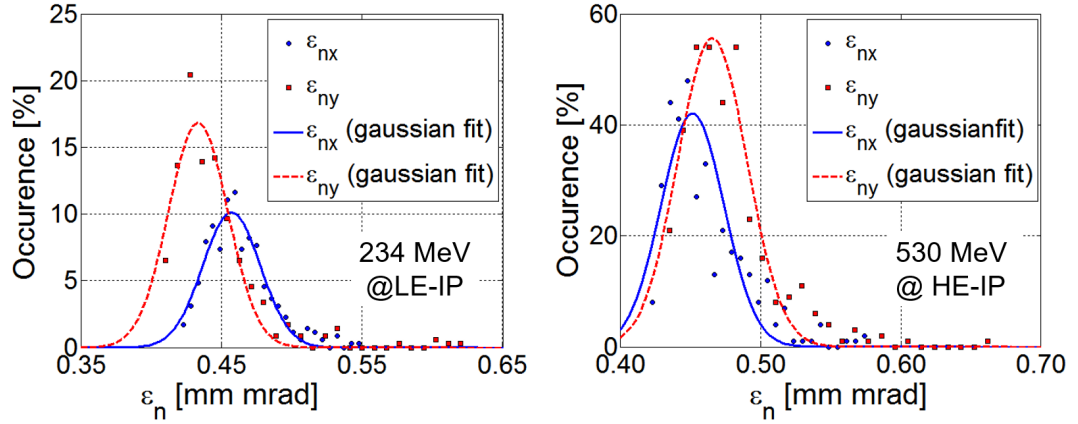


Figure 3.29: Normalised emittance occurrence over 350 machine runs for the 2.0 MeV (234 MeV electron beam LE-IP) and the 10.0 MeV (530 MeV electron beam HE-IP) γ source WP in case of $70 \mu\text{m}$ misalignments and jitters on the machine as described in Table 3.5.

Table 3.6: Simulated parameters for the 234 MeV electron beam at LE-IP in case of any errors and in case of $70 \mu\text{m}$ misalignments and jitters on the machine as described in Table 3.5.

234 MeV @LE-IP	Without errors	With errors	
Energy	234.0	234.0 ± 0.3	MeV
Energy Spread	0.82	0.82 ± 0.02	%
Bunch Length	273.0	274.5 ± 6.0	μm
ϵ_n	0.44	0.46 ± 0.02	mm mrad
σ_t	19.6	20.5 ± 1.0	μm
$\langle x \rangle, \langle y \rangle$	0	0.2 ± 0.5	μm

Table 3.7: Simulated parameters for the 530 MeV electron beam at HE-IP in case of any errors and in case of $70 \mu\text{m}$ misalignments and jitters on the machine as described in Table 3.5.

530 MeV @LE-IP	Without errors	With errors	
Energy	529.6	529.8 ± 0.5	MeV
Energy Spread	0.45	0.44 ± 0.05	%
Bunch Length	272.0	272.1 ± 5.2	μm
ϵ_n	0.44	0.47 ± 0.02	mm mrad
σ_t	17.3	17.8 ± 1.1	μm
$\langle x \rangle, \langle y \rangle$	0	0.1 ± 0.5	μm

obtained results are shown for the 2 MeV and the 10 MeV γ -ray working points, namely the electron beam energy spread, spot size and normalised emittance at IPs, the same data are summarised in Table 3.6 and Table 3.7.

The beam resulting from machine sensitivity study above described have been used to test the out-coming radiation beam dependence on it. The effects on the emitted photons of errors and jitters of both the electron and the laser beams together with the possible collimation system displacements are detailed reported in [69, 87].

3.6 Dark Current Evaluation

Electromagnetic fields in a high gradient RF cavity can result in electron emission from the metallic walls of the cavity itself and induce, in case these electrons are captured and accelerated by the accelerating fields, the so called “dark-current”. This dark current can be accelerated in the linac up to hundreds MeV before they are removed by focusing magnets or by cavity iris apertures. The lost dark current interacts with the materials surrounding cavities and magnets and so produces electromagnetic showers and contributes to the radiation in the linac tunnel; thus simulations on the dark current transport in the ELI-NP GBS linac, from the photo-cathode up to the dumps, have been performed to evaluate in more detail beam losses in the dumpers and to provide the basis for shielding and safety system specifications.

The dark current is mostly generated in the RF gun, due to electrons emitted from the photocathode, and around the irises of the downstream accelerator cavities of the linac. In our simulations the dark current I_{FN} is generated in the Astra code following the Fowler-Nordheim model described in [88]

$$I_{FN} = 1.54 \times 10^{-6} \frac{\beta_e^2 A_e E_{acc}^2}{\varphi} 10^{4.52\varphi - 0.5} e^{-\frac{6.53 \times 10^9 \varphi^{1.5}}{\beta_e E_{acc}}} \quad (3.12)$$

where I_{FN} is the dark current in units of A, β_e the field enhancement factor, φ the work function of the metal in eV (for copper, $\varphi = 4.7$ eV), A_e the effective emission area in m^2 , and E_{acc} the applied electric field in V/m.

Simulations in the ELI-NP GBS injector have been performed with the Astra code and are based on experimental results obtained at LCLS in 2006, where the dark-current transport have been evaluated in the S-band RF gun and in the following S-band SLAC type structure at 120 Hz repetition rate [89, 90, 91]. The dark current measured at the gun exit is up to 3 nC over a 1 μs wide macro pulse (~ 3000 RF buckets) at $E_{acc} =$

120 MV/m, and in a single 3 m long SLAC type structure is about 15 pC over a $2 \mu\text{s}$ wide macro pulse at $E_{acc} = 26 \text{ MV/m}$. It is worth mentioning that the 15 pC charge observed in the S-band structure represents only the 10 % of the charge generated in the cavity itself, being $I_{FN} = 75 \mu\text{A}$ with $\beta_e = 120$, $A_e = 350 \mu\text{m}^2$, and even less than 1 % of the dark current at the gun exit; the charge generated in a S-band cavity decreases even more at lower accelerating gradient and so in our simulations, where $E_{acc} \leq 23.5 \text{ MV/m}$, it will be neglected.

Above considerations lead to a worst case scenario for the dark current transport in the ELI-NP GBS injector where is actually foreseen a $1.5 \mu\text{s}$ RF pulse length at 100 Hz repetition rate. Nevertheless it has been chosen for our simulations [92] a 3 nC dark current, composed of 100 k macro-particles, over $1 \mu\text{s}$ with a uniform cylinder transverse distribution on the cathode with a radius of 2.5 mm, as in [89]. The space charge contribution is switched-off and the machine model is set up with the design optics for the generation of the nominal 250 pC electron beam with a final energy of 80 MeV at the injector exit. Almost 40 % of the 100 k macro-particles are lost in the RF gun and in the drift tube to the first S-band structure. Only 60 % of the 3 nC dark current comes up to the injector exit and so is tracked through the C-band linac matched for the working points illustrated in Table 3.2. The Figure 3.30 shows the transverse and longitudinal phase space of the dark current at the injector exit as obtained by Astra simulations: due to the velocity slippage only few % of the remaining macro particles are transmitted to the nominal 80 MeV working point.

Simulations in the ELI-NP GBS C-band linac have been performed with the Elegant code and are based on experimental measurements carried out at LNF [67], where the C-band cavities have been designed and developed in the framework of the ELI-NP collaboration, devoted to measure the dark current in the C-band cavity mounted at the SPARC_LAB test facility [93] in 2016. The dark current has been measured for different pulse lengths (from 100 to 1600 ns) and field values and it has result to be always lower than $\approx 0.3 \text{ nA}$ [94]; similar results have been obtained at the SwissFEL test facilities at PSI [95] where the C-band test structures have produced no measurable dark current, although electrons were present in the structures. Hence in our simulations the dark current generated in the C-band cavities will be neglected. The wakefield and the CSR effects in the linac are switched off and in this simple model, the macro particles are completely lost when its positions exceeds the aperture limit, i.e. 12 mm for the beam pipe and 7 mm for the TW section irises. The Figure 3.31 and Figure 3.32 show the dark current evolution through the C-band low and high energy linacs, matched for the

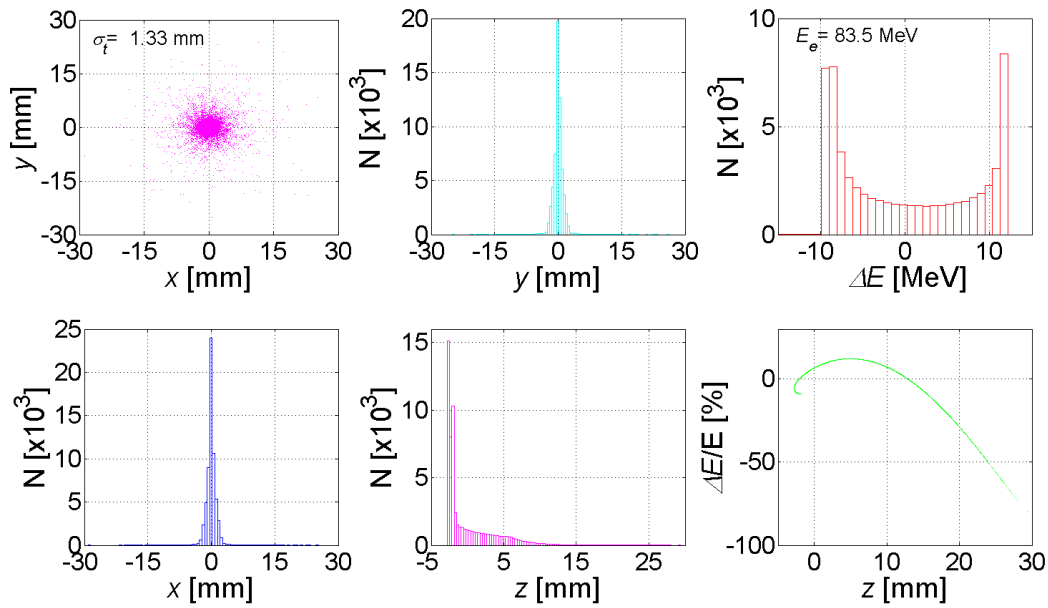


Figure 3.30: Transverse and longitudinal phase space at injector exit for the 3 nC dark current as obtained by Astra simulations. The space charge contribution is switched-off and the machine model is set up with the design optics for the generation of the nominal 250 pC electron beam with a final energy of 80 MeV at the injector exit.

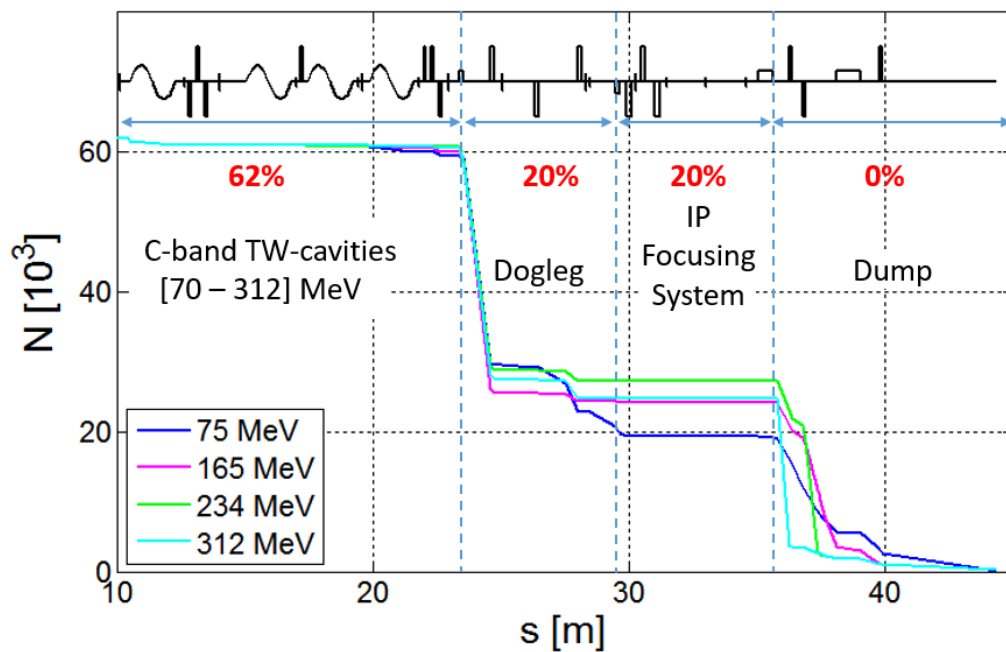


Figure 3.31: Dark current evolution through the C-band low energy linac matched for the working points illustrated in Table 3.2 as obtained by Elegant simulations.

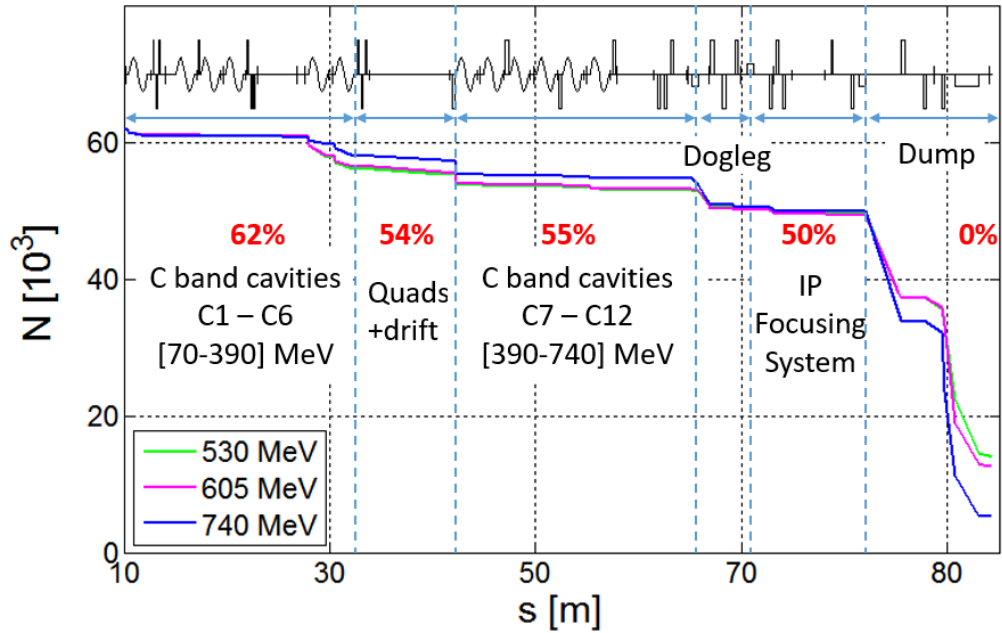


Figure 3.32: Dark current evolution through the C-band high energy linac matched for the working points illustrated in Table 3.2 as obtained by Elegant simulations.

working points illustrated in Table 3.2, as obtained by Elegant simulations: the particles are mainly lost in the two dogleg transfer lines, in the final focusing systems and in the dumps, identifying several hotspots in the linac and driving to precise requirements for shielding and safety system.

The Figure 3.31 and Figure 3.32 show the dark current transverse and longitudinal phase space at IPs as obtained by Elegant simulations in case of the machine model is set up with the design optics for tracking the nominal 250 pC electron beam with a final energy of 234 MeV at LE-IP and 530 MeV at the HE-IP respectively. Looking at Figure 3.33 and Figure 3.34 it has to be mentioned that the dark current propagating through the linac presents a very broad energy spectrum and so it can be captured in several successive RF buckets resulting in a decreasing of the average current lost in the linac; further only few % of the initial dark current reaches the dump region, corresponding to almost a few pC charge that spreads out over a ~ 1 mm long pulse.

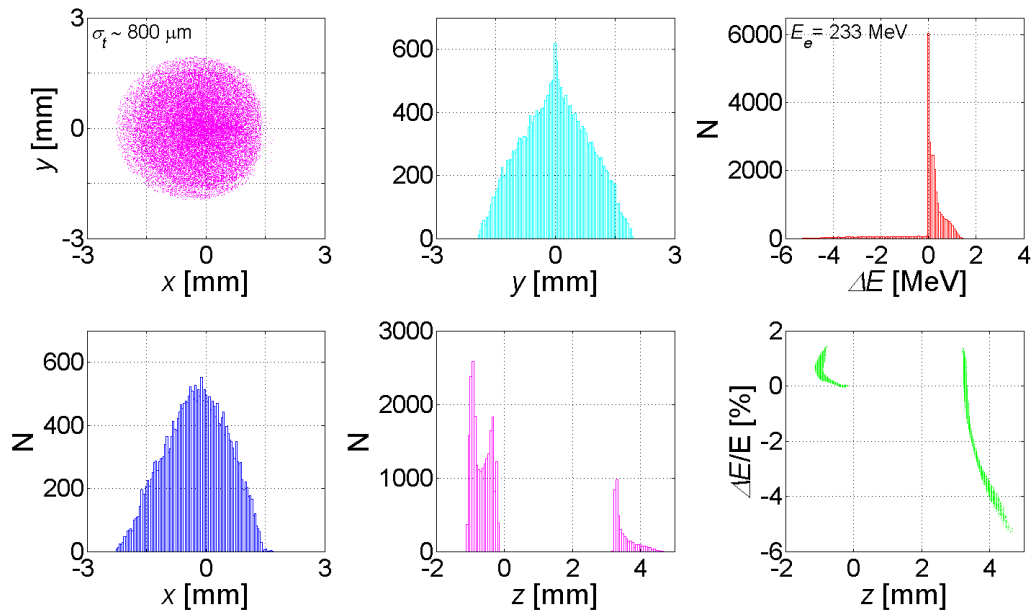


Figure 3.33: Dark current Transverse and longitudinal phase space at LE IP as obtained by Elegant simulations. Wakefield and CSR effects are switched-off and the machine model is set up with the design optics for tracking the nominal 250 pC electron beam with a final energy of 234 MeV at the LE-IP.

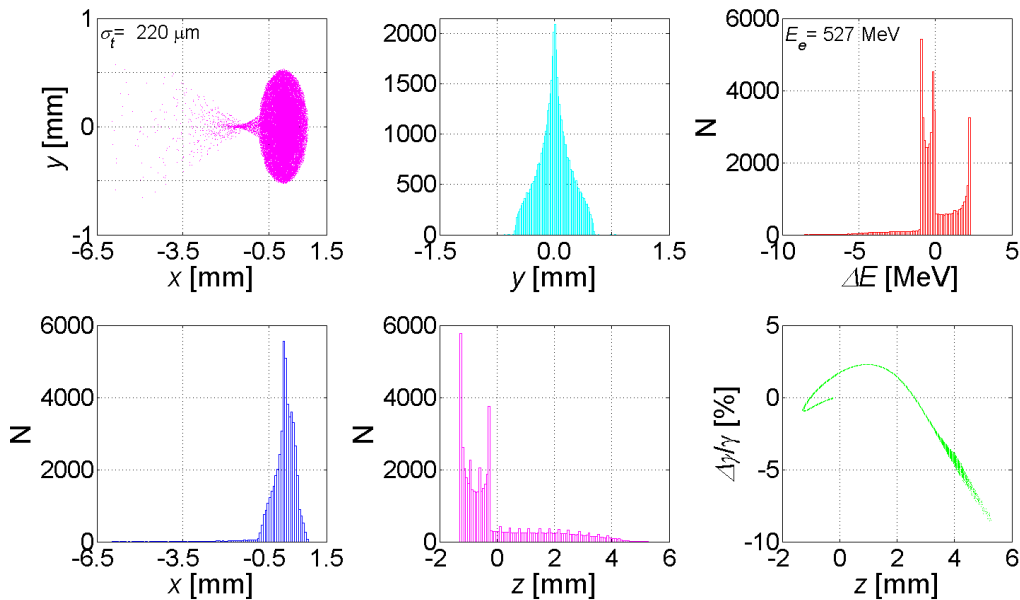


Figure 3.34: Dark current Transverse and longitudinal phase space at HE IP as obtained by Elegant simulations. Wakefield and CSR effects are switched-off and the machine model is set up with the design optics for tracking the nominal 250 pC electron beam with a final energy of 530 MeV at the HE-IP.

3.7 Final Considerations

Optimisation studies for the beam dynamics in the ELI-NP GBS RF linac have been described to provide an electron beam at the interaction point such to optimise the γ -ray source performances for several Working Points, each corresponding to the user required γ -photon beam energy.

Start to end simulations of the machine have been addressed also including the effects of wakefields and quasi-constant accelerating field profile in the C-band RF linac on the beam dynamics of the nominal 250 pC electron beam with final 234 MeV energy. Studies on wakefield effects have been described in both single and multi-bunch operation. In particular, the study of the longitudinal beam dynamics in the multi-bunch operation shows an energy modulation along the bunch train and leads to take care of the beam loading effect, underlining the importance of the full beam loading compensation proposed in [81]. In the next future the study will be extended to the electron beam dynamics in the RF gun and in the two S-band SLAC type TW cavities. Further the transverse long-range wake fields will be treated in order to estimate the multi bunch beam break up effect on the transverse phase space. Effects on the beam dynamics of quasi-constant accelerating field profile in the C-band RF linac have been investigated and possible cures have been suggested to provide an electron beam at the IP compliant with the specifications in Table 3.1.

The optimisation work on the electron beam dynamics of the ELI-NP Gamma Beam System has been also described regarding machine sensitivity studies aiming to check the robustness of the source in terms of jitter and misalignments. A tolerance range has been indicated in Table.3.5 and the obtained simulation results have been presented satisfactorily close to the nominal machine parameters. Other type of deviations as steerer magnets and BPM alignment errors will be considered next to complete the analysis towards the multibunch operation sensitivity studies.

Finally the dark current contribution has been reported to quantify beam losses along the transfer line and in the dumpers driving to the design specifications for the shielding and the radiation safety system of the linac tunnel.

In view of the ELI-NP machine future commissioning in Magurele under the INFN responsibility, to which I will take part, the commissioning strategies are under study including also the high level applications to be used for the machine installation and stabilization (as the beam base alignment procedure or dispersion free steering method) and for the transport of the electron beam at the interaction point through on-line mea-

surements and feedback loops to optimise the final source luminosity.

SPARC_LAB RF linac and TS Beamline

Contents

4.1	The SPARC_LAB Test Facility	69
4.2	TS Experimental Setup	73
	Electron Beam Dynamics	75
	FLAME Laser System	78
	Synchronization	79
	Interaction Region	81
	X-ray beam diagnostics	83
4.3	Commissioning Results	83
	First commissioning phase	84
	Second commissioning phase	89
4.4	Final Considerations	95

4.1 The SPARC_LAB Test Facility

SPARC_LAB [93], Sources for Plasma Accelerators and Radiation Compton with Lasers and Beams, is a test facility located at the INFN National Laboratories in Frascati, merging the potentialities of the SPARC_LAB high power high intensity laser system, named FLAME [96], and the former SPARC project [97], a collaboration among INFN, ENEA and CNR approved by the Italian Ministry of Research in 2001.

The SPARC project, installed at the INFN National Laboratories in Frascati, has been mainly devoted to the R&D activity on ultra-brilliant electron beam photo injector and on FEL physics. The test facility hosts a 180 MeV high brightness photo injector [98] which feeds a 12 m long undulator; the versatile machine layout allowed the investigation of several beam manipulation techniques and linac matching schemes, as the emittance compensation process in the gun region [71, 72], the velocity bunching scheme to apply an RF beam compression through the photo injector with emittance preservation [49, 99], the experimental observation of the double-emittance minimum [42], and so on and so forth. The expertise acquired on the repeatable and stable production, manipulation and control of high brightness electron beams enabled the observation of FEL radiation in the SASE [100, 101], Seeded [102] and HHG [103] modes with wavelength from 500 nm down to 40 nm. In addition a high power RF linac based THz radiation source has been installed at SPARC and fully characterised [104, 105].

The FLAME laser system is a nominal 250 TW laser linked to the SPARC linac and mainly devoted to explore laser-matter interaction, in particular with regard to laser-plasma acceleration of electrons [106] and protons [107] in the self injection and external injection modes.

At SPARC LAB the unique combination of these two systems enables to explore a wide spectrum inter-disciplinary leading-edge research activity based on advanced radiation sources - as FEL experiments, X-rays generation by means of Thomson back-scattering [64, 108, 63] and high peak power, narrow-band THz radiation [109] - and to investigate the plasma acceleration with different configurations, i.e. self and external injection, laser and particle beam driven. The scheme layout of the test facility is reported in Figure 4.1: the RF gun (1) is followed by an hybrid linac consisting of two S-band and a C-band TW structures (2), a THz source station and a vacuum chamber devoted to plasma-based experiments (3); the downstream 14 degree dipole (4) delivers the electron beam towards four beam lines devoted to FEL physics (5) both in SASE and with seed-laser (10), beam diagnostics (6), and to the interaction points of the Thomson source (8) and plasma acceleration external injection (7) experiments. Looking at Figure 4.1 it has to be mentioned that an upgrade of the RF linac took place in 2016 by installing a new high gradient C-band structure, developed at LNF [110] in the framework of the ELI NP collaboration [58]; in the new layout an S-band TW structure, the third one in Figure 4.2 (see 4.2), has been removed and replaced with the vacuum chamber which is hosting the plasma-based experiments. The vacuum chamber is embedded with permanent magnets devoted to the injection and extraction matching of the

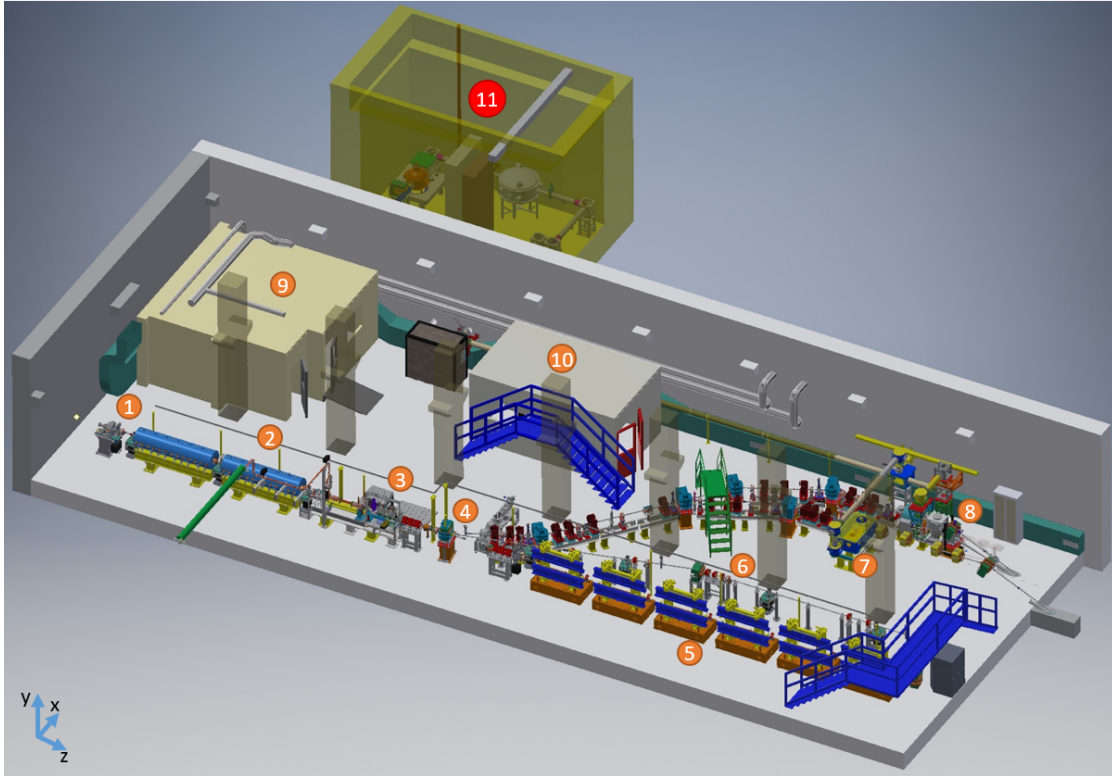


Figure 4.1: SPARC_LAB layout: the RF gun (1) is followed by an hybrid linac consisting of two S-band and a C-band TW structures (2), a THz source station and a vacuum chamber devoted to plasma-based experiments (3); the downstream 14 degree dipole (4) delivers the electron beam towards four beam lines devoted to FEL physics (5) both in SASE and with seed-laser (10), beam diagnostics (6), and Thomson back-scattering (8) and plasma acceleration external injection (7) experiments using the FLAME laser pulse (11).

electron beam in the capillary region where the resonant PWFA, the so called COMB experiment, is foreseen. At this purpose a huge experimental campaign is on going in order to characterise the capillary region [111, 112] and to explore a new focusing device to match the electron beam at plasma injection or extraction, the so called active plasma-lens [113].

Recently the SPARC_LAB activity has been mainly focused on the manipulation of a train of short electron bunches generated by means of a new technique called Laser Comb [114]; the latter has been successfully tested and detailed reported in [115, 116]. In this operating mode the photocathode is illuminated by a comb-like laser pulse to extract a train of electron bunches which are injected into the same RF bucket of the gun. The SPARC laser system, based on a Ti:Sa oscillator has been upgraded to pro-

Table 4.1: SPARC_LAB Thomson source design parameters.

Electron Beam Parameters @IP		
all values are rms		
Charge	100 - 800	pC
Energy	30 -150	MeV
Energy Spread	<0.1	%
Pulse Length	15 - 20	ps
Spot Size	5 - 20	μm
Emittance	1 -3	mm mrad

FLAME Laser Beam Parameters @IP		
Pulse energy	1 -5	J
Wavelength	800	nm
Pulse Length [r.m.s.]	6	ps
Spot Size	10	μm
Repetition Rate	10	Hz

X-ray Photon Beam Specifications		
Energy	20 -250	keV
Spot Size [r.m.s.]	10	μm
Bandwidth [r.m.s.]	10	%
Photon Flux	10^9	Photons per pulse in <i>bw</i>

duce a train of short electron bunches, of the order of hundreds of femtoseconds or less, with picosecond time separation. These kind of beams are routinely generated at SPARC_LAB for several applications: tailored electron beams modulated both in time and energy have been characterised and used to customise the emission bandwidth and temporal properties of radiation sources such as free-electron lasers [115, 117] and THz radiation sources [98, 118, 119]; train of short bunches are also useful in plasma-based experiments and more detail in they have been produced using RF compression by velocity-bunching for PWFA applications [120] and for LWFA [121].

A Thomson backscattering source is also under commissioning at the SPARC_LAB test facility. The opportunity has been used to couple the SPARC high brightness photoinjector with the high power FLAME laser system in order to provide a quasi coherent, quasi monochromatic X-ray source. Here a head on collision is foreseen at the Thom-

son Interaction Point between a 30 to 150 MeV electron beam and the 250 TW FLAME laser pulse, providing a photon energy tunable in the range of 20 to 250 keV. The first experiment foresees the generation of a X-ray beam, useful for X-ray imaging of mammographic phantoms with the phase contrast technique [108] and the optimised design parameters useful for such application are listed in Table 4.1. In the February 2014, the SPARC_LAB Thomson Source produced its very first X-ray beam [84, 122], and in June 2015 a second commissioning phase took place to improve the source performances [85].

In the first section of this chapter the SPARC_LAB Thomson Source is detailed described with regards to its applications; in the second section the Thomson Source experimental setup is illustrated and then in the following first and second shift commissioning results are reported.

4.2 TS Experimental Setup

The X-ray imaging is essentially based on the analysis of intensity or phase variations of an X-ray beam passing through a sample in order to create its image. Nowadays, the most relevant techniques are the standard X-ray imaging and the, more innovative, phase contrast X-ray imaging. The standard X-ray imaging studies the attenuation of the intensity of the X-ray beam, while the phase contrast technique relies on the phase variation of the X-ray beam. It is well known that this technique presents some advantages with respect to the conventional one, in particular when low energy X-ray beams are required as in the case of medical imaging. For example many studies demonstrated that in breast radiography the best image quality at constant dose is obtained using 20 keV photon beam. In tissues such as the breast, which is mainly adipose and glandular, the radiation is more absorbed, reducing the detectable signal and the sharpness of the image and it becomes even more complicated to distinguish healthy tissue from tumours. A solution can be to take advantage of the edge enhancement effect, one of the peculiarities of the phase contrast X-ray imaging that became a very promising technique even more for medical application in the last years. Despite the introduced benefits, this technique requires very performing X-ray sources that have to generate monochromatic, spatially coherent photon beam and photon flux of the order of 10^{10} photon/s. Moreover photon beam energy has to change in relation to the patient physical characteristics. Nowadays such a beam can be produced in synchrotron radiation facilities, but, due to their huge dimensions and high costs, they cannot be inserted in routine clinical

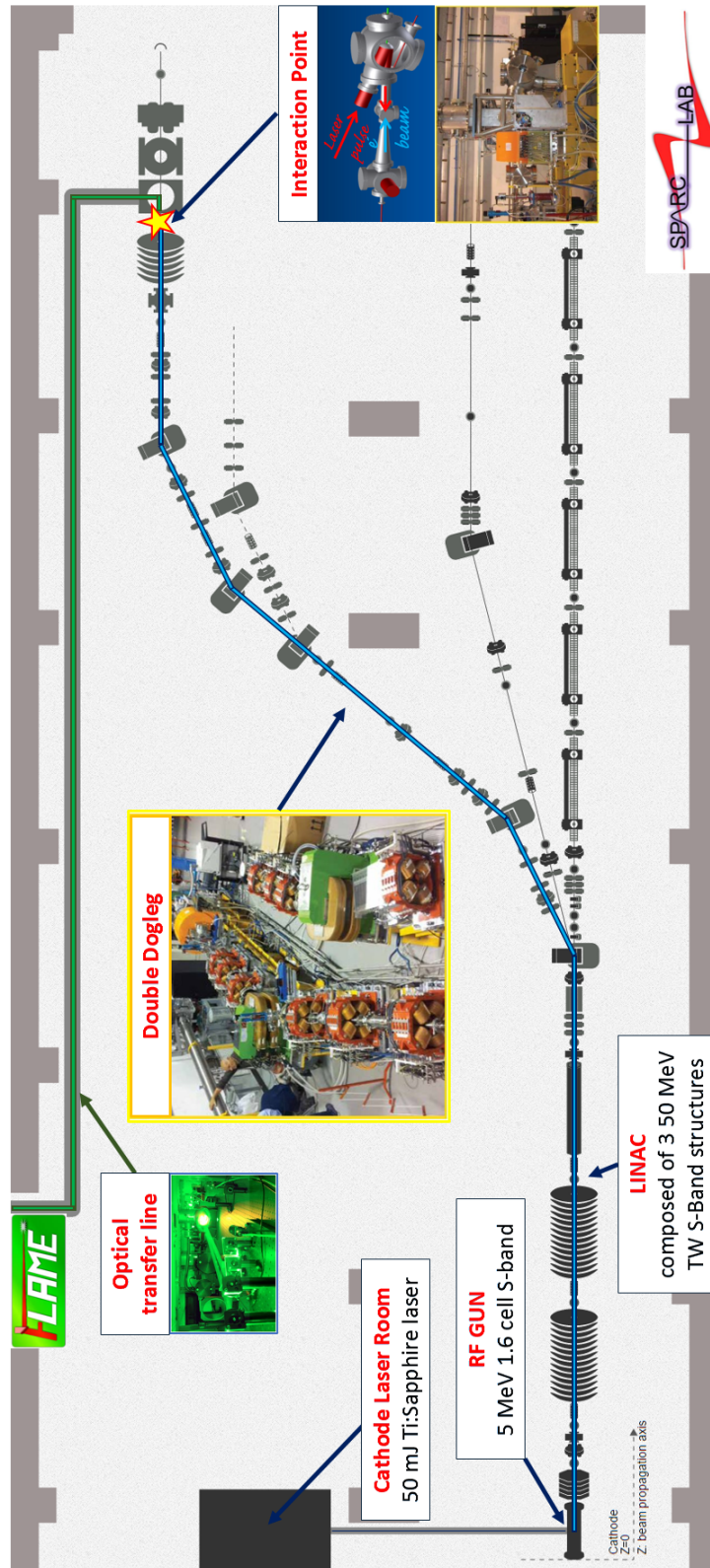


Figure 4.2: Thomson Source schematic layout: FLAME laser pulse, passing through a 20 meter long optical beam line in vacuum, collides at the Thomson Interaction Point (IP) with the electron beam coming from the SPARC LAB high brightness photo injector.

practice. This problem could be fixed generating X-rays through Thomson backscattering; the sources based on this phenomenon have become more and more attractive due the large variety of applications in biological, medical and industrial science and the relatively compactness of the whole apparatus.

At SPARC_LAB Thomson source the first experiment foresees the generation of a X-ray beam of moderate mono-chromaticity (20 %) and energy tunable in the range 20 - 250 keV useful for X-ray imaging of mammographic phantoms with the phase contrast technique.

Electron Beam Dynamics

The RF linac layout The SPARC S-band photo-injector, operating at 2.856 GHz, is composed of a 1.6 cell S-band RF gun equipped with a copper photo cathode and an emittance compensation solenoid, followed by three 50 MeV TW SLAC type S-band sections [66]; two compensation solenoid surround the first and the second S-band cavity enabling the operation in the velocity bunching scheme through the linac with emittance preservation. The gun solenoid design consists in four coils that can be powered independently with alternate signs providing a better compensation for alignment errors and multipolar components; a steerer, placed downstream the emittance compensation solenoid, deflects the beam allowing to control the trajectory in the critical phase of the injection in the first travelling accelerating section. The electron beam is generated in the RF gun by a 50 mJ Ti:Sapphire laser pulse (9 in Figure 4.1) hitting on the Cu photocathode with $\sigma_r \simeq 1$ mm and $\sigma_z \simeq 6$ ps. At the gun exit the beam energy is ~ 5 MeV and the three following TW SLAC type S-band sections, carry the electron beam up to the required energy (maximum 150 MeV). A double dogleg transport line downstream the linac exit provides on left side an off axis deviation of about 6 m, such to overcome the limitations due to the SPARC building plan, and delivers the beam at the Interaction Point (TS IP), avoiding in this way the bremsstrahlung radiation contribution. In the TS IP region a focusing system, consisting in a quadrupole triplet coupled with a solenoid, provides a flexible final focusing for matching the electron beam spot size vs the counter-propagating laser pulse. The Figure 4.2 shows the Thomson Source schematic layout: FLAME laser pulse, passing through a 20 meter long optical beam line in vacuum, collides at the Thomson Interaction Point (IP) with the electron beam coming from the SPARC_LAB high brightness photo injector.

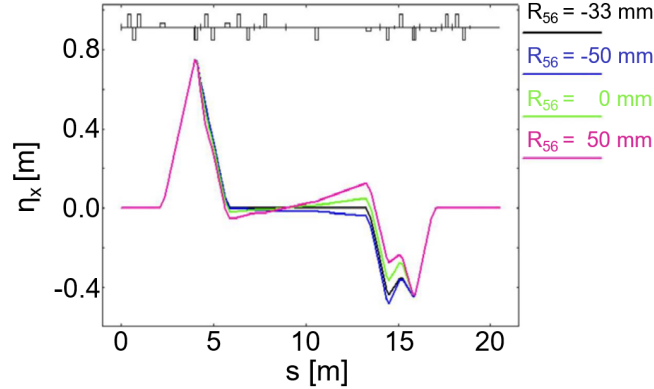


Figure 4.3: Double dogleg R_{56} tunability and relative horizontal dispersion plot as obtained by simulation studies. The R_{56} parameter of the dogleg, that represents the correlation between the z and the $\Delta E_e/E_{e0}$, can be set in the range of ± 50 mm.

Beam Dynamics Simulations Intense beam dynamics studies have been performed to provide the electron beam at the IP with the required parameters (listed in Table 4.1). The electron beam, composed of 50 k macro particles, is generated in the photo injector with Astra [51] and Tstep [50] code and then is injected in the double dogleg transfer line. The beam dynamics optimisation in the photo-injector follows the criteria imposed by the invariant envelope theory and a fine tuning of the gun solenoid allows to minimise the emittance at the double dogleg transfer line injection; the energy spread is cured with a proper off-crest operation depending on the particular electron beam energy required at the TS IP and the process is detailed explained in 4.3. The Trace 3D code [53], that includes the space charge forces, has been used for the beam matching, starting from the linac exit, to provide a 10 - 50 μm beam spot size at the IP; indeed our final beam energy will be ever lower than the beam transition energy between the space charge and the emittance dominated regime, and so space charge effects are not negligible. Transfer line simulations aim to properly set the Thomson Interaction Point focusing system and to correct the horizontal dispersion in the double dogleg. The R_{56} parameter of the dogleg, that represents the correlation between the z and the $\Delta E_e/E_{e0}$, can be set in the range of ± 50 mm. The R-matrix is the transfer matrix between two locations, s_1 and s_2 , of the charged particle through a beam transport line, whose elements depend on the transport between s_1 and s_2 and on the beam spot size (for computing space-charge forces) in this interval [123]. At any position s , measured along a reference trajectory, a charged particle can be described by a 6x1 vector $\mathbf{X}(s)=(x(s),x'(s),y(s),y'(s),z(s),\Delta E_e/E_{e0})$ where: $x(s)$, $y(s)$ and $z(s)$ are the horizontal, vertical and longitudinal displacements of the tra-



Figure 4.4: Output signal of this device in the final beamline configuration: the coloured lines in the two graphs represent the losses captured by a series of optical fibers along the line; the peak values correspond to the end of the line (the signal is reflected being the optical fiber non-adapted at the end). In this case the transport current has been optimised and any losses are present in the line up to the IP.

jectory (with respect to the central trajectory); $x'(s)$ and $y'(s)$ are the angles this trajectory makes in the horizontal and vertical plane; $\Delta E_e/E_{e0}$ is the longitudinal momentum deviation of the trajectory (with respect to the central trajectory). The Figure 4.3 shows the double dogleg R_{56} tunability and the relative horizontal dispersion plot.

Electron beam diagnostics The electron beam characterisation is essential to properly match the RF linac and the transfer line in order to provide the required beam at the IP. The beam envelope is captured in several position along the machine and in particular at the gun exit, at the linac exit and at the TS IP (see 4.2); more detail in the imaging get on the screen mounted at the gun exit is also useful for the beam energy

measurement, provided by means of the beam deflection by varying the current of a steerer (horizontal or vertical) upstream the screen, and to centre the beam on the photo cathode. Beam current monitors are placed at the gun and linac exit and after the third dipole in order to optimise the beam charge transport up to the IP; more detailed the current measurements at the gun exit together with a fine RF injection phase scan enables the identification of the proper injection phase needed to maximise the beam energy gain. The transport current optimisation has been possible also thanks to the insertion of beam loss monitors, available from the second dipole up to the IP. In Figure 4.4 is shown the output signal of this device in the final beamline configuration: the coloured lines in the two graphs represent the losses captured by a series of optical fibers along the line; the peak values correspond to the end of the line (the signal is reflected being the optical fiber non-adapted at the end). In this case the transport current has been optimised and any losses are present in the line up to the IP. At the linac exit the 6D phase space characterisation is provided by a S-band RF deflecting cavity [68] coupled with a 14° by-pass dipole, (4) in Figure 4.1, together with the emittance measurement by means of quadrupole scan technique. The latter can be done also in other diagnostic stations placed in the straight-on branch of the first dogleg and at each straight section of the Thomson transfer line; also the energy and the energy spread can be measured in these stations using the three dipoles of the double dogleg transfer line. Finally the beam trajectory is measured thanks to beam position monitors along the machine and at the interaction region entrance and exit.

FLAME Laser System

The laser pulse used to drive the Thomson back scattering process with the SPARC electron beam is provided by the FLAME laser system. FLAME is a nominal 300 TW Ti:Sa, chirped pulse amplification laser system that uses 11 YAG pump lasers and 5 titanium - sapphire multi-pass amplifiers to produce linearly polarized pulses with a central wavelength λ_0 800 μm in a 60 - 80 nm bandwidth. The pulse duration ranges between 25 fs and 10 ps, and the maximum energy is $E = 7$ J that corresponds to an energy on target $E_t = 5$ J, at the 10 Hz repetition rate. The laser system is hosted in a clean room at the ground floor of the FLAME building and is optically transported in a shielded underground area where the compressor is located and that is adjacent to the SPARC hall. From here an optical transfer line in vacuum $P=10^{-6}$ Torr carries the beam up to the off-axis parabolic mirror of the Thomson interaction chamber, see



Figure 4.5: 3D CAD drawing of the Thomson Interaction vacuum chamber setup on the left. Lateral view of the implemented interaction chamber and parabolic mirror vacuum chamber on the right.

Figure 4.5, that focuses the beam in a $10 \mu\text{m}$ diameter (FWHM) spot at the interaction point; the parabolic mirror is holed in its centre, in order to allow the passing through of the scattered radiation and of the electron beam. The required focal spot has been obtained with the use of the adaptive optic placed inside the compressor used to control the phase-front of the photon beam. The Figure 4.6 shows the measured beam spot at the focus (TS IP) without (left side plot) and with the phase-front correction (right side plot): the beam is quite oval in the case of no phase front correction and becomes nearly round when the best phase front is applied. Moreover, it is perceptible that the use of the adaptive optics is crucial also for the energy contained in the central spot (considering the $1/e^2$ diameter): indeed after the phase front correction the percentage of the total energy of the laser pulse in the central spot increases from 25 % up to 60 %.

Synchronization

The Thomson scattering experiment needs an extremely precise synchronization between electron bunch and laser pulse. The electrons and the photons collide well inside the waist region of the laser beam of final focus provided that the relative time of arrival jitter at the IP between the two beams is $\leq 500 \text{ fs}_{RMS}$. The bunch time of arrival at the IP depends on the arrival time of the laser on the photocathode and on the phase of the RF accelerating fields. The arrival time at the IP of the extremely intense IR laser pulse depends on the starting time of the seed pulse, which is selected from a laser oscillator pulse train and then amplified, compressed and transported. The synchronous arrival of electrons and photons at the IP is obtained by locking the oscillators of the photocathode laser and interaction laser systems, and the phase of the RF accelerating fields

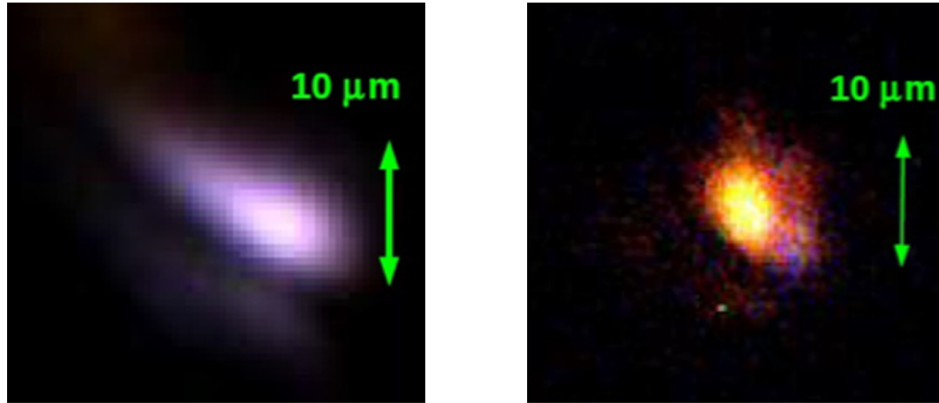


Figure 4.6: Measured beam spot at the focus (TS IP) without (left side plot) and with the phase-front correction (right side plot): the beam is quite oval in the case of no phase front correction and becomes nearly round when the best phase front is applied. Moreover, it is perceptible that the use of the adaptive optics is crucial also for the energy contained in the central spot (considering the $1/e^2$ diameter): indeed after the phase front correction the percentage of the total energy of the laser pulse in the central spot increases from 25 % up to 60 %

to a common Reference Master Oscillator (RMO). The RMO is a low phase noise (60 fs_{RMS} integrated in the 10 Hz - 10 MHz range) microwave oscillator tuned at the Linac main frequency 2856 MHz. The laser oscillators are locked through a PLL architecture to the 36th sub-harmonics of the RMO, while the output RF phase of the linac klystrons is downconverted to baseband by mixing with the RMO signal, and deviations are corrected both within the $4 \mu\text{s}$ RF pulse duration (jitter feedback) and pulse-to-pulse (drift feedback). The jitter of the bunch arrival time at the end of the linac has been measured relative to the klystron RF streaking the bunch on a screen by means of an RF deflecting cavity and recording shot to shot the bunch centroid vertical position. In alternative the bunch arrival time has been measured relative to the photocathode laser using the Electro Optical Sampling technique [124]. The measured jitter of the bunch arrival time is $< 100 \text{ fs}_{RMS}$ with both methods, that in our implementation present a similar estimated resolution of $\approx 20 \text{ fs}_{RMS}$. Once locked to the RMO, the measured absolute integrated phase noise of the interaction laser FLAME oscillator is $\approx 100 \text{ fs}_{RMS}$, and we do not expect significant performance degradation by the laser amplification and transport. So the expected relative jitter of the arrival time at IP of electron bunch and laser pulse is well below the 500 fs_{RMS} specification. Once locked both to the RMO, the control window of the PLLs, implemented on the photo-cathode and interaction lasers, gives

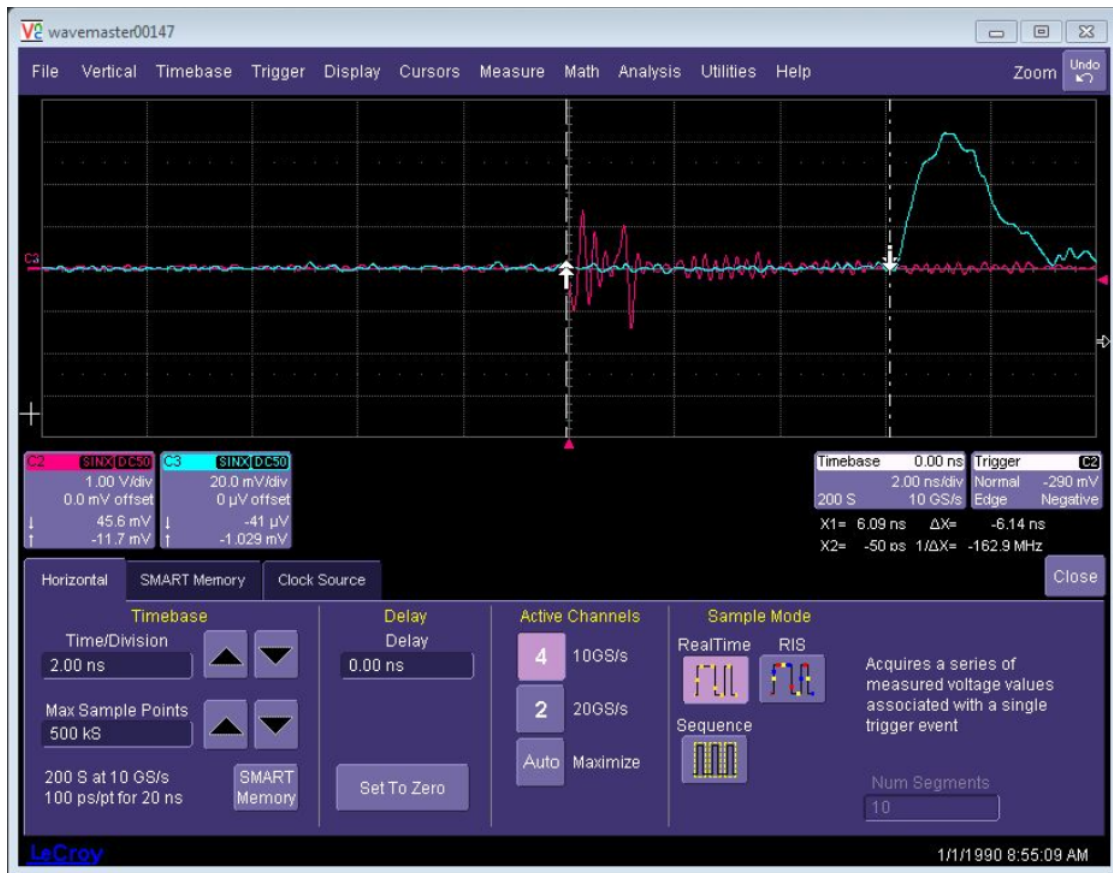


Figure 4.7: signals induced by electron and photon pulses in pick-ups placed close to the IP. Taking into account the time-of-flight from pick-up to IP, this measurement allows a coarse temporal pre-alignment of the beams, while a fine temporal superposition can be found experimentally by maximizing the flux of the Thomson radiation.

the possibility of freely phasing the two systems at any desired position. Figure 4.7 shows the signals induced by electron and photon pulses in pick-ups placed close to the IP. Taking into account the time-of-flight from pick-up to IP, this measurement allows a coarse temporal pre-alignment of the beams, while a fine temporal superposition can be found experimentally by maximizing the flux of the Thomson radiation.

Interaction Region

The head-on interaction between the electron and the collision photon beam takes place in a tee-vacuum chamber shown in Figure 4.5, that is equipped with a double screen movement to get the beam imaging at the IP; upstream a vacuum chamber hosts electron beam diagnostics for both imaging and emittance measurements, and down-

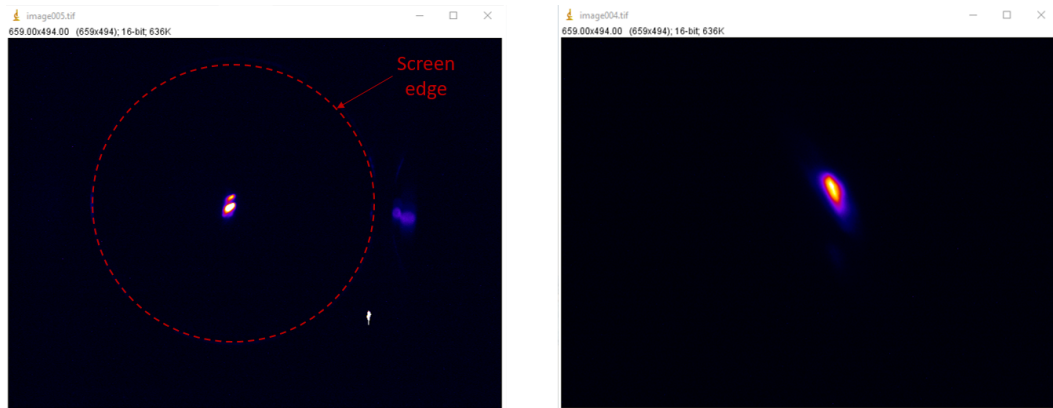


Figure 4.8: Electron beam imaging at the IP captured without (left side plot) and with the camera that provides the on-line setting of the zoom and focus. The camera is mounted on a remote controlled movement allowing to select the zone of the screen occupied by the beam and to change the resolution from ~ 30 to $10 \mu\text{m}/\text{pixel}$ or less, required to detect a beam spot size of the order of $10 \mu\text{m}$ and to provide the needed alignment accuracy.

stream another vacuum chamber determines the in trajectory of the FLAME pulse and hosts the off-axis parabolic mirror that focuses the laser pulse at the interaction point.

The reference line for the Flame laser beam alignment is the one passing through the magnetic centres of the focusing quadrupole triplet and the IP solenoid as coming from the magnetic measurements. This reference line is adopted to set the He-Ne laser at the entrance of the last dogleg dipole to sight the light path up to the Thomson radiation window exit. In this way the alignment laser image on the screens placed along the beam-line provides the guide line for the Flame laser beam.

Starting from the second commissioning phase the imaging of the electron beam and the FLAME pulse at the IP can be provided on the same screen leading to an improvement of the on-line alignment procedure between them; further a camera mounted on a remote controlled movement enables an on-line setting of the zoom and focus to select the zone of the screen occupied by the beam and to change the resolution from ~ 30 to $10 \mu\text{m}/\text{pixel}$ or less, required to detect a beam spot size of the order of $10 \mu\text{m}$ and to provide the needed alignment accuracy. The electron beam imaging at the IP captured without (left side plot) and with such a camera is reported in Figure 4.8 as obtained in June 2015.

X-ray beam diagnostics

Since in first collisions the radiation signal could be not optimised, a detector having a high sensitivity and a wide dynamic range has been selected to detect a potentially weak signal: a CsI(T1) crystal of size (20x20x2) mm³, coupled with a photomultiplier tube (Hamamatsu, mod. R329-02), has been placed 4 meter away from the source along the X-rays propagation axis and mounted on an x-y movement for the fine position adjustment. The detector has been calibrated to detect, for a 60 keV monochromatic radiation, the signal produced by a single photon up to the one due to pulses containing about 10⁶ photons.

Two different devices, both connected at a PC, are foreseen for X-rays: a 20 GHz BW oscilloscope for a fast response and a multichannel analyser (MCA-8000, Amptek, US) to acquire an integral measurement over various interactions. Due to the high intensity and short duration of the pulse, it is not possible to distinguish the signal produced by the interaction of each single photon in a pulse, as in traditional spectroscopic application, but the signal is proportional to the entire energy released in the scintillator by each pulse. Therefore, an information on the energy distribution is required to evaluate the number of photons in each pulse.

The diagnostic tool is also equipped with a set of detectors, with techniques specifically developed [125, 126], in order to provide a full characterization of the source in terms of flux, energy distribution, spatial distribution and beam stability.

4.3 Commissioning Results

The commissioning of the SPARC.LAB Thomson Source started in 2014 and produced its very first X-ray beam [84, 122] in February 2014 with: $\langle E \rangle = 60$ keV, BW = 19 %, Number of photons per shot of 6.7×10^3 . In this phase the source performances and stability have been strongly limited by problems related to the solenoid cooling system and misalignment of the interaction chamber and the electron dumping section, located downstream the parabolic mirror vacuum chamber, i.e. too much close to the X-ray radiation extraction. In the June 2014 shut-down a dumping dipole immediately after the interaction point has been inserted, to avoid any background contribution from the dumping beam line. In June 2015 a second commissioning phase took place to improve the source performances and to fulfill a complete characterization of the X-ray source in terms of flux, energy distribution, spatial distribution and beam stability [85].

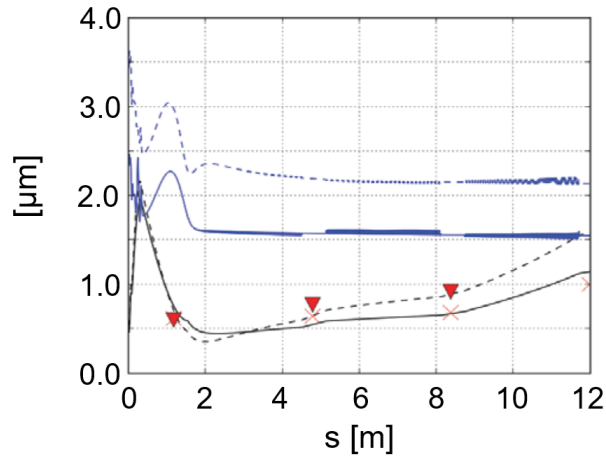


Figure 4.9: Electron beam emittance (blue curves) and envelope evolution (black curves) from the photo-cathode to the linac exit calculated with the Astra code. The crosses and triangles represent the beam spot measurements taken in this configuration at screen locations along the linac.

Also the diagnostic tool has been upgraded with a set of detectors filters, Nb and Zr, to estimate the radiation energy two k-edge. In the following sections the first and second commissioning phase setup and results are detailed described.

First commissioning phase

The Electron Beam For the first commissioning phase a 50 MeV, 200 pC electron beam has been chosen as working point and characterised at SPARC_LAB [84, 122].

The beam emittance and envelope evolution through the photoinjector has been simulated with the Astra code and 50k particles; the results are shown in Figure 4.9 together with the beam spot measurements taken at the screen locations along the linac. From the transverse emittance measurement performed at the linac exit the Twiss parameters are obtained to match the beam to the dogleg entrance for the transport and focusing at the Thomson Interaction Point. For the commissioning phase the dispersion is closed at the end of each dipole pair and the focusing system is set to obtain a 10 - 50 μm beam spot size. The Twiss parameters are reported in Figure 4.10 as obtained with Trace 3D code.

In order to minimise the effects of the power amplitude jitter from the feeding Klystrons, the phases of the accelerating sections have been set as follows to : $\Phi S_1 = -$

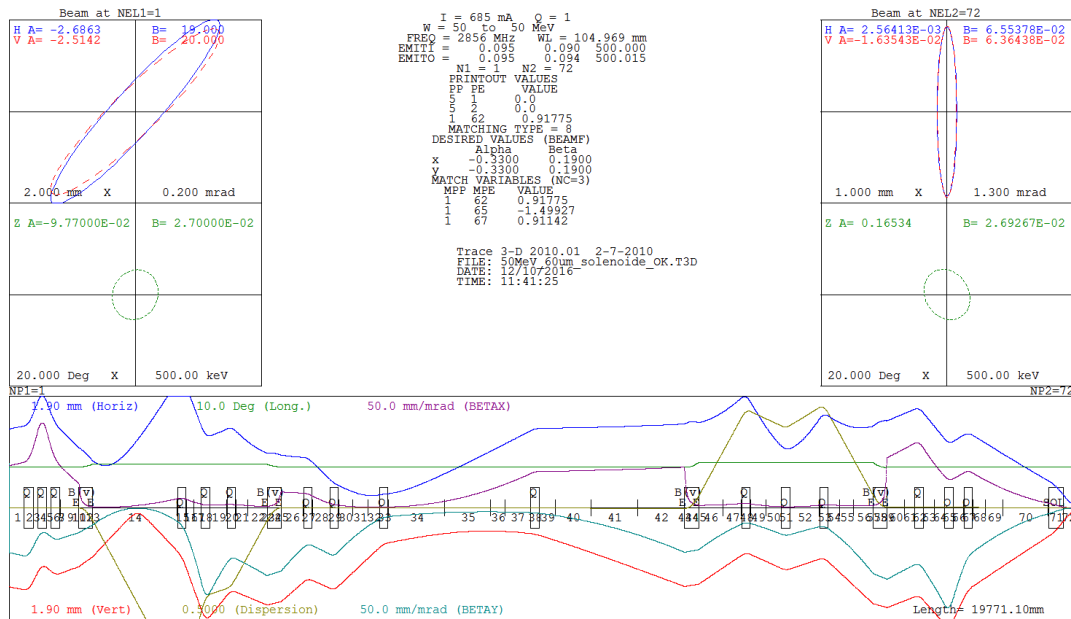


Figure 4.10: Twiss parameters and envelope evolution from the linac exit to the Thomson IP obtained with the TRACE3D code.

26.2° , $\Phi_{S2} = + 78.5^\circ$, $\Phi_{S3} = - 111^\circ$. In these conditions the electron beam energy jitter was less than 0.02 MeV and the spread was less than 0.1 %. The plots in Figure 4.11 show the energy measurements obtained by means of the 14 deg dipole and longitudinal phase space measured with the S-band RF deflecting cavity coupled with a 14° by-pass dipole; the plots in Figure 4.12 show the measured beam energy and current longitudinal profile related to the longitudinal phase space in Figure 4.11. The emittance evolution measurement is performed with the quadrupole scan technique in each straight section downstream the dipole pairs and result in measured emittance ranging in 1 - 3 mm mrad.

Because of a limit in the magnet cooling system, for which an upgrade took place in the June 2014 shutdown, the solenoid upstream the IP could be used at 70 % of its nominal value. In this condition the minimum rms spot size captured on the YAG screen located at the IP was of $90 \pm 3 \mu m$, see Figure 4.13, nevertheless, due to a poor overlap of the colliding beams, the best result has been obtained for an enlarged electron beam spot size of $\sigma_{xy} = (240 - 160 \pm 10) \mu m$.

In Table 4.2 are presented the beam parameters measured at SPARC.LAB Thomson source for the working point of the first commissioning phase with best performances in terms of X-ray flux.

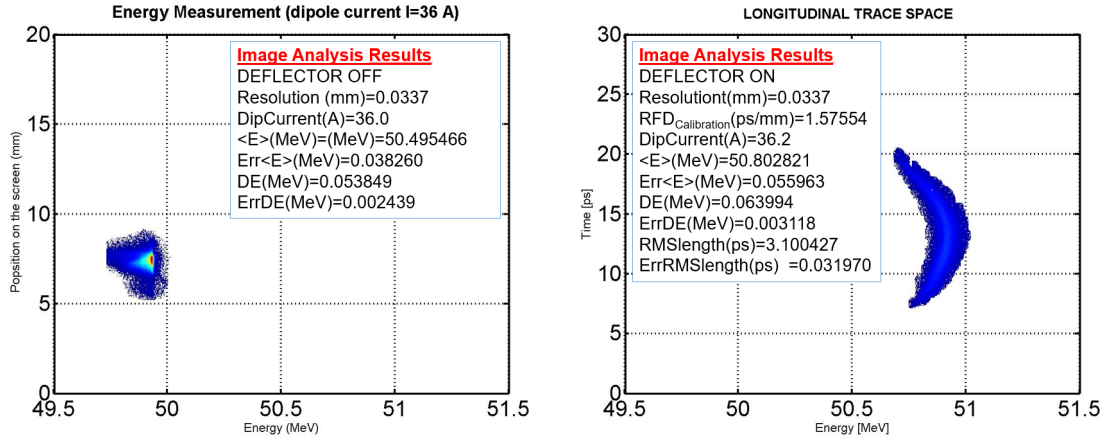


Figure 4.11: Energy measurements obtained by means of the 14° dipole (left side plot) and longitudinal phase space measured with the S-band RF deflecting cavity coupled with a 14° by-pass dipole (right side plot).

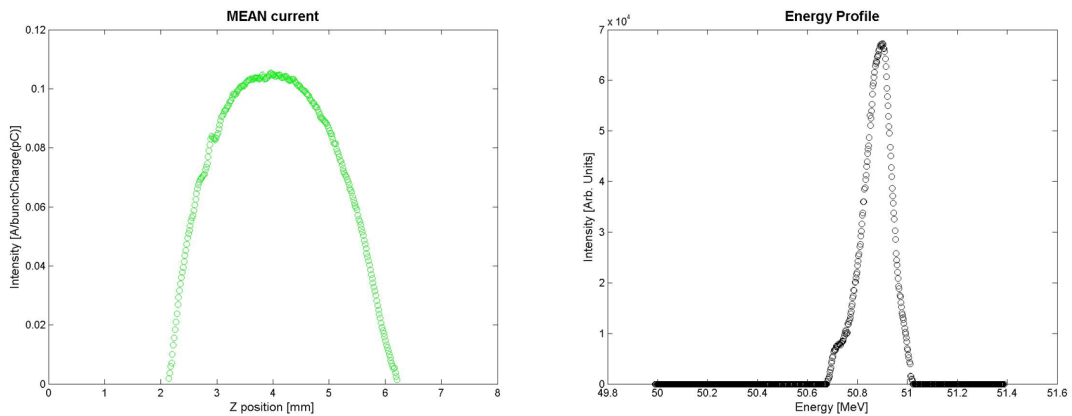


Figure 4.12: Measured beam energy (left side plot) and current longitudinal profile (right side plot) related to the measured longitudinal phase space in Figure 4.11.

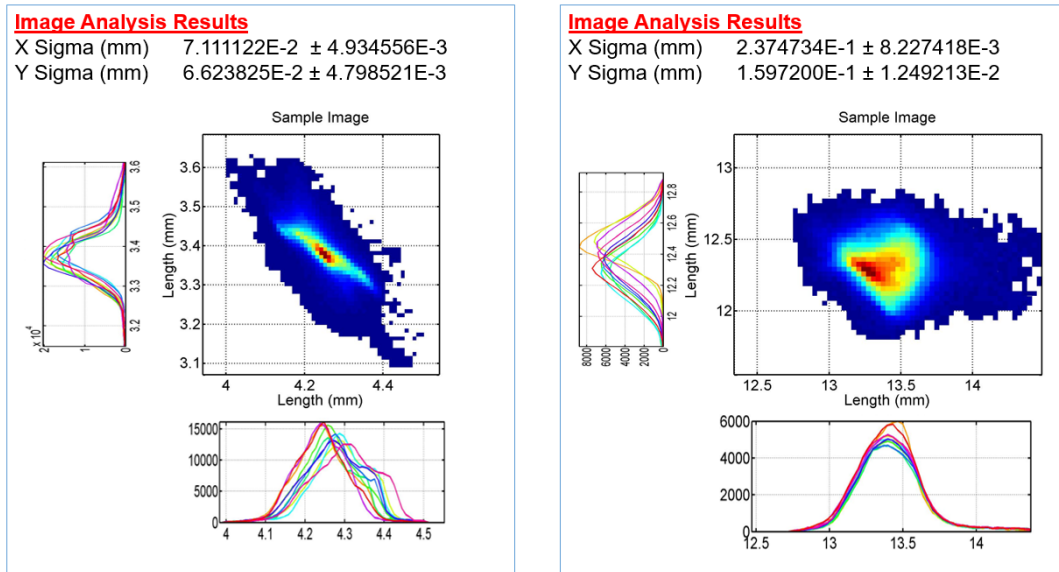


Figure 4.13: Minimum rms spot size captured on the YAG screen located at the IP of $90 \pm 3 \mu\text{m}$ (left side plot) and enlarged electron beam spot size of $\sigma_{xy} = (240 - 160 \pm 10) \mu\text{m}$ which allowed the best result in terms of source flux (right side plot).

FLAME pulse In this very first Thomson Source experiment FLAME provided a 0.5 J laser beam at IP with 6 ps pulse width and $10 \mu\text{m}$ beam spot size. In Table 4.2 are presented the beam parameters measured at SPARC LAB Thomson source for the working point of the first commissioning phase with best performances in terms of X-ray flux.

X-ray Source For the commissioning phase the beams described in Table 4.2 have been chosen to collide at the Thomson IP. In these conditions, in the very first 4-week shift, with an electron beam spot size of $\sigma_{xy} = (240 - 160 \pm 10) \mu\text{m}$, a clear, but still not optimised, X-ray signal has been collected on the detector.

The detected signal has been measured both with the 20 GHz BW oscilloscope and the multichannel analyser as mentioned above. The 20 GHz BW oscilloscope has been mainly useful to synchronise the electron beam and FLAME pulse and allows to measure the 150 fs relative temporal jitter between them. The multichannel analyser has provided the evaluation of average energy of X-ray and of the number of photons produced in the interaction. The detected signal, integrated over 1200 pulses, is shown in Figure 4.14 on the left: the red signal is due to the Thomson X-rays, instead the black one is due to the background noise in case of FLAME pulse switched-off. The back-

Table 4.2: Beam parameters measured at SPARC_LAB Thomson source for the working point of the first commissioning phase with best performances in terms of X-ray flux.

Electron Beam Parameters @IP		
all values are rms		
Charge	200 ± 10	pC
<Energy>	50	MeV
Energy Jitter	0.02	MeV
Energy Spread	0.10	%
Pulse Length	3.1 ± 0.03	ps
Spot Size	$240 - 160 \pm 10$	μm
Emittance	$1.5 - 2.2 \pm 0.2$	mm mrad
FLAME Laser Beam Parameters @IP		
Pulse energy	0.5	J
Wavelength	800	nm
Pulse Length [r.m.s.]	6	ps
Spot Size w_0	10	μm
Repetition Rate	10	Hz
X-ray Photon Beam Parameters		
<Energy>	60	keV
Spot Size [r.m.s.]	10	μm
Bandwidth [r.m.s.]	19	%
Photon Flux	$2 * 10^5$	Photons per pulse in B.W.

ground is synchronous with Thomson x-rays and it is mainly due to radiation produced in the electron beam dumping section located downstream the parabolic mirror vacuum chamber, being it too much close to the X-rays radiation extraction. The average energy of Thomson X-rays, released in the crystal by each pulse, is of about 235 MeV.

By CAIN simulation of the interaction has been possible to evaluate that the average energy of the photons reaching the detector was 60 keV with an average number of photons per each pulse interacting with the detector sensitive area of 6.7×10^3 .

This result has been confirmed by simulations made with a code based on the classical theory [57]: in case of a 50 MeV electron beam with 200 pC charge, 5 mm mrad of emittance and 150 μm spot size rms head-on colliding with a 500 mJ laser pulse with

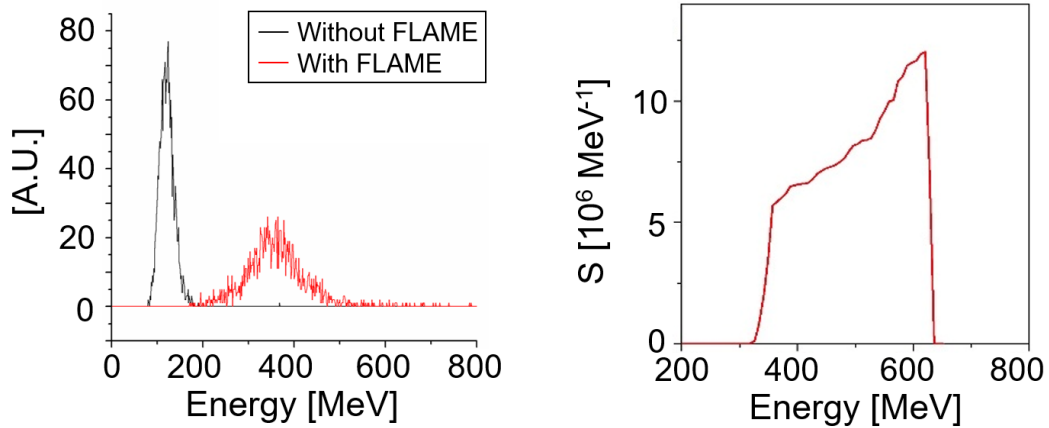


Figure 4.14: Thomson x-rays signal in red, in black the electron background signal (without FLAME laser), integrated over 120 s (1200 pulses) on the left. Spectral density S (MeV^{-1}) versus photon energy on the right.

30 μm beam waist, should be produced a X-ray signal of 2×10^5 photons per pulse in a bandwidth of about 19%. The predicted photon energy edge is of 63 keV given by $E_p \sim 4E_L\gamma^2$. The result is reported in Figure 4.14 on the right. Poor overlap conditions due to some misalignments of the interaction vacuum chamber can explain the difference between the measured number of photons for each pulse and the one expected from the theory.

Second commissioning phase

Electron beam For the second commissioning phase a 30 MeV, 200 pC electron beam has been chosen as working point and characterised at SPARC.LAB [85].

The beam emittance and envelope evolution through the photoinjector has been simulated with the Astra code and 50k particles; the results are shown in Figure 4.15 together with the beam spot measurements taken at the screen locations along the linac. From the transverse emittance measurement performed at the linac exit the Twiss parameters are obtained to match the beam to the dogleg entrance for the transport and focusing at the Thomson Interaction Point. For the commissioning phase the dispersion is closed at the end of each dipole pair and the focusing system is set to obtain a 10 - 50 μm beam spot size. The Twiss parameters are reported in Figure 4.16 as obtained with Trace 3D code.

No RF attenuators are available in the RF systems of the three S-band TW sec-

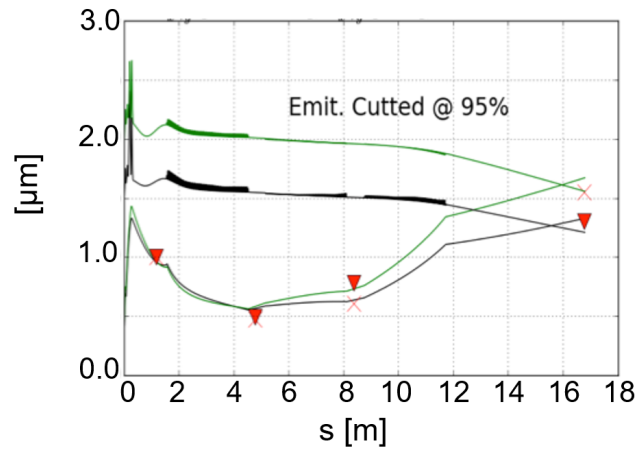


Figure 4.15: Electron beam emittance (upper curves) and envelope evolution (lower curves) from the photo-cathode to the linac exit calculated with the Astra code. The crosses and triangles represent the beam spot measurements taken in this configuration at screen locations along the linac.

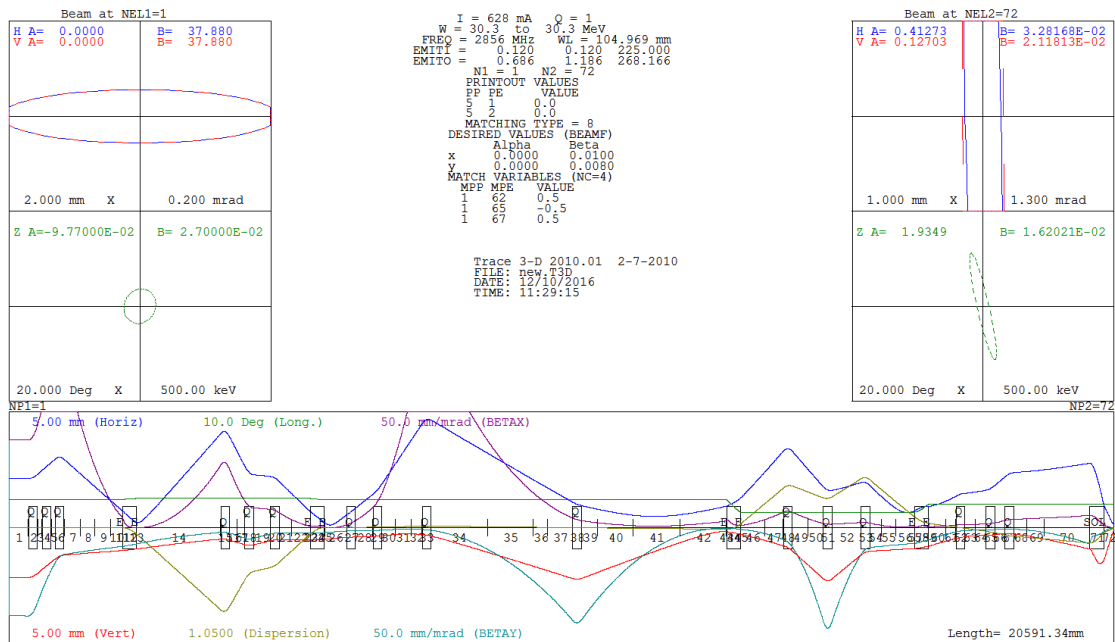


Figure 4.16: Twiss parameters and envelope evolution from the linac exit to the Thomson IP obtained with the TRACE3D code.

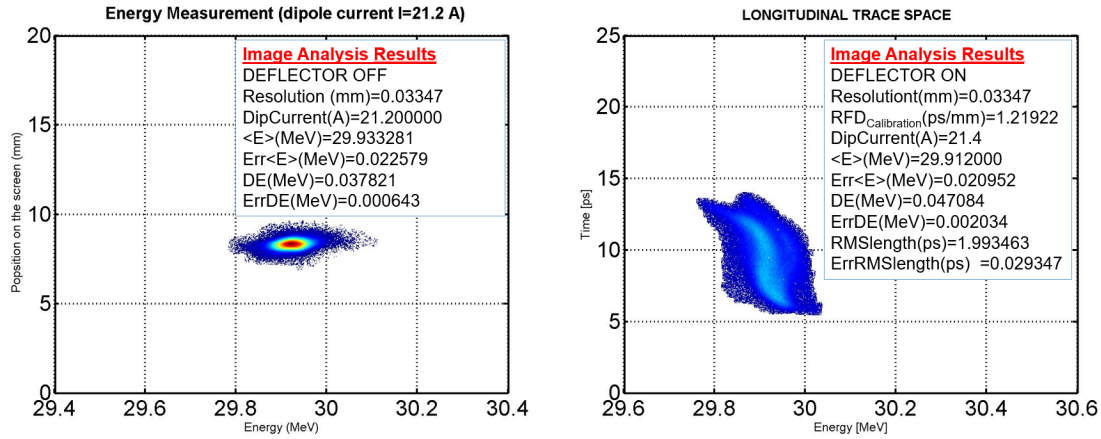


Figure 4.17: Energy measurements obtained by means of the 14 deg dipole (left side plot) and longitudinal phase space measured with the S-band RF deflecting cavity coupled with a 14° by-pass dipole (right side plot).

tions that follow the gun, therefore a hybrid compression-deceleration scheme has been set with the following phases of the accelerating sections: $\Phi S_1 = 32 \text{ deg}$, $\Phi S_2 = -72 \text{ deg}$, $\Phi S_3 = -134 \text{ deg}$ from crest, in order to minimize the effects of the power amplitude jitter from the feeding Klystrons, and obtain a final energy of 30 MeV with an energy jitter less than 0.02 MeV and energy spread $\Delta\gamma/\gamma = 0.1 \%$. The applied acceleration/deceleration scheme worked well enough to produce a low energy spread electron beam at 30 MeV, even though resulting in a strong sensitivity for the electron beam to the machine imperfections/stability. The plots in Figure 4.17 show the energy measurements obtained by means of the 14 deg dipole and longitudinal phase space measured with the S-band RF deflecting cavity coupled with a 14° by-pass dipole; the plots in Figure 4.18 show the measured beam energy and current longitudinal profile related to the longitudinal phase space in Figure 4.17. The emittance evolution measurement is performed with the quadrupole scan technique in each straight section downstream the dipole pairs and result in measured emittance ranging in 2 - 4 mm mrad.

The final focusing is performed in the final straight section using a quadrupole magnet triplet and a solenoid, with a maximum field $B = 1.1 \text{ T}$, close to the IP. At 30 MeV the minimum obtained spot size for the electron beam, captured on the YAG screen located at the IP, was around $\sigma_{rms} \approx 60 - 80 \mu\text{m}$ as reported in Figure 4.19.

In Table 4.2 are presented the beam parameters measured at SPARC.LAB Thomson source for the working point of the second commissioning phase with best performances in terms of X-ray flux.

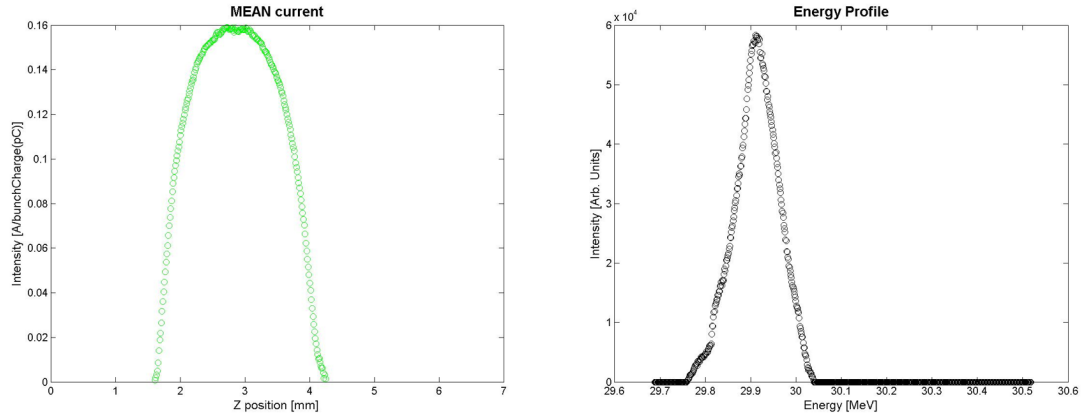


Figure 4.18: Measured beam energy (left side plot) and current longitudinal profile (right side plot) related to the measured longitudinal phase space in Figure 4.17.

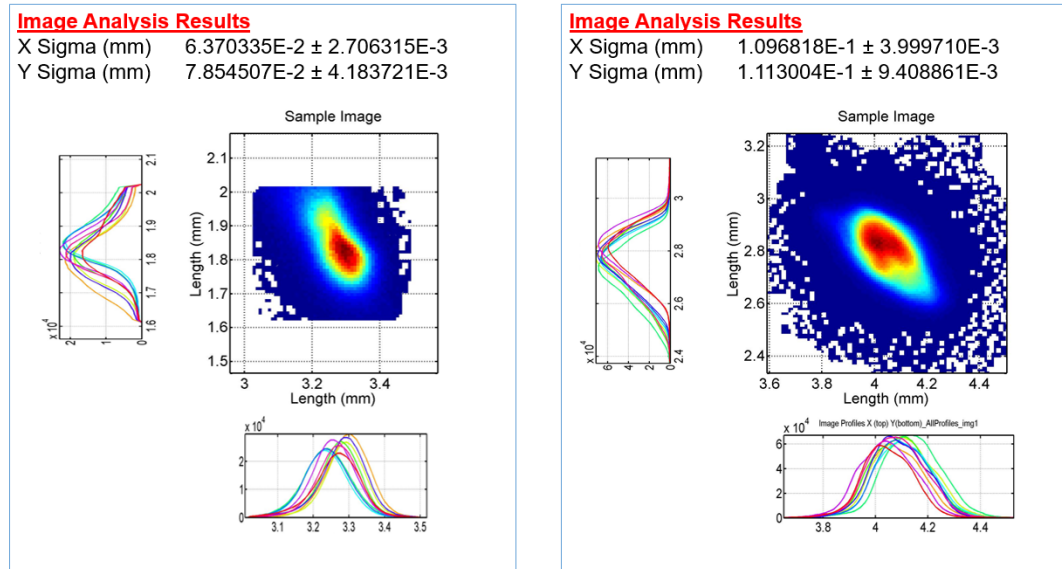


Figure 4.19: Minimum rms spot size captured on the YAG screen located at the IP of 60 - $80 \pm 3 \mu\text{m}$ (left side plot) and enlarged electron beam spot size of $\sigma_{xy} = (110 - 109 \pm 10) \mu\text{m}$ which allowed the best result in terms of source flux (right side plot).

Table 4.3: Beam parameters measured at SPARC_LAB Thomson source for the working point of the second commissioning phase with best performances in terms of X-ray flux.

Electron Beam Parameters @IP		
all values are rms		
Charge	100 - 200 \pm 20	pC
<Energy>	30	MeV
Energy Jitter	0.02	MeV
Energy Spread	0.10	%
Pulse Length	2.2 \pm 0.02	ps
Spot Size	110 \pm 10	μ m
Emittance	1.2 - 2.2 \pm 0.2	mm mrad
FLAME Laser Beam Parameters @IP		
Pulse energy	2	J
Wavelength	800	nm
Pulse Length [r.m.s.]	6	ps
Spot Size w_0	150	μ m
Repetition Rate	10	Hz
X-ray Photon Beam Parameters		
<Energy>	60	keV
Spot Size [r.m.s.]	10	μ m
Bandwidth [r.m.s.]	19	%
Photon Flux	$2 * 10^5$	Photons per pulse in bw

FLAME pulse In this Thomson Source experiment FLAME provided a 2 J laser beam at IP with 6 ps pulse width and $w_0 \simeq 150 \mu\text{m}$, even if a $w_0 \simeq 10 \mu\text{m}$ could be reached. In Table 4.2 are presented the beam parameters measured at SPARC_LAB Thomson source for the working point of the second commissioning phase with best performances in terms of X-ray flux.

X-ray source For the selected WP with 200 pC and 30 MeV electron beam at the Linac exit the measured normalized transverse emittance was $\epsilon_{nt} = 1.2 - 2.2 \pm 0.2$ mm mrad, with an energy spread of 0.1 ± 0.03 %, and a $\sigma_z = 2.2 - 0.2$ ps. The minimum electron beam size reached was $\sigma_r = 60 - 80 \pm 10 \mu\text{m}$. Due to background problems on the X-ray detectors, placed relatively close to the electron beam dumper, we should

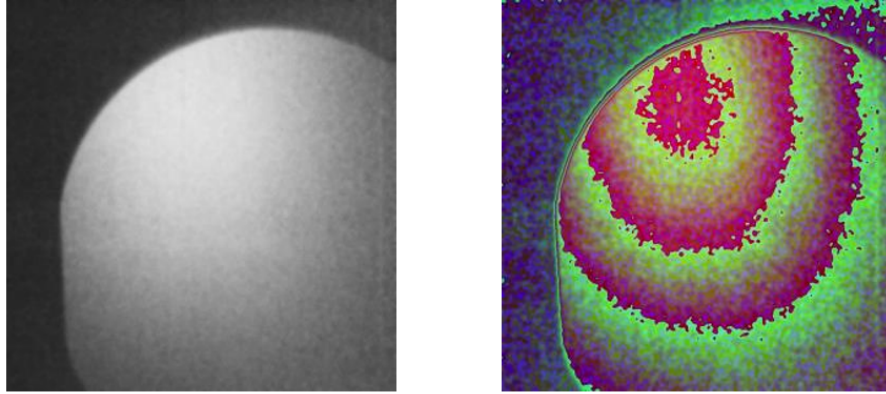


Figure 4.20: Thomson X-radiation image collected with Hamamatsu imager Flat Panel C9728DK-10, located at 300 cm from the IP, with 1 s exposure time and averaged over 100 images

limit the IP electron spot size to $\sigma_t = 110 \pm 10 \mu m$. In fact, due to a residual misalignment of the electron beam with respect to the dumper vacuum pipe (enhanced by the strong focusing field of the solenoid $B = 0.7$ T), the background increased when the beam divergence was higher as a consequence of a stronger focusing at IP. This misalignment was also detected by the image recorded data that are shown Figure 4.20 where the Thomson radiation image is clearly cut by the Perspex CF 40 window profile. To measure the radiation energy two k-edge filters, Nb and Zr, were also used, resulting in a roughly estimated value of 13 keV, confirming the cut of the most energetic part of the produced radiation due to the tilted electron trajectory. In fact, with our commissioning setup the expected number of photons in the 20 % bandwidth is $\approx 1.4 * 10^6$ photons/shot with $U_L = 2$ J, $Q = 200$ pC, $\delta\phi = 0.2$, $h\nu = 1.55$ eV, $\sigma_t = 110 \mu m$ and $w_0 = 150 \mu m$ while our measured photon flux is $N_\gamma = 10^4$ photons/pulse. Another contribution to the reduction of the obtained photon flux can also come from the jitter sensitivity of our 30 MeV working point, deeply off crest in the S-band accelerating sections, as coming out from the simulation results shown in Figure 4.21, where the Thomson radiation spectrum is shown as calculated with CAIN code starting from the measured parameters for the electron and photon beams and its sensitivity to the jitter of electron beam horizontal centroid is shown in terms of photon flux reduction Figure 4.21.

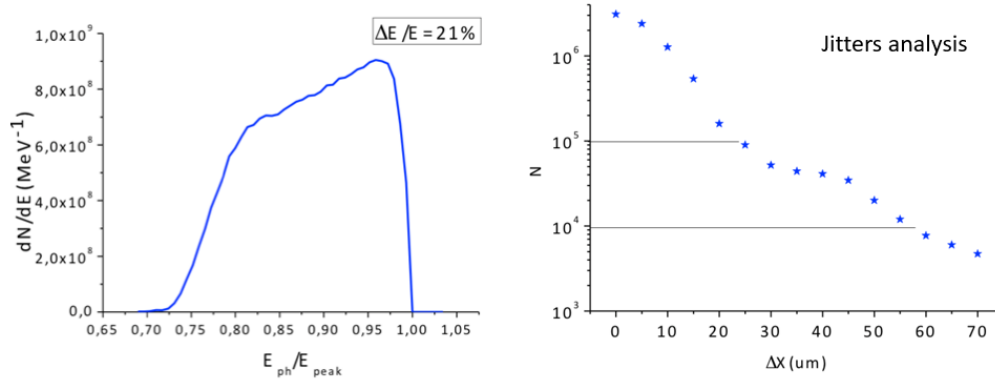


Figure 4.21: Thomson X-radiation spectral distribution calculated from the measured electron and laser beam parameters for this second commissioning shift (left side plot) and the relative photon flux reduction estimation coming from the jitter in the transverse electron beam centroid (right side plot).

4.4 Final Considerations

The commissioning phase of the SPARC_LAB Thomson source took place in the February 2014 and June 2015 dedicated shifts with the aim to provide an electron beam with energies of 30 and 50 MeV. The measured electron beams have resulted to be satisfactory in agreement with the beam dynamics simulation results and in both shifts a photon flux of $\simeq 10^4$ photons/pulse and a BW $\simeq 20\%$ have been measured. Nevertheless there is still room for improvements towards the nominal source performances in terms of flux and bandwidth.

In this commissioning phase an acceleration/deceleration scheme has been adopted to generate electron beam energies lower than 50 MeV trying to rely only on the available hardware, i.e. phase shifters on the S-band cavities that follow the RF gun. This scheme worked well enough, even though resulting in a strong sensitivity for the electron beam to the machine imperfections and stability. In the next future the insertion of RF attenuators in the RF system of the S-band TW sections is foreseen enabling more stable injector working points that minimise the electron beam energy and pointing instabilities that are strictly correlated to the source bandwidth and flux.

Improvements are needed also in the beam procedure alignment whose resolution has been determined by the He-Ne laser properties. The achievable setting precision

of the He-Ne laser and its spot enlargement at the radiation exit window can introduce the final offset of this line of the order of $\pm 4 - 5$ mm respect to the electron beam reference line, and so a superposition of the two beams on the IP screen by means of the steerer magnets can lead to a non zero angle of the electron beam trajectory and a non negligible offset at the entrance of the focusing solenoid, much more severe as long as lower is the electron beam energy. This offset together with the residual misalignments in the electron beam-line, 1 cm shift in one second dogleg quadrupole respect to the nominal lattice model, impeded to provide the required beam spot size of the order of 10 - 20 μm and resulted in a poor overlap conditions between the electron and laser beams.

The optimisation plan foresees a better control of the electron trajectory at the IP to avoid unrecoverable off-axis emission of the Thomson radiation and too high background contribution to the X-ray detectors signal.

The Perspex CF 40 radiation exit window has been replaced with a DN100 one to avoid to cut the radiation exiting the interaction chamber with an offset from the reference line due to the tilted electron beam trajectory. Also the tapered pipe has been replaced with a DN100 straight one to reduce background and allow to squeeze the e-beam down to nominal size.

An interaction setup upgrade is also under study, enabling a non-zero angle collision in order to make it easier the electron and laser pulse trajectory control removing the on axis counter propagation that limits the room availability for both beams diagnostic. It will include the installation of 4-button BPMs downstream the IP and on the dumping pipe to control the electron beam trajectory inside the solenoid and the insertion of referenced pinhole upstream and downstream the IP for FLAME laser beam alignment.

Based on ELI-NP linac sensitivity studies, the introduction of a feedback loop that works towards the source luminosity optimisation, not dependent on the BPM resolutions, could drive to the best collision alignment through a proper setting of the steerer magnets immediately upstream the IP and ensure a stable and reliable routine operation with an electron beam pointing jitter $< 1 \mu m$.

Further in the next future thanks to the FLAME laser system flexibility, non-linear regimes for the Compton scattering could be explored together with new experimental schemes that conjugate the Compton radiation production with the most advanced plasma based acceleration schemes for the electrons.

Conclusions

The guide-lines for the 6D phase space optimisation for high brightness electron beams in RF linacs have been described for advanced and high brilliance Inverse Compton X and γ ray sources. In particular has been shown that the expertise coming from the R&D activity on high brightness linear accelerators, if coupled with high quality high power ps laser system, enables reliable and demanding radiation source that are today in the transition phase towards the era of effective user facilities in X-ray imaging and γ -ray Nuclear Physics and Photonics.

Electron beam dynamics studies have been presented for the ELI-NP GBS linac to provide an electron beam at the interaction point such to optimise the γ -ray source performances. In particular the aspects that are mostly involved in the robustness, operational reliability and active and passive element constraints specifications of such a demanding machine have been investigated and the challenge introduced by the multi-bunch operation has been evaluated including in the analysis the effect of short and long-range wakefield effects. In the next future the study of the wakefields effects on the beam quality will be extended to the beam dynamics in the RF gun and in the two S-band SLAC type TW cavities and transverse long-range wakefields effects will be addressed. Finally machine sensitivity studies will be completed next with other type of deviations as steerer magnets and BPM alignment errors to check the robustness of the machine in the multi-bunch operation.

The beam dynamics simulations in the SPARC.LAB Thomson Source beam-line have been presented together with the strategies adopted in the commissioning phase to optimise the 50 and 30 MeV electron beam at the interaction point in the first and

second experimental campaigns. The commissioning phase of the Thomson source started in 2014 and the two dedicated shifts resulted both in the photon flux of $\simeq 10^4$ photons/pulse with moderate (20%) monochromaticity. Residual misalignments in the electron beamline and a not optimised alignment between the electron beam and the FLAME pulse led to adopt more relaxed parameters for the commissioning phase than the ones required for the generation of X-rays useful for the X-ray imaging of mammographic phantoms with the phase contrast technique. In the next future thanks to the FLAME laser system flexibility non-linear regimes for the Compton scattering could be explored together with new experimental schemes that conjugate the Compton radiation production with the most advanced plasma based acceleration schemes for the electrons.

The practical experience coming from the commissioning of the SPARC_LAB TS beam-line demands the need of high level applications to be used for the machine installation and stabilization (as the beam base alignment procedure or dispersion free steering method) and for the transport of the electron beam at the interaction point through on-line measurements and feedback loops acting on the machine to optimise the final source luminosity. In the meantime the simulations made for the ELI-NP linac are giving hints for improving the Thomson Source performances by indicating a possible upgrade of the electron beam line, as the optimisation plan foreseen for the interaction module, that will include BPM both upstream and downstream the IP and, and for the procedure of the collision alignment to ensure a stable and reliable routine operation with an electron beam pointing jitter $< 1 \mu m$.

It is worth to notice the relevance of the SPARC_LAB Thomson source in terms of energy tunability that, for example, will provide the possibility to explore the ELI-NP Gamma Beam Source low energy range operation. Certainly the opportunity to test the electron beam dynamics together with the electron and radiation diagnostic have played an important role in the understanding of the electron beam dynamics process and is playing an important role also in view of the ELI-NP machine future commissioning in Magurele under the INFN responsibility, to which I will take part.

Transverse Wakefield Effects

The electron beam dynamics in the ELI-NP GBS linac has been illustrated in 3.4 to evaluate the transverse wakefield effects in the single-bunch operation. The aim here is to summarise the analytical formulas of the beam centroid motion as obtained in [77] in case of injection offsets at the linac entrance (Δ_{inj}) or cavity misalignments (Δ_{mis}).

A.1 Effect of Injection Offset

Let us assume that the beam consists of two macro-particles, each of charge $Q/2$ separated by $\Delta z = 2\sigma_z$ as illustrated in Figure A.1. If an injection offset at the linac entrance (Δ_{inj}) occurs the beam undergoes a coherent betatron oscillation; then the equations of motion of the particles become

$$\begin{cases} x_1'' + k_1^2 x_1 = 0 \\ x_2'' + k_2^2 x_2 = \frac{QW_{0\perp}(2\sigma_z)}{2E(s)/e} x_1 \end{cases}$$

where k_i is the betatron wave number for the head and the tail particle respectively (with $k = 1/\beta$), $W_{0\perp}(2\sigma_z)$ is the transverse wakefield at the the distance $\Delta z = 2\sigma_z$ and $E(s)$ the electron beam energy at s . The head particle is not affected by the transverse field, and so it undergoes free betatron oscillations with

$$x_1 = \Delta_{inj} \cos(k_1 s) \tag{A.1}$$

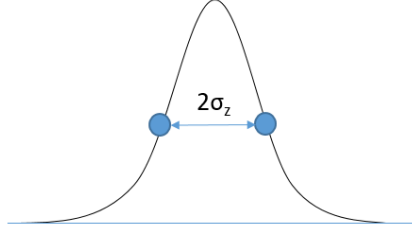


Figure A.1: Two particle model: the beam consists of two macro-particles, each of charge $Q/2$ separated by $\Delta z = 2\sigma_z$.

The tail particle instead is affected by the transverse wakefield excited by the passage of the leading particle. In the hypothesis that $k_1 = k_2$ the equation of motion of the trailing particle is the one of a harmonic oscillator driven on resonance

$$x_2 = x_1 + \frac{QW_{0\perp}(2\sigma_z)}{4kE(s)} \Delta_{inj} s \sin(ks) \quad (\text{A.2})$$

It is worth mentioning that the trajectory difference oscillates with an amplitude increasing with s , therefore high injection offset can lead to transverse instabilities.

The (A.2) does not include the acceleration; this can be introduced by integrating over the cavity length the relative displacement of the tail with respect to the head for a length ds

$$\left| \frac{\Delta x}{x_1} \right| = \frac{QW_{0\perp}(2\sigma_z)}{4E_0} \int_0^s \frac{\beta(s')}{\gamma(s')} ds' \quad (\text{A.3})$$

The (A.3) can be solved numerically or by assuming the specific behaviour of $\beta(s)$ and $\gamma(s)$. For example for $E(s) = E_0 + Gs$ with G a constant accelerating gradient and constant beta function, the (A.3) becomes

$$\left| \frac{\Delta x}{x_1} \right| = \frac{QW_{0\perp}(2\sigma_z)}{4G} \beta \ln\left(\frac{\gamma(s)}{\gamma_0}\right) \quad (\text{A.4})$$

Moreover if β varies as the square root of the energy, as it is in a real accelerator with alternating-gradient focusing (like a FODO lattice), the (A.3) becomes

$$\left| \frac{\Delta x}{x_1} \right| = \frac{QW_{0\perp}(2\sigma_z)}{2G} \beta_{m0} \left(\sqrt{\frac{\gamma_f}{\gamma_0}} - 1 \right) \quad (\text{A.5})$$

A.2 Effect of Cavity Misalignments

Let us assume that the beam consists of two macro-particles, each of charge $Q/2$ separated by $\Delta z = 2\sigma_z$ as illustrated in Figure A.1. If a cavity misalignment (Δ_{mis}) occurs the head of the beam passes undamaged, but the core and the tail of the bunch feel the wakefield excited by the head passage.

The equation of horizontal motion of a particle at time τ that experiences the transverse wakefield force and the external forces of the focusing lattice, taking into account the acceleration, is

$$\frac{1}{\gamma(s)} \frac{d}{ds} \left[\gamma(s) \frac{dx(\tau, s)}{ds} \right] + K(s)x(\tau, s) = \frac{F_{\perp}(\tau, s)}{E(s)} \quad (\text{A.6})$$

where $K(s) = \frac{1}{B\rho} \frac{\partial B_y}{\partial x}$ is the focusing strength.

If Δ_{mis} is the displacement of the structure with respect to the beam centerline and x is the displacement of a particle at the position s , the offset of the particle with respect to the cavity axis is $x - \Delta_{mis}$. Then the total force experienced by the test particle at time τ is

$$F_{\perp}(\tau, s) = e \int_{-\infty}^{\tau} W_{0\perp}(\tau - \tau') \rho(\tau') x(\tau', s) d\tau' = e \int_{-\infty}^{\tau} W_{0\perp}(\tau - \tau') \rho(\tau') [x(\tau', s) - \Delta_{mis}] d\tau' \quad (\text{A.7})$$

where ρ is the bunch charge distribution such that the total charge $Q = \int \rho(\tau) d\tau$.

At every traversal of the structure j , the trailing particle experiences a kick $\Delta x'_j$ due to the wakefield excited by the bunch head as follows

$$\Delta x'_j = - \frac{QW_{0\perp}(2\sigma_z)}{E_j/e} \Delta_{mis_j} L_j \quad (\text{A.8})$$

where $W_{0\perp(2\sigma_z)}$ is the transverse wakefield at the distance $\Delta z = 2\sigma_z$ and E_j is the electron beam energy, L_j and Δ_{mis_j} are the length and the misalignments of the accelerating cavity j .

The beam displacement at s is the sum of the betatron oscillations excited upstream by the transverse kicks

$$x(s) = \sum_j^{s_j < s} R_{12(s_j, s)} \Delta x'_j \quad (\text{A.9})$$

with R_{12} the transport matrix coefficients that transfer the angular kick to the displacement at s

$$R_{12(s_j, s)} = \sqrt{\beta(s)\beta_j} \sin(\Psi(s) - \Psi_j) \times \sqrt{\frac{\gamma_j}{\gamma(s)}} \quad (\text{A.10})$$

where $\beta(s)$ and $\gamma(s)$ are the beta function and the Lorentz factor of the electron beam at s , β_j and γ_j are the beta function and the Lorentz factor of the electron beam at the centre of the structure and $(\Psi(s) - \Psi_j)$ is the phase advance from the centre of the structure j to the position s .

Then For $\Delta_{mis} \neq 0$ the equation of motion of the beam centroid becomes [77]

$$x(s) = -\frac{QW_{0\perp(2\sigma_z)}}{2E_0} \sqrt{\frac{\beta(s)}{\gamma(s)}} \left(\sum_{j=1}^{N_s} \sqrt{\frac{\beta_j}{\gamma_j}} \sin(\Psi(s) - \Psi_j) \right) \Delta_{mis_j} L_j \quad (\text{A.11})$$

Transverse Beam Dynamics in RF Accelerating Structures

The electron beam dynamics in the ELI-NP GBS linac has been illustrated in 3.4 in case of a quasi-constant accelerating field profile in the C-band cavities. The aim here is to provide a model for the particle transverse motion in a real TW cavity induced by RF fields [127, 82, 128], including the fringe field in the input and output RF couplers, in terms of the transport matrix R.

The idea, used in several codes as for example Tstep [50] and Elegant [52], is to combine pure π -mode standing wave, to simulate the couplers, with a travelling wave to simulate the body of the cavity. Coupler regions are simulated based on the Serafini-Rosensweig model described in [82]: the fringe field at beginning is simulated with a half standing wave cell leading the TW cavity; the fringe field at end is simulated with half standing wave cell trailing the TW cavity. The body of the cavity is split in n constant profile TW structures with a $2\pi/3$ field phase advance per cell (with $n = 1, n_{\text{cell}}$ and n_{cell} the total cell number in the structure) to provide a good enough approximation to the design gradient profile.

Let us describe the radial electromagnetic force on an ultra-relativistic paraxial charged particle due to the transverse rf fields in a cylindrically symmetric, spatially periodic, rf cavity. In terms of the longitudinal accelerating field profile E_z it can be written as

$$F_r \cong -\frac{qr}{2} \frac{dE_z}{dz} \quad (\text{B.1})$$

where q is the charge of the particle and the total derivative with respect to z , the

distance along the beam axis that the particle propagates. To maintain the discussion in most general terms let us write the longitudinal field profile in the most general Floquet form [129]

$$E_z = E_0 \text{Re} \left[\sum_{n=-\infty}^{\infty} b_n e^{i(\omega t - k_n z)} \right] \quad (\text{B.2})$$

where E_0 is the average accelerating field experienced by an on-crest particle injected at the phase which gives maximum acceleration, $k_n = (\psi + 2\pi n)$ is the wave-number of the travelling wave associated with the n -th space harmonic considered with respect to the periodicity length d of the structure, and $\psi = l\pi/m$ is the phase advance per cavity cell (l, m being integers, $l \leq m$). Following [82, 128] it is possible to average the periodic force derived from (B.1) and (B.2).

$$\overline{F_r} = \eta(\Delta\phi) \frac{(qE_{acc})^2}{8\gamma E_0} r \quad (\text{B.3})$$

where $\eta(\Delta\phi) = \sum_{n=1}^{\infty} b_n^2 + b_{-n}^2 + 2b_n b_{-n} \cos(2\Delta\phi)$, $\Delta\phi$ is the phase of the particle with respect to the maximum acceleration phase and E_0 the electron rest mass. The function $\eta(\Delta\phi)$ contains the information about the longitudinal field distribution as obtained by electromagnetic design computer codes or from bench measurements. This second-order ponderomotive focusing force can, because of its cylindrical symmetry, be written as a focusing strength parallel to either transverse Cartesian axis

$$K_r = -\frac{\eta(\Delta\phi)}{8\cos^2(\Delta\phi)} \left[\frac{\gamma'}{\gamma} \right] \quad (\text{B.4})$$

where $\gamma' = qE_0 \cos(\Delta\phi)/E_0$ is the gradient in the particle energy averaged over a period of the structure.

The (B.4) has been calculated in [128] for standing and travelling wave structures and, in the specific case the rf wave contains only the fundamental spatial harmonics. For a pure π -mode standing wave the focusing strength in a SW accelerating structure it follows

$$K_r^{SW} = \frac{1}{8} \left[\frac{\gamma'}{\gamma} \right]^2 \quad (\text{B.5})$$

while in a TW accelerating structure the focusing strength disappears completely.

Above these considerations the first order beam transport matrix R has been calculated for a standing wave and a travelling wave section in [127].

The first order beam transport matrix R_{TW} for a travelling wave section include the adiabatic damping and can be written as two matrices, one describing a drift with a modified length L^* and the second one scaling the entry angle with the ratio γ_i/γ_f of the initial to the final energy R^{ad} . The length L refers to the cavity length and $\Delta\gamma$, is the change in energy.

$$R_{TW} = \begin{bmatrix} 1 & L \frac{\gamma_i}{\Delta\gamma} \ln \frac{\gamma_f}{\gamma_i} \\ 0 & \frac{\gamma_i}{\gamma_f} \end{bmatrix}$$

The standing wave cavity accelerates the electron beam under the presence of a radial focusing force, as already mentioned above. The consequence is that the corresponding beam transport matrix $R_{SW}^{K_r}$ is now the matrix of a focusing quadrupole with its strength K_{SW} acting over the length L^* , which has been modified by the adiabatic damping.

$$R_{SW}^{K_r} = \begin{bmatrix} \cos \sqrt{K_r^{SW}} L^* & \frac{1}{\sqrt{K_r^{SW}}} \sin \sqrt{K_r^{SW}} L^* \\ -\frac{\gamma_i}{\gamma_f} \sqrt{K_r^{SW}} \sin \sqrt{K_r^{SW}} L^* & \frac{\gamma_i}{\gamma_f} \cos \sqrt{K_r^{SW}} L^* \end{bmatrix}$$

Now the adiabatic damping is considered by multiplying the $R_{SW}^{K_r}$ matrix with the one scaling the resulting angle with the ratio γ_i/γ_f of the initial to the final energy R^{ad} . The complete traversal of an rf cavity requires that the particle experience a first-order transient force in the fringe field regions at both the entrance and exit of the cavity R_{SW}^{kick} . Ignoring the variation of the both the particle energy and transverse position in the transient region it follows

$$R_{SW}^{kick} = \begin{bmatrix} 1 & 0 \\ \mp \frac{\gamma'}{2\gamma_{i(f)}} & 1 \end{bmatrix}$$

and so the complete matrix becomes

$$R_{SW} = \begin{bmatrix} \cos \sqrt{K_r^{SW}} L^* - \sqrt{2} \sin \sqrt{K_r^{SW}} L^* & \sqrt{8} \frac{\gamma_i}{\gamma_f} \sin \sqrt{K_r^{SW}} L^* \\ -\frac{3\gamma_f'}{\sqrt{8}\gamma_f} \sin \sqrt{K_r^{SW}} L^* & \frac{\gamma_i}{\gamma_f} [\cos \sqrt{K_r^{SW}} L^* + \sqrt{2} \sin \sqrt{K_r^{SW}} L^*] \end{bmatrix}$$

Now it is possible to write the complete transport matrix for the particle transverse motion in a real TW cavity induced by RF fields combining R_{SW} and R_{TW} and so

$$R = R_{SW}^{inj} R_{TW} R_{SW}^{ext} \quad (\text{B.6})$$

with R_{SW}^{inj} and R_{SW}^{ext} the R matrix of respectively the input and output coupler.

Let us now consider a quasi-constant field profile; the body of the cavity can be split in n constant profile TW structures and so the R_{TW} should become the product of the R_{TW}^n (with $n = 1, n_{cell}$ and n_{cell} the total cell number in the structure). The final transport matrix becomes

$$R = R_{SW}^{inj} \left(\prod_{i=1}^{n_{cell}} R_{TW}^i \right) R_{SW}^{ext} \quad (\text{B.7})$$

Bibliography

- [1] A. H. Compton, “A quantum theory of the scattering of x-rays by light elements,” *Phys. Rev.*, vol. 21, pp. 483–502, May 1923. Available online: <http://link.aps.org/doi/10.1103/PhysRev.21.483>
- [2] H. Motz, “Applications of the radiation from fast electron beams,” *Journal of Applied Physics*, vol. 22, no. 5, pp. 527–535, 1951. Available online: <http://scitation.aip.org/content/aip/journal/jap/22/5/10.1063/1.1700002>
- [3] K. Landecker, “Possibility of frequency multiplication and wave amplification by means of some relativistic effects,” *Phys. Rev.*, vol. 86, pp. 852–855, Jun 1952. Available online: <http://link.aps.org/doi/10.1103/PhysRev.86.852>
- [4] R. H. Milburn, “Electron scattering by an intense polarized photon field,” *Phys. Rev. Lett.*, vol. 10, pp. 75–77, Feb 1963. Available online: <http://link.aps.org/doi/10.1103/PhysRevLett.10.75>
- [5] F. Arutyunian *et al.*, “The compton effect on relativistic electrons and the possibility of obtaining high energy beams,” *Physics Letters*, vol. 4, no. 3, pp. 176 – 178, 1963. Available online: <http://www.sciencedirect.com/science/article/pii/0031916363903512>
- [6] W. Herr *et al.*, “Concept of luminosity,” *CAS - CERN Accelerator School: Intermediate Course on Accelerator Physics*, vol. 2, no. 3, pp. 361–378, 2003. Available online: <https://cds.cern.ch/record/941318>

- [7] L. Federici *et al.*, “Backward compton scattering of laser light against high-energy electrons: the ladon photon beam at frascati,” *Il Nuovo Cimento B (1971-1996)*, vol. 59, no. 2, pp. 247–256, 1980. Available online: <http://dx.doi.org/10.1007/BF02721314>
- [8] D. Babusci *et al.*, “Polarized and tagged gamma-ray Ladon beams,” *Riv. Nuovo Cim.*, vol. 19N5, pp. 1–30, 1996.
- [9] J. Bocquet *et al.*, “Graal: a polarized γ -ray beam at esrf,” *Nuclear Physics A*, vol. 622, no. 1, pp. c124 – c129, 1997. Available online: <http://www.sciencedirect.com/science/article/pii/S0375947497003370>
- [10] G. C.M. *et al.*, “Sequential femtosecond x-ray imaging,” *Nature Photonics*.
- [11] T. F. *et al.*, “Few-femtosecond timing at fourth-generation x-ray light sources,” *Nature Photonics*.
- [12] I. V. Pogorelsky *et al.*, “Demonstration of 8×10^{18} photons/second peaked at 1.8 Å in a relativistic thomson scattering experiment,” *Phys. Rev. ST Accel. Beams*, vol. 3, p. 090702, Sep 2000. Available online: <http://link.aps.org/doi/10.1103/PhysRevSTAB.3.090702>
- [13] W. J. Brown *et al.*, “Experimental characterization of an ultrafast thomson scattering x-ray source with three-dimensional time and frequency-domain analysis,” *Phys. Rev. ST Accel. Beams*, vol. 7, p. 060702, Jun 2004. Available online: <http://link.aps.org/doi/10.1103/PhysRevSTAB.7.060702>
- [14] M. Babzien *et al.*, “Observation of the second harmonic in thomson scattering from relativistic electrons,” *Phys. Rev. Lett.*, vol. 96, p. 054802, Feb 2006. Available online: <http://link.aps.org/doi/10.1103/PhysRevLett.96.054802>
- [15] M. Bech *et al.*, “Hard x-ray phase-contrast imaging with the compact light source based on inverse compton x-rays,” *Journal of Synchrotron Radiation*, vol. 16, no. 1, pp. 43–47, Jan 2009. Available online: <https://doi.org/10.1107/S090904950803464X>
- [16] R. Kuroda *et al.*, “Quasi-monochromatic hard x-ray source via laser compton scattering and its application,” *Nuclear Instruments and Methods in Physics Research Section A: Accelerators, Spectrometers, Detectors*

- and Associated Equipment*, vol. 637, no. 1, Supplement, pp. S183 – S186, 2011, the International Workshop on Ultra-short Electron and Photon Beams: Techniques and Applications. Available online: <http://www.sciencedirect.com/science/article/pii/S016890021000793X>
- [17] “Generation of first hard x-ray pulse at tsinghua thomson scattering x-ray source,” *Review of Scientific Instruments*, vol. 84, no. 5, p. 053301, 2013. Available online: <http://aip.scitation.org/doi/abs/10.1063/1.4803671>
- [18] A. Jochmann *et al.*, “Operation of a picosecond narrow-bandwidth laser, Thomson-backscattering x-ray source,” *Nuclear Instruments and Methods in Physics Research Section B: Beam Interactions with Materials and Atoms*, vol. 309, pp. 214 – 217, 2013, the 5th International Conference ‘Channeling 2012’, ‘Charged and Neutral Particles Channeling Phenomena’ September 23-28, 2012, Alghero (Sardinia), Italy. Available online: <http://www.sciencedirect.com/science/article/pii/S0168583X1300298X>
- [19] D. Laundry *et al.*, “Results from the daresbury compton backscattering x-ray source,” *Nuclear Instruments and Methods in Physics Research Section A: Accelerators, Spectrometers, Detectors and Associated Equipment*, vol. 689, pp. 108 – 114, 2012. Available online: <http://www.sciencedirect.com/science/article/pii/S0168900212005542>
- [20] C. Sun *et al.*, “Theoretical and simulation studies of characteristics of a compton light source,” *Phys. Rev. ST Accel. Beams*, vol. 14, p. 044701, Apr 2011. Available online: <http://link.aps.org/doi/10.1103/PhysRevSTAB.14.044701>
- [21] D. J. Gibson *et al.*, “Design and operation of a tunable mev-level compton-scattering-based γ -ray source,” *Phys. Rev. ST Accel. Beams*, vol. 13, p. 070703, Jul 2010. Available online: <http://link.aps.org/doi/10.1103/PhysRevSTAB.13.070703>
- [22] K. Phuoc *et al.*, “All-optical compton gamma-ray source,” *Nature Photonics*.
- [23] V. Petrillo *et al.*, “Ultrahigh brightness electron beams by plasma-based injectors for driving all-optical free-electron lasers,” *Phys. Rev. ST Accel. Beams*, vol. 11, p. 070703, Jul 2008. Available online: <http://link.aps.org/doi/10.1103/PhysRevSTAB.11.070703>

- [24] N. Powers *et al.*, “Quasi-monoenergetic and tunable x-rays from a laser-driven compton light source,” *Nature Photonics*.
- [25] V. Petrillo *et al.*, “Dual color x rays from thomson or compton sources,” *Phys. Rev. ST Accel. Beams*, vol. 17, p. 020706, Feb 2014. Available online: <http://link.aps.org/doi/10.1103/PhysRevSTAB.17.020706>
- [26] A. Debus *et al.*, “Traveling wave thomson scattering and optical undulators for high yield euv and x-ray sources,” *Applied Physics B*, vol. 100, no. 1, pp. 61–76, 2010. Available online: <http://dx.doi.org/10.1007/s00340-010-3990-1>
- [27] A. Jochmann *et al.*, “High resolution energy-angle correlation measurement of hard x rays from laser-thomson backscattering,” *Phys. Rev. Lett.*, vol. 111, p. 114803, Sep 2013. Available online: <http://link.aps.org/doi/10.1103/PhysRevLett.111.114803>
- [28] H. Ikeura-Sekiguchi *et al.*, “In-line phase-contrast imaging of a biological specimen using a compact laser-compton scattering-based x-ray source,” *Applied Physics Letters*, vol. 92, no. 13, p. 131107, 2008. Available online: <http://aip.scitation.org/doi/abs/10.1063/1.2903148>
- [29] M. Babzien *et al.*, “Observation of the second harmonic in thomson scattering from relativistic electrons,” *Phys. Rev. Lett.*, vol. 96, p. 054802, Feb 2006. Available online: <http://link.aps.org/doi/10.1103/PhysRevLett.96.054802>
- [30] Y. Sakai *et al.*, “Observation of redshifting and harmonic radiation in inverse compton scattering,” *Phys. Rev. ST Accel. Beams*, vol. 18, p. 060702, Jun 2015. Available online: <http://link.aps.org/doi/10.1103/PhysRevSTAB.18.060702>
- [31] K. Achterhold *et al.*, “Monochromatic computed tomography with a compact laser-driven x-ray source,” *Scientific Reports*, vol. 3. Available online: <http://dx.doi.org/10.1038/srep01313>
- [32] B. Golosio *et al.*, “Measurement of an inverse compton scattering source local spectrum using k-edge filters,” *Applied Physics Letters*, vol. 100, no. 16, p. 164104, 2012. Available online: <http://aip.scitation.org/doi/abs/10.1063/1.4703932>
- [33] S. Schleede *et al.*, “Emphysema diagnosis using x-ray dark-field imaging at a laser-driven compact synchrotron light source,” *Proceedings of the National*

- Academy of Sciences*, vol. 109, no. 44, pp. 17 880–17 885, 2012. Available online: <http://www.pnas.org/content/109/44/17880.abstract>
- [34] F. Schwab *et al.*, “Comparison of contrast-to-noise ratios of transmission and dark-field signal in grating-based x-ray imaging for healthy murine lung tissue,” *Zeitschrift für Medizinische Physik*, vol. 23, no. 3, pp. 236 – 242, 2013, schwerpunkt: Röntgenbasierte Phasenkontrast Bildgebung. Available online: <http://www.sciencedirect.com/science/article/pii/S0939388912001481>
- [35] “High power laser energy research facility.” Available online: www.hiper-laser.org
- [36] A. Variola *et al.*, “The thomx project status,” in *Proceedings, 5th International Particle Accelerator Conference (IPAC 2014): Dresden, Germany, June 15-20, 2014*, 2014, p. WEPRO052. Available online: <http://jacow.org/IPAC2014/papers/wepro052.pdf>
- [37] R. Ruth, “Testing the compact light source: a miniature synchrotron for the home lab,” *Acta Crystallographica Section A*, vol. 62, no. a1, p. s34, Dec 2006. Available online: <https://doi.org/10.1107/S0108767306099326>
- [38] E. Ettl *et al.*, “The munich compact light source: initial performance measures,” *Journal of Synchrotron Radiation*, vol. 23, no. 5, pp. 1137–1142, Sep 2016. Available online: <https://doi.org/10.1107/S160057751600967X>
- [39] C. Bruni *et al.*, “Thomx - conceptual design report,” Tech. Rep., 2009, a. Variola, A. Loulergue, F. Zomer (eds.). Available online: <http://hal.in2p3.fr/in2p3-00448278>
- [40] B. E. Carlsten, “New photoelectric injector design for the los alamos national laboratory xuv fel accelerator,” *Nucl. Instrum. Meth.*, vol. A285, pp. 313–319, 1989.
- [41] L. Serafini *et al.*, “Envelope analysis of intense relativistic quasilaminar beams in rf photoinjectors: A theory of emittance compensation,” *Phys. Rev.*, vol. E55, pp. 7565–7590, 1997.
- [42] M. Ferrario *et al.*, “Direct measurement of the double emittance minimum in the beam dynamics of the sparcs high-brightness photoinjector,” *Phys.*

- Rev. Lett.*, vol. 99, p. 234801, Dec 2007. Available online: <http://link.aps.org/doi/10.1103/PhysRevLett.99.234801>
- [43] B. Aune *et al.*, “New method for positron production at slac,” *SLAC-PUB-2393*, 1979.
- [44] L. Serafini *et al.*, “Velocity bunching in photo-injectors,” *AIP Conference Proceedings*, vol. 581, no. 1, pp. 87–106, 2001. Available online: <http://scitation.aip.org/content/aip/proceeding/aipcp/10.1063/1.1401564>
- [45] P. Emma, “Accelerator physics challenges of x-ray fel sase sources ,” in *Proc. of the EPAC2002, Paris, France, 2002*.
- [46] L. Serafini *et al.*, “Transverse particle motion in radio-frequency linear accelerators,” *Physical Review E*, vol. 49, no. 2, pp. 1599–1602, 1994. Available online: <http://link.aps.org/doi/10.1103/PhysRevE.49.1599>
- [47] M. Reiser, *Theory and Design of Charged Particle Beams*. Wiley-Interscience Publication, 1994.
- [48] M. Ferrario *et al.*, “Homdyn study for the lcls rf photoinjector,” *Proceedings of the 2nd ICFA Advanced Accelerator Workshop on the Physics of High Brightness Beams*, vol. 004, no. March, pp. 534–563, 2000.
- [49] M. Ferrario *et al.*, “Experimental demonstration of emittance compensation with velocity bunching,” *Phys. Rev. Lett.*, vol. 104, p. 054801, 2010. Available online: <http://link.aps.org/doi/10.1103/PhysRevLett.104.054801>
- [50] L. M. Young, “Tstep ”an electron linac design code”.”
- [51] K. Floetmann, “Astra,” http://desy.de/~mpyflo/Astra_dokumentation, 2011.
- [52] M. Borland, “Elegant: A flexible sdds-compliant code for accelerator simulation,” *Advanced Photon Source LS-287*, 2000.
- [53] K. Crandall *et al.*, *TRACE 3-D Documenation*, third edition ed., L.-U.-. Los Alamos. National Laboratory Reportj, Ed., 1997.
- [54] C. R. C.-. (AP), Ed., *MAD*, 1995.
- [55] J. Billen, *PARMELA*, L.-U.-. Los Alamos. National Laboratory Reportj, Ed., 1996.

- [56] W. Brown *et al.*, “Three-dimensional time and frequency-domain theory of femtosecond x-ray pulse generation through thomson scattering,” *Physical Review Special Topics - Accelerators and Beams*, vol. 7, no. 6, p. 060703, jun 2004. Available online: <http://link.aps.org/doi/10.1103/PhysRevSTAB.7.060703>
- [57] V. Petrillo *et al.*, “Photon flux and spectrum of compton sources,” *Nuclear Instruments and Methods in Physics Research Section A: Accelerators, Spectrometers, Detectors and Associated Equipment*, vol. 693, pp. 109 – 116, 2012. Available online: <http://www.sciencedirect.com/science/article/pii/S0168900212007772>
- [58] L. Serafini *et al.*, “Technical design report: Eurogammas proposal for the eli-np gamma beam system,” *Scientific Editor L. Serafini*, 2014.
- [59] V. Berestetskii *et al.*, *Quantum Electrodynamics*, ser. Course of theoretical physics. Butterworth-Heinemann, 1982. Available online: <https://books.google.it/books?id=URL5NKX8vbAC>
- [60] A. G. Grozin, *Using Reduce in High Energy Physics*. New York, NY, USA: Cambridge University Press, 1997.
- [61] A. G. Grozin, “Complete analysis of polarization effects in e gamma – e gamma with reduce,” in *Joint International Workshop: 8th Workshop in High-energy Physics and Quantum Field Theory and 3rd Workshop on Physics at VLEPP Moscow, Russia, September 15-21, 1993*, 1995, pp. 60–62. Available online: <http://alice.cern.ch/format/showfull?sysnb=2342184>
- [62] C. Sun *et al.*, “Theoretical and simulation studies of characteristics of a compton light source,” *Phys. Rev. ST Accel. Beams*, vol. 14, p. 044701, 2011.
- [63] V. Petrillo *et al.*, “Dual color x rays from thomson or compton sources,” *Physical Review Special Topics - Accelerators and Beams*, vol. 17, no. 2, pp. 1–7, 2014.
- [64] A. Bacci *et al.*, “Electron linac design to drive bright compton back-scattering gamma-ray sources,” *Journal of Applied Physics*, vol. 113, no. 19, 2013. Available online: <http://scitation.aip.org/content/aip/journal/jap/113/19/10.1063/1.4805071>
- [65] C. Vaccarezza *et al.*, “Optimizing rf linacs as drivers for inverse compton sources: the eli-np case,” *Proceedings of LINAC14*, 2014.

- [66] R. Neal *et al.*, “The stanford two-mile accelerator,” *Benjamin, W.A. , Inc. , New York*, 1968.
- [67] D. Alesini *et al.*, “Design and rf test of damped c-band accelerating structures for the eli-np linac,” *Proceedings of IPAC14*, no. c, pp. 40–43.
- [68] D. Alesini *et al.*, “RF deflector design and measurements for the longitudinal and transverse phase space characterization at sparc,” *Nuclear Instruments and Methods in Physics Research Section A: Accelerators, Spectrometers, Detectors and Associated Equipment*, vol. 568, no. 2, pp. 488 – 502, 2006. Available online: <http://www.sciencedirect.com/science/article/pii/S0168900206013040>
- [69] I. Drebot *et al.*, “Expected Gamma Spectra at ELI-NP-GBS,” in *Proc. of International Particle Accelerator Conference (IPAC’16), Busan, Korea, May 8-13, 2016*, ser. International Particle Accelerator Conference, no. 7. Geneva, Switzerland: JACoW, June 2016, paper TUPOW042, pp. 1854–1856, doi:10.18429/JACoW-IPAC2016-TUPOW042. Available online: <http://jacow.org/ipac2016/papers/tupow042.pdf>
- [70] Y. Ding *et al.*, “Measurements and simulations of ultralow emittance and ultrashort electron beams in the linac coherent light source,” *Physical Review Letters*, vol. 102, no. 25, pp. 5–8, 2009.
- [71] C. Ronsivalle *et al.*, “Comparison between sparc e-meter measurements and simulations,” *Proceedings of the IEEE Particle Accelerator Conference*, no. 011935, pp. 986–988, 2007.
- [72] C. Ronsivalle *et al.*, “Simulations of the emittance compensation in photoinjectors and comparison with sparc measurements,” *Proceedings of EPAC 2008*, pp. 21–25, 2008.
- [73] K. Bane, “Short-range wipole wakefields in accelerating structures for nlc,” *SLAC-PUB-9663*, 2003.
- [74] V. Fusco, “Beam dynamics and collective effects in sparc project,” *Ph. D. thesis, University La Sapienza, Rome, Italy*.
- [75] A. Mosnier, “Instabilities in linacs,” *CAS - CERN Accelerator School: 5th Advanced Accelerator Physics Course*, 1994.

- [76] L. Palumbo *et al.*, “Beam dynamics and collective effects in sparac project,” *Proc. of CAS - CERN Accelerator School: 5th Advanced Accelerator Physics Course, Rhodes, Greece, 1994*.
- [77] A. Mosnier, “Instabilities in linacs,” *CAS - CERN Accelerator School: 5th Advanced Accelerator Physics Course, 1994*.
- [78] M. Borland, “Wakefield effects in the advanced photon source linac,” *Proc. PAC 2005, Tennessee, 2005*.
- [79] P. Craievich *et al.*, “Emittance growth due to short-range transverse wakefields in the fermi linac,” *Proceedings of the 27th International Free Electron Laser Conference*.
- [80] A. Giribono *et al.*, “Electron Beam Dynamics Studies for ELI-NP GBS Linac,” in *Proc. of International Particle Accelerator Conference (IPAC'16), Busan, Korea, May 8-13, 2016*, ser. International Particle Accelerator Conference, no. 7. Geneva, Switzerland: JACoW, June 2016, paper TUPOW043, pp. 1857–1860, doi:10.18429/JACoW-IPAC2016-TUPOW043. Available online: <http://jacow.org/ipac2016/papers/tupow043.pdf>
- [81] L. Piersanti *et al.*, “The RF System of the ELI-NP Gamma Beam Source,” in *Proc. of International Particle Accelerator Conference (IPAC'16), Busan, Korea, May 8-13, 2016*, ser. International Particle Accelerator Conference, no. 7. Geneva, Switzerland: JACoW, June 2016, paper MOPMW006, pp. 407–410, doi:10.18429/JACoW-IPAC2016-MOPMW006. Available online: <http://jacow.org/ipac2016/papers/mopmw006.pdf>
- [82] J. Rosenzweig *et al.*, “Transverse particle motion in radio-frequency linear accelerators,” *Phys. Rev. E*, vol. 49, pp. 1599–1602, Feb 1994. Available online: <http://link.aps.org/doi/10.1103/PhysRevE.49.1599>
- [83] A. Giribono *et al.*, “6d phase space electron beam analysis and machine sensitivity studies for eli-np gbs,” *Nucl. Instrum. Meth.*, vol. A829, pp. 274–277, 2016.
- [84] C. Vaccarezza *et al.*, “The sparac_lab thomson source commissioning,” in *Proceedings, 5th International Particle Accelerator Conference (IPAC 2014), Dresden, Germany, June 15-20, 2014*, 2014, p. MOPRO078. Available online: <http://jacow.org/IPAC2014/papers/mopro078.pdf>

- [85] C. Vaccarezza *et al.*, “The sparc_lab thomson source,” *Nuclear Instruments and Methods in Physics Research Section A: Accelerators, Spectrometers, Detectors and Associated Equipment*, vol. 829, no. November, pp. 237 – 242, 2016. Available online: <http://linkinghub.elsevier.com/retrieve/pii/S0168900216001303>
- [86] A. Bacci *et al.*, “Maximizing the brightness of an electron beam by means of a genetic algorithm,” *Nucl. Instrum. Methods Phys. Res. B*, vol. 263, 2007.
- [87] C. Curatolo, “High brilliance photon pulses interacting with relativistic electron and proton beams,” *Ph. D. thesis, University of Milan, Milan, Italy*.
- [88] J. W. Wang, “RF properties structures of periodic for linear accelerating colliders,” *Tech. Rep.*, 1989.
- [89] P. Emma *et al.*, “Linac coherent light source electron beam collimation,” vol. EPAC 06, Edinburgh, Scotland, no. SLAC-PUB-12489, 2006.
- [90] D. H. Dowell *et al.*, “Measurement and analysis of field emission electrons in the LCLS gun,” *Proceedings of the 22nd Particle Accelerator Conference, Albuquerque, New Mexico*, pp. 1299 –1301, 2007.
- [91] D. H. Dowell *et al.*, “Results of the SLAC LCLS gun high-power rf tests,” *Proceedings of PAC07, Albuquerque, New Mexico, USA*, no. TUPMS047, pp. 1296 –1298, 2007.
- [92] A. Bacci, “Private communication: Dark current in the eli-np injector,” 2015.
- [93] M. Ferrario *et al.*, “Sparc_lab present and future,” *Nuclear Instruments and Methods in Physics Research Section B: Beam Interactions with Materials and Atoms*, vol. 309, pp. 183 – 188, 2013. Available online: <http://www.sciencedirect.com/science/article/pii/S0168583X13003844>
- [94] D. Alesini *et al.*, “The c-band accelerating structures for sparc photoinjector energy upgrade,” *Journal of Instrumentation*, vol. 8, no. 05, pp. P05 004–P05 004, 2013. Available online: <http://stacks.iop.org/1748-0221/8/i=05/a=P05004?key=crossref.46e555d219a07dc4eaac1151aebc5cdd>
- [95] F. Le Pimpec *et al.*, “Dark current studies for swissfel,” in *Proceedings, 34th International Free Electron Laser Conference (FEL 2012): Nara, Japan, August*

- 26-31, 2012, 2012. Available online: <http://inspirehep.net/record/1114541/files/arXiv:1205.3098.pdf>
- [96] L. A. Gizzi *et al.*, “An integrated approach to ultraintense laser sciences: The plasmon-x project,” *European Physical Journal: Special Topics*, vol. 175, no. 1, pp. 3–10, 2009.
- [97] D. Alesini *et al.*, “The sparc project: A high-brightness electron beam source at Inf to drive a sase-fel experiment,” *Nuclear Instruments and Methods in Physics Research, Section A: Accelerators, Spectrometers, Detectors and Associated Equipment*, vol. 507, no. 1-2, pp. 345–349, 2003.
- [98] E. Chiadroni *et al.*, “Characterization of the thz radiation source at the frascati linear accelerator,” *Review of Scientific Instruments*, vol. 84, no. 2, 2013.
- [99] M. Ferrario *et al.*, “Homodyn study for the lcls rf photoinjector,” *Proceedings of the 2nd ICFA Advanced Accelerator Workshop on the Physics of High Brightness Beams*, vol. 004, no. March, pp. 534–563, 2000.
- [100] L. Giannessi *et al.*, “Self-amplified spontaneous emission free-electron laser with an energy-chirped electron beam and undulator tapering,” *Phys. Rev. Lett.*, vol. 106, p. 144801, Apr 2011. Available online: <http://link.aps.org/doi/10.1103/PhysRevLett.106.144801>
- [101] L. Giannessi *et al.*, “Self-amplified spontaneous emission for a single pass free-electron laser,” *Physical Review Special Topics - Accelerators and Beams*, vol. 14, no. 6, pp. 1–8, 2011.
- [102] M. Labat *et al.*, “High-gain harmonic-generation free-electron laser seeded by harmonics generated in gas,” *Phys. Rev. Lett.*, vol. 107, p. 224801, Nov 2011. Available online: <http://link.aps.org/doi/10.1103/PhysRevLett.107.224801>
- [103] L. Giannessi *et al.*, “High-order-harmonic generation and superradiance in a seeded free-electron laser,” *Phys. Rev. Lett.*, vol. 108, p. 164801, Apr 2012. Available online: <http://link.aps.org/doi/10.1103/PhysRevLett.108.164801>
- [104] E. Chiadroni *et al.*, “The sparc linear accelerator based terahertz source,” *Applied Physics Letters*, vol. 102, no. 9, p. 094101, 2013. Available online: <http://scitation.aip.org/content/aip/journal/apl/102/9/10.1063/1.4794014>

- [105] E. Chiadroni *et al.*, “The thz radiation source at sparc,” *Journal of Physics: Conference Series*, vol. 357, no. 1, p. 012034, 2012. Available online: <http://stacks.iop.org/1742-6596/357/i=1/a=012034>
- [106] T. Levato *et al.*, “First electrons from the new 220 {TW} frascati laser for acceleration and multidisciplinary experiments (flame) at frascati national laboratories (Inf),” *Nuclear Instruments and Methods in Physics Research Section A: Accelerators, Spectrometers, Detectors and Associated Equipment*, vol. 720, pp. 95 – 99, 2013. Available online: <http://www.sciencedirect.com/science/article/pii/S0168900212015598>
- [107] A. Bacci *et al.*, “Laser induced proton acceleration at the FLAME facility in Frascati: LILIA experiment,” *2nd Workshop - Plasmi, Sorgenti, Biofisica ed Applicazioni*, no. 647554, pp. 136–143, 2012. Available online: <http://siba-ese.unisalento.it/index.php/psba2/article/view/11958/10834>
- [108] P. Oliva *et al.*, “Start-to-end simulation of a thomson source for mammography,” *Nuclear Instruments and Methods in Physics Research Section A: Accelerators, Spectrometers, Detectors and Associated Equipment*, vol. 615, no. 1, pp. 93–99, mar 2010. Available online: <http://linkinghub.elsevier.com/retrieve/pii/S0168900209024012>
- [109] B. Marchetti *et al.*, “Novel schemes for the optimization of the sparc narrow band thz source,” *Review of Scientific Instruments*, vol. 86, no. 7, pp. 0–10, 2015. Available online: <http://dx.doi.org/10.1063/1.4922882>
- [110] D. Alesini *et al.*, “Design, realization and test of c-band accelerating structures for the sparc_lab linac energy upgrade,” *Nuclear Instruments and Methods in Physics Research Section A: Accelerators, Spectrometers, Detectors and Associated Equipment*, vol. 837, pp. 161–170, 2016. Available online: <http://linkinghub.elsevier.com/retrieve/pii/S0168900216309342>
- [111] F. Filippi *et al.*, “Spectroscopic measurements of plasma emission light for plasma-based acceleration experiments,” *Journal of Instrumentation*, vol. 11, no. 09, pp. C09 015–C09 015, 2016. Available online: <http://stacks.iop.org/1748-0221/11/i=09/a=C09015?key=crossref.28ba77e9d3c073fedac4411848c580be>

- [112] F. Filippi *et al.*, “Plasma Density Profile Characterization for Resonant Plasma Wakefield Acceleration Experiment at SPARC_LAB,” in *Proc. of International Particle Accelerator Conference (IPAC’16), Busan, Korea, May 8-13, 2016*, ser. International Particle Accelerator Conference, no. 7. Geneva, Switzerland: JACoW, June 2016, paper WEPMY007, pp. 2554–2556. Available online: <http://jacow.org/ipac2016/papers/wepmy007.pdf>
- [113] J. van Tilborg *et al.*, “Active plasma lensing for relativistic laser-plasma-accelerated electron beams,” *Physical Review Letters*, vol. 115, no. 18, p. 184802, 2015. Available online: <http://link.aps.org/doi/10.1103/PhysRevLett.115.184802>
- [114] M. Ferrario *et al.*, “Laser comb with velocity bunching: Preliminary results at sparc,” *Nuclear Instruments and Methods in Physics Research, Section A: Accelerators, Spectrometers, Detectors and Associated Equipment*, vol. 637, pp. S43–S46, 2011. Available online: <http://dx.doi.org/10.1016/j.nima.2010.02.018>
- [115] A. Petralia *et al.*, “Two-color radiation generated in a seeded free-electron laser with two electron beams,” *Physical review letters*, vol. 115, no. 1, p. 014801, 2015.
- [116] A. Mostacci *et al.*, “Operational experience on the generation and control of high brightness electron bunch trains at sparc-lab,” vol. 9512, p. 95121Q, 2015. Available online: <http://proceedings.spiedigitallibrary.org/proceeding.aspx?doi=10.1117/12.2182566>
- [117] V. Petrillo *et al.*, “Observation of time-domain modulation of free-electron-laser pulses by multi-peaked electron-energy spectrum,” *Phys. Rev. Lett.*, vol. 111, p. 114802, Sep 2013. Available online: <http://link.aps.org/doi/10.1103/PhysRevLett.111.114802>
- [118] F. Giorgianni *et al.*, “Strong nonlinear terahertz response induced by dirac surface states in Bi_2Se_3 topological insulator,” *Nature Communications*, vol. 7, p. 11421, 2016. Available online: <http://www.nature.com/doi/10.1038/ncomms11421>
- [119] F. Giorgianni *et al.*, “Tailoring of highly intense thz radiation through high brightness electron beams longitudinal manipulation,” *Applied Sciences*, vol. 6, no. 2, p. 56, 2016. Available online: <http://www.mdpi.com/2076-3417/6/2/56>

- [120] R. Pompili *et al.*, “Beam manipulation with velocity bunching for pwfa applications,” *Nuclear Instruments and Methods in Physics Research Section A: Accelerators, Spectrometers, Detectors and Associated Equipment*, 2016.
- [121] R. Pompili *et al.*, “Femtosecond timing-jitter between photo-cathode laser and ultra-short electron bunches by means of hybrid compression,” *New Journal of Physics*, vol. 18, no. 8, 2016.
- [122] A. Giribono, “X-ray generation at sparc lab thomson backscattering source,” *Il Nuovo Cimento*, vol. 38 C, no. 83, pp. 1–7, 2015.
- [123] A. W. Chao *et al.*, *Handbook of Accelerator Physics and Engineering*. Singapore: World Scientific, 1999. Available online: <https://cds.cern.ch/record/384825>
- [124] R. Pompili *et al.*, “First single-shot and non-intercepting longitudinal bunch diagnostics for comb-like beam by means of electro-optic sampling,” *Nuclear Instruments and Methods in Physics Research Section A: Accelerators, Spectrometers, Detectors and Associated Equipment*, vol. 740, pp. 216–221, 2014.
- [125] B. Golosio *et al.*, “Measurement of an inverse compton scattering source local spectrum using k-edge filters,” *Applied Physics Letters*, vol. 100, no. 16, 2012. Available online: <http://scitation.aip.org/content/aip/journal/apl/100/16/10.1063/1.4703932>
- [126] P. Cardarelli *et al.*, “Energy distribution measurement of narrow-band ultrashort x-ray beams via k-edge filters subtraction,” *Journal of Applied Physics*, vol. 112, no. 7, 2012. Available online: <http://scitation.aip.org/content/aip/journal/jap/112/7/10.1063/1.4757027>
- [127] D. A. Edwards, “Tesla test facility linac: Design report. version 1.0,march 1, 1995,” 1995.
- [128] S. C. Hartman *et al.*, “Ponderomotive focusing in axisymmetric rf linacs,” *Phys. Rev. E*, vol. 47, pp. 2031–2037, Mar 1993. Available online: <http://link.aps.org/doi/10.1103/PhysRevE.47.2031>
- [129] R. Helm *et al.*, *Linear Accelerators. Edited by Pierre M. Lapostolle (And) Albert L. Septier, P. Lapostolle et al., Eds.*

List of Figures

1.1	List of the existing and planned Compact compton sources updated at 2010 [39].	4
1.2	Emittance double minimum behavior, envelope evolution and emittance behaviour when accelerating structures are properly matched [48].	9
2.1	Geometry of Compton scattering of an electron and a photon in a laboratory frame coordinate system (x_e, y_e, z_e)	14
2.2	Energy distribution - 3-dimensional on the left side plot and 2-dimensional on a screen perpendicular to the electron propagation axis on the right side plot - of the emitted photon at $L = 50$ m downstream the interaction point; the photon is emitted in the head-on collision of a 740 MeV electron, the highest ELI-NP GBS source energy working point, and a 515 nm wavelength photon. The scattered photon energy E_p only depends on the scattering angle θ_f , i.e the energy decreases in circles around z being it independent of the azimuth angle Φ_f	15
2.3	Photon energy as function of the scattering angle θ_f result of the scattering of an electron and a 515 nm wavelength photon. The (2.6) is plotted in the Thomson approximation for several electron energies, each corresponding to the ELI-NP GBS source energy working point; the emitted photon energy depends on the electron energy (γ_i) and, since it decreases as $\gamma_i^2 \theta_f^2$, the photon energy distribution narrows at higher electron energies.	17

2.4	Geometry of Compton scattering of an electron beam and a photon beam in the laboratory frame coordinate system (x, y, z)	18
3.1	ELI-NP Gamma Beam System (GBS) layout: a SPARC-like S-band high brightness injector [49] followed by two C-band RF linacs (low and high energy) that trough the relative transfer lines provide the electron beam to the Low and High Energy Interaction Points (LE IP and HE IP) respectively [58].	27
3.2	Behaviour of the source energy E_{ICS} and of the Compton recoil Δ as function of the electron beam energy E_{e^-} . The electron beam energy is established to range between 75 - 740 MeV	28
3.3	Behaviour of the energy spread dilution due to RF curvature degradation effects as function of the bunch length and of the accelerating frequency in the on crest operation and full relativistic conditions. At ELI-NP GBS the choice has been to inject a $\sigma_z \leq 280\mu m$ in the C-band linac to avoid $\Delta\gamma/\gamma > 0.1\%$. This is obtained by means of the adopted velocity bunching scheme, resulting in a gentle longitudinal compression factor < 3 at the photo injector exit, as routinely and successfully applied at SPARC.LAB.	31
3.4	ELI-NP Gamma Beam System (GBS) layout: a SPARC-like S-band high brightness injector [49] followed by two C-band RF linacs (low and high energy) that trough the relative transfer lines provide the electron beam to the Low and High Energy Interaction Points (LE IP and HE IP) respectively [58].	32
3.5	The whole system have been already mounted and aligned at INFN-LNF laboratories and is hosted on three independent modules: the RF gun and the gun solenoid are on the first module (M1), while the S-band structures on the following ones (M2 and M3).	33
3.6	The RF gun region is composed of a 1.6 cell S-band RF gun, operating at 2.856 GHz, equipped with a copper photo cathode and an emittance compensation solenoid.	33
3.7	The C-band accelerating structures are 1.8 m long and consist of 102 cells with a $2\pi/3$ phase advance per cell. The cavities will be hosted at INFN-LNF laboratories until the commissioning phase; here the vacuum tests for some of them have already started.	34

3.8	Charge distribution at cathode surface produced by the photo-cathode laser pulse as obtained with 2D Tstep simulations.	38
3.9	Longitudinal and transverse phase spaces at the injector exit and evolution of transverse normalised emittance (ϵ red line), spot size (σ_r blue line) and longitudinal bunch length (σ_z green line) from the cathode to the injector exit for a 250 pC electron beam with final energy of 70.5 MeV as obtained with the Tstep code.	39
3.10	Longitudinal and transverse phase spaces at the injector exit and evolution of transverse normalised emittance (ϵ red line), spot size (σ_r blue line) and longitudinal bunch length (σ_z green line) from the cathode to the injector exit for a 250 pC electron beam with final energy of 80.5 MeV as obtained with the Tstep code.	39
3.11	Longitudinal and transverse phase spaces at the injector exit and evolution of transverse normalised emittance (ϵ red line), spot size (σ_r blue line) and longitudinal bunch length (σ_z green line) from the cathode to the injector exit for a 250 pC electron beam with final energy of 90.5 MeV as obtained with the Tstep code.	40
3.12	Right: Pill box cavity model considered for the wake fields calculations. Left: Longitudinal and transverse short-range wake function curves integrated over one cell for the C-band accelerating structure.	41
3.13	6D phase space at LE-IP for the 75 MeV electron beam as obtained by Elegant simulations.	43
3.14	6D phase space at LE-IP for the 234 MeV electron beam as obtained by Elegant simulations.	44
3.15	6D phase space at LE-IP for the 312 MeV electron beam as obtained by Elegant simulations.	44
3.16	6D phase space at HE-IP for the 530 MeV electron beam as obtained by Elegant simulations.	45
3.17	6D phase space at HE-IP exit the 740 MeV electron beam as obtained by Elegant simulations.	45
3.18	Beam energy profile at the C-band linac injection (blue curve) and at LE-IP as obtained by including (red curve) and not including (green curve) the longitudinal wakefields: the beam loses $\sim 0.2\%$ of its energy due to the longitudinal wakefields.	46

3.19	Evolution of the electron beam horizontal distribution along the C-band linac in ideal conditions (left) and in case of $\Delta_{inj} = 500 \mu m$ (centre) or $\Delta_{mis} = 500 \mu m$ (right).	47
3.20	Behaviour of the simulated horizontal centroid (blue markers) - $\langle x \rangle$ - and normalised emittance (red markers) - ϵ_x - as function of Δ_{inj} (left) and Δ_{mis} (right) with (diamonds) and without trajectory correction (rounds) . The behaviour of $\langle x \rangle$ (blue rounded markers) as function of Δ_{inj} (left) and Δ_{mis} (right), confirms the expected linear dependence on Δ_i (blue dashed lines) analytically calculated as described in [75, Ch. 2] (with $i=[inj,mis]$).	47
3.21	Left: Wake potential inside a C-band cavity observed at different istances t_n corresponding to the n^{th} bunch arrive ($n=0,1, \dots, 20$). Right: Total longitudinal wake potential in full beam loading condition, i.e. in the steady state.	50
3.22	Left: Cumulative energy deviation in the multi-bunch operation from the first to the last bunch due to longitudinal long-range wake fields. Right: Relative energy spread in the multi-bunch operation from the first to the last bunch due to longitudinal long-range wake fields.	50
3.23	Left: accelerating field as obtained by simulations and reported in [67]. Right: Accelerating filed as obtained by Elegant simulations (right): the cavity, 1.8 m long and with $2\pi/3$ field phase advance per cell, has been split in n constant profile TW structures (with $n = 1, 3, 6, 17$) to provide a good enough approximation to the design field profile (red dashed line).	52
3.24	Twiss parameters along the linac for the 234 MeV electron beam at LE-IP in case of constant gradient (lines) and quasi constant gradient (dashed lines) C-band accelerating structures.	53
3.25	Energy spread and focal spot size occurrence over 100 machine runs at LE IP in case of errors in the low energy beamline.	56
3.26	Steerer strength needed to centre the electron beam on the BPMs (right) and resulting trajectory errors at LE-IP (left): BPM resolution defines the mean value of trajectory errors $\langle c \rangle$, while steerer strength jitters introduce a standard deviation from the mean value of $\approx \pm 1 \mu m$.	57
3.27	Energy spread occurrence over 350 machine runs in case of errors in the electron beamline.	59
3.28	Focal spot size occurrence over 350 machine runs in case of errors in the electron beamline.	59

<i>List of Figures</i>	125
3.29 Normalised emittance occurrence over 350 machine runs in case of errors in the electron beamline.	60
3.30 6D phase space at injector exit for the dark current as obtained by Astra simulations.	63
3.31 Dark current evolution through the C-band low energy linac matched for the working points illustrated in Table 3.2 as obtained by Elegant simulations. . .	63
3.32 Dark current evolution through the C-band high energy linac matched for the working points illustrated in Table 3.2 as obtained by Elegant simulations.	64
3.33 Dark current Transverse and longitudinal phase space at LE IP as obtained by Elegant simulations. Wakefield and CSR effects are switched-off and the machine model is set up with the design optics for tracking the nominal 250 pC electron beam with a final energy of 234 MeV at the LE-IP.	65
3.34 Dark current Transverse and longitudinal phase space at HE IP as obtained by Elegant simulations. Wakefield and CSR effects are switched-off and the machine model is set up with the design optics for tracking the nominal 250 pC electron beam with a final energy of 530 MeV at the HE-IP.	65
4.1 SPARC_LAB layout: the RF gun (1) is followed by an hybrid linac consisting of two S-band and a C-band TW structures (2), a THz source station and a vacuum chamber devoted to plasma-based experiments (3); the downstream 14 degree dipole (4) delivers the electron beam towards four beam lines devoted to FEL physics (5) both in SASE and with seed-laser (10), beam diagnostics (6), and Thomson back-scattering (8) and plasma acceleration external injection (7) experiments using the FLAME laser pulse (11). .	71
4.2 Thomson Source schematic layout: FLAME laser pulse, passing through a 20 meter long optical beam line in vacuum, collides at the Thomson Interaction Point (IP) with the electron beam coming from the SPARC_LAB high brightness photo injector.	74
4.3 Double dogleg R56 tunability and relative horizontal dispersion plot as obtained by simulation studies. The R_{56} parameter of the dogleg, that represents the correlation between the z and the $\Delta E_e/E_{e0}$, can be set in the range of ± 50 mm.	76

- 4.4 Output signal of this device in the final beamline configuration: the coloured lines in the two graphs represent the losses captured by a series of optical fibers along the line; the peak values correspond to the end of the line (the signal is reflected being the optical fiber non-adapted at the end). In this case the transport current has been optimised and any losses are present in the line up to the IP. 77
- 4.5 3D CAD drawing of the Thomson Interaction vacuum chamber setup on the left. Lateral view of the implemented interaction chamber and parabolic mirror vacuum chamber on the right. 79
- 4.6 Measured beam spot at the focus (TS IP) without (left side plot) and with the phase-front correction (right side plot): the beam is quite oval in the case of no phase front correction and becomes nearly round when the best phase front is applied. Moreover, it is perceptible that the use of the adaptive optics is crucial also for the energy contained in the central spot (considering the $1/e^2$ diameter): indeed after the phase front correction the percentage of the total energy of the laser pulse in the central spot increases from 25 % up to 60 % 80
- 4.7 signals induced by electron and photon pulses in pick-ups placed close to the IP. Taking into account the time-of-flight from pick-up to IP, this measurement allows a coarse temporal pre-alignment of the beams, while a fine temporal superposition can be found experimentally by maximizing the flux of the Thomson radiation. 81
- 4.8 Electron beam imaging at the IP captured without (left side plot) and with the camera that provides the on-line setting of the zoom and focus. The camera is mounted on a remote controlled movement allowing to select the zone of the screen occupied by the beam and to change the resolution from ~ 30 to $10 \mu\text{m}/\text{pixel}$ or less, required to detect a beam spot size of the order of $10 \mu\text{m}$ and to provide the needed alignment accuracy. 82
- 4.9 Electron beam emittance (blue curves) and envelope evolution (black curves) from the photo-cathode to the linac exit calculated with the Astra code. The crosses and triangles represent the beam spot measurements taken in this configuration at screen locations along the linac. 84
- 4.10 Twiss parameters and envelope evolution from the linac exit to the Thomson IP obtained with the TRACE3D code. 85

4.11	Energy measurements obtained by means of the 14 <i>deg</i> dipole (left side plot) and longitudinal phase space measured with the S-band RF deflecting cavity coupled with a 14° by-pass dipole (right side plot).	86
4.12	Measured beam energy (left side plot) and current longitudinal profile (right side plot) related to the measured longitudinal phase space in Figure 4.11.	86
4.13	Minimum rms spot size captured on the YAG screen located at the IP of $90 \pm 3 \mu m$ (left side plot) and enlarged electron beam spot size of $\sigma_{xy} = (240 - 160 \pm 10) \mu m$ which allowed the best result in terms of source flux (right side plot).	87
4.14	Thomson x-rays signal in red, in black the electron background signal (without FLAME laser), integrated over 120 s (1200 pulses) on the left. Spectral density S (MeV^{-1}) versus photon energy on the right.	89
4.15	Electron beam emittance (upper curves) and envelope evolution (lower curves) from the photo-cathode to the linac exit calculated with the Astra code. The crosses and triangles represent the beam spot measurements taken in this configuration at screen locations along the linac.	90
4.16	Twiss parameters and envelope evolution from the linac exit to the Thomson IP obtained with the TRACE3D code.	90
4.17	Energy measurements obtained by means of the 14 <i>deg</i> dipole (left side plot) and longitudinal phase space measured with the S-band RF deflecting cavity coupled with a 14° by-pass dipole (right side plot).	91
4.18	Measured beam energy (left side plot) and current longitudinal profile (right side plot) related to the measured longitudinal phase space in Figure 4.17.	92
4.19	Minimum rms spot size captured on the YAG screen located at the IP of $60 - 80 \pm 3 \mu m$ (left side plot) and enlarged electron beam spot size of $\sigma_{xy} = (110 - 109 \pm 10) \mu m$ which allowed the best result in terms of source flux (right side plot).	92
4.20	Thomson X-radiation image collected with Hamamatsu imager Flat Panel C9728DK-10, located at 300 cm from the IP, with 1 s exposure time and averaged over 100 images	94
4.21	Thomson X-radiation spectral distribution calculated from the measured electron and laser beam parameters for this second commissioning shift (left side plot) and the relative photon flux reduction estimation coming from the jitter in the transverse electron beam centroid (right side plot).	95

- A.1 Two particle model: the beam consists of two macro-particles, each of charge $Q/2$ separated by $\Delta z = 2\sigma_z$ 100

List of Tables

3.1	Summary of ELI-NP GBS Specifications	26
3.2	Simulated parameters of the 250 pC electron beam at IPs as result from beam dynamics studies devoted to optimise the γ -ray source.	37
3.3	Simulated parameters of the 250 pC electron beam at photo-injector exit as result from beam dynamics studies devoted to optimise the γ -ray source. . .	38
3.4	Simulated parameters for the 234 MeV electron beam at LE-IP in case of constant gradient and quasi-constant gradient TW accelerating cavities. . .	54
3.5	Maximum error values for power supplies, magnetic elements and beam position monitors resolution.	55
3.6	Simulated parameters for the 234 MeV electron beam at LE-IP in case of any errors and in case of 70 μm misalignments and jitters on the machine as described in Table 3.5.	60
3.7	Simulated parameters for the 530 MeV electron beam at HE-IP in case of any errors and in case of 70 μm misalignments and jitters on the machine as described in Table 3.5.	60
4.1	SPARC_LAB Thomson source design parameters.	72
4.2	Beam parameters measured at SPARC_LAB Thomson source for the working point of the first commissioning phase with best performances in terms of X-ray flux.	88

4.3	Beam parameters measured at SPARC_LAB Thomson source for the working point of the second commissioning phase with best performances in terms of X-ray flux.	93
-----	---	----



Ringraziamenti

Vorrei ringraziare in primo luogo i controrelatori di questo manoscritto per averlo letto accuratamente e per aver fornito spunti di riflessione e approfondimento, il Prof. Hugues Monard (THOMX) e la Prof. Vittoria Petrillo (INFN-Milano).

Desidero poi ringraziare il Prof. Luigi Palumbo per avermi indicato la strada e per avermi seguito in questo percorso e tutto il gruppo di ricerca del dipartimento SBAI che mi ha dato l'opportunità di rapportarmi sempre con realtà di alto spessore scientifico-tecnologico. In particolare ringrazio il Prof. Andrea Mostacci, il Prof. Mauro Migliorati, la Dott.ssa Livia Lancia e il Dott. Luca Ficcadenti.

Ringrazio il direttore della Divisione Acceleratori Andrea Ghigo che per primo mi ha introdotto al mondo dei Laboratori di Fisica Nucleare di Frascati dove ho svolto la mia attività di ricerca durante il dottorato.

In particolare un grazie va al direttore di SPARC_LAB Massimo Ferrario per avermi accolto in questo gruppo di ricerca. Qui ho trovato persone altamente competenti che con la loro personalità mi hanno fornito uno spaccato vero della vita da ricercatore: David Alesini, Maria Pia Anania, Marco Bellaveglia, Angelo Biagioni, Fabrizio Bisesto, Michele Castellano, Enrica Chiadroni, Alessandro Cianchi, Michele Croia, Nico Di Giovenale, Giampiero Di Pirro, Massimo Ferrario, Alberto Marocchino, Riccardo Pompili, Stefano Romeo, Jessica Scifo, Vladimir Shpakov, Bruno Spataro, Cristina Vaccarezza e Fabio Villa. Farò tesoro di tutti i loro consigli. Ringrazio in particolare Nico, Mariapia e Cristina per aver passato notti intere con me in sala controllo nell'intento di produrre i primi raggi X della sorgente di radiazione SPARC_LAB Thomson Source. Desidero ringraziare Alessandro Variola e tutto il gruppo di ricerca di ELI-NP con il

quale ho lavorato in questi anni. Ringrazio il gruppo della sezione di Milano dell'INFN per le riunioni tanto interessanti quanto fruttose: Luca Serafini, Vittoria Petrillo, Alberto Bacci, Camilla Curatolo e Illya Drebot.

Fra tutti un ringraziamento particolare va a Cristina per i suoi innumerevoli insegnamenti: con pazienza, professionalità e competenza non ti sei mai dispensata dall'ascoltarmi e consigliarmi, GRAZIE! Senza i tuoi insegnamenti questa tesi non sarebbe stata tanto ricca di contenuti; per aver dedicato tempo alla correzione di questo ed altri documenti e per essere stata per me in questi anni mentore ed amica preziosa.

Desidero ringraziare le amiche e colleghe Jessica e Maria Pia per avermi supportato e ascoltato nei momenti di difficoltà e per le stimolanti discussioni in materia scientifica. Infine ringrazio la *Stanza 11* dove ogni giorno è d'obbligo un sorriso: Mario, Angelo e Francesco.

Ringrazio Francesco, Fabio, Massi, Martina e Stefano, che sono stati in questi tre anni di dottorato i miei compagni di avventura e con i quali ho condiviso ansia e gioia allo stesso tempo, oltre che scuole e conferenze dalla Corea fino in Brasile, con un pass through obbligato per l'Isola d'Elba.

Ringrazio i miei genitori e mio fratello per aver creduto in me ed essermi stati vicini sempre: senza il loro appoggio non avrei mai avuto la possibilità di intraprendere questo lungo viaggio iniziato ormai 10 anni fa. Desidero inoltre ringraziare zia Roberta che ho scelto come esempio da seguire sin da piccola per la sua tenacia e la sua inimitabile dolcezza. Ringrazio i miei nonni che mi hanno insegnato ad amare i miei cari e il mio lavoro. Per avermi fatto capire che nella vita quello che conta è fare tutto con passione.

Ringrazio Francesco per avermi sostenuto sempre e incondizionatamente, per avermi spronata a dare sempre il meglio di me. Dal primo istante in cui ci siamo conosciuti ho capito che il nostro sarebbe diventato un legame molto speciale. Lo ringrazio per il suo affetto.

Non potrei assolutamente dimenticare le amiche di sempre Antonietta, Martina e Stefania. Le ringrazio per l'amicizia e l'affetto dimostratomi in questi anni, siamo cresciute e con noi il legame che ci unisce.

Ringrazio tutti coloro che mi hanno incrociato il mio cammino e che mi hanno incoraggiato in questi anni. Ognuno a modo proprio.